Intermediate Filaments Associate with Aggresome-like Structures in Proteostressed *C. elegans* Neurons and Influence the Rate of Large Vesicle Extrusions as Exophers

Authors/affiliations: Meghan Lee Arnold[1], Jason Cooper[1], Rebecca Androwski,[1] Sohil Ardeshna[1], Ilija Melentijevic,[1] Joelle Smart,[1] Ryan J. Guasp[1], Ken C.Q. Nguyen[2], Ge Bai[1], David H. Hall[2], Barth D. Grant[1], Monica Driscoll[1]

[1]Department of Molecular Biology and Biochemistry
Rutgers University, Piscataway, NJ USA, 08855

[2]Department of Neuroscience
Albert Einstein College of Medicine, Rose F. Kennedy Center, Bronx, New York 10461

Corresponding Authors: Monica Driscoll and Barth D. Grant

Email Address: driscoll@biology.rutgers.edu and grant@dls.rutgers.edu
Tel: (848-445-7182) (848-445-7339)

Abstract

In human neurodegenerative diseases, toxic protein aggregates can spread between neurons to promote pathology. In the transparent animal model *C. elegans*, stressed neurons can concentrate fluorescently tagged protein aggregates and organelles and extrude them in large membrane-bound vesicles called exophers, which enter neighboring cells. *C. elegans* exophergenesis may occur by mechanisms analogous to those that enable aggregate spreading in the human brain in neurodegenerative disease. Here we report on aggresome-like biology in stressed *C. elegans* neurons that influences exophergenesis. We show that *C. elegans* intermediate filament proteins IFD-1 and IFD-2 can assemble into juxtanuclear structures with molecular and cellular characteristics similar to mammalian aggresomes and document that these intermediate filaments are required cell autonomously for efficient exopher production. IFD-concentrating structures expand with age or neuronal stress level, can associate with neurotoxic polyglutamine expansion protein HttQ74, and depend upon orthologs of mammalian adapter proteins, dynein motors, and microtubule integrity for aggregate collection into juxtanuclear compartments. IFD homolog human neurofilament light chain hNFL can partially substitute for *C. elegans* IFD-2 proteins in promoting exopher production, indicating conservation of the capacity of intermediate filaments to influence large neuronal extrusions. In sum, we identify an unexpected requirement for specific intermediate filaments (counterparts of human biomarkers of neuronal injury and disease, and major components of Parkinson's disease Lewy bodies) in large vesicle extrusion from stressed neurons.

Introduction

Cellular accumulation of misfolded protein aggregates is a hallmark feature of aging and neurodegeneration that can cause functional decline [1]. Aggregates can be transferred from diseased neurons to nearby cells, via an extracellular spreading process that promotes pathological degeneration [2]. Given that both aggregate accumulation and spreading are prominent features in human neurodegenerative disease pathology, a major goal in neurobiology is to understand the intrinsic and extrinsic mechanisms by which cells manage aggregate toxicity.

Well studied cellular mechanisms that mitigate the deleterious effects of aggregates include internal aggregate collection/concentration (aggresome formation), and degradation via the ubiquitin-proteasome system or the autophagy-lysosome pathway [3]. We discovered another mechanism of neurotoxic aggregate management that relies on extrinsic degradation—*C. elegans* adult neurons can selectively eject material in large (~3.8mm) membrane-bound vesicles called exophers [4]. Exopher production begins with dynamic collection of aggregates within the neuronal soma, concentration at a pre-exopher domain, and later dramatic outward budding of a nearly soma-sized membrane-bound vesicle that can selectively include damaged organelles and toxic proteins [4, 5] (Figure 1A, 1B). Exopher contents can be delivered directly to neighboring tissues (the glia-like hypodermis, in the case of *C. elegans* touch-neuron-derived exophers that we have studied most), similar to what has been observed for *Drosophila* [5-7] and mammalian neurons [2]. We speculate that the *C. elegans* exopher mechanism is analogous to a poorly understood process by which neurodegenerative disease-associated aggregates spread from cell to cell to promote pathology in human

neurodegenerative disease. Thus, mechanistic dissection of exophergenesis and the transfer of exopher contents to neighboring cells within in the informative *C. elegans* genetics model holds potential to provide insight into critical neurodegenerative disease biology.

Mammalian cells can use adapter proteins to collect and link aggregated protein cargoes to dynein motors that transport them via microtubule tracks to juxtanuclear structures called aggresomes [8-10]. Aggresomes, which are thought to be surrounded by intermediate filament meshworks, can be targets for autophagosomes and lysosomes as these organelles attempt degradation of aggresome contents; aggresomes are especially prominent under the stress conditions that result when proteasome and autophagy pathways are overtaxed or impaired. The extent to which mammalian aggresome pathways contribute to spreading mechanisms has not been extensively investigated.

Extrinsic factors (oxidative stress, osmotic stress [11] (which are associated with proteostasis disruption [12, 13]), food availability, presence of eggs ([11, 14] and our unpublished observations)) can markedly influence the level of exopher production. In this study, we sought to identify neuron-intrinsic factors that act to influence exopher production, beginning with a candidate RNAi knockdown approach to rapidly reveal potential molecular players in exophergenesis that included aggresome-associated components. Our follow-up studies identified a cell-autonomous requirement for aggresome-associated intermediate filament (IF) D class proteins IFD-1 and IFD-2 in efficient *C. elegans* exophergenesis. We found that IFD-1 and IFD-2 colocalize to

proteostress-sensitive juxtanuclear inclusions that both associate with aggregating human disease proteins and influence exopher production. We document roles of conserved adapter proteins, dynein motors and microtubule integrity in collection and concentration of offending proteins into IF-associated compartments that are highly reminiscent of mammalian aggresomes and we show that human neuronal intermediate filament hNFL can execute touch neuron-autonomous exopher-related functions in *C. elegans* neurons. Our data contribute molecular documentation of *C. elegans* neuronal aggresome formation and provide the first demonstration of aggresome component contributions to stress-associated extrusion of compromised neuronal contents. Mechanistic linking of conserved aggresome-associated neurofilaments with neuronal extrusion invites focus on associated mechanisms as a novel angle for mammalian study and potential intervention therapies in neurodegenerative disease.

Results

Electron microscopy suggests that intermediate filament-associated aggresomes are present in proteo-stressed *C. elegans* neurons in the early bud phase of exopher production

The dynamic process of exopher-mediated expulsion involves collection and localization of noxious cellular contents, neuronal soma expansion, outward budding of a large membrane-surrounded vesicle that can preferentially concentrate specific cell contents, and the release of the loaded membrane-surrounded nascent exopher into the domain of the neighboring cell [4, 5] (Figure 1A,B). We study exopher biology in a *C. elegans* strain in which the six easily visualized touch receptor neurons express a fluorescent

mCherry reporter at high levels; for simplicity we refer to transgene *bzIs166*[P_{mec-4}mCherry] as mCherry in the text that follows. We note that *C. elegans* exophers can be visualized in dye-filling amphid neurons in the absence of fluorescent reporters [4] and in *C. elegans* muscle cells using fluorescently tagged proteasome or mitochondrial membrane reporters [4, 14]. Thus, the production of exophers is not a response to a specific transgene construction.

During early adult life, the ALMR touch receptor neuron (**A**nterior **L**ateral **M**icrotubule mechanosensory touch neuron, **R**ight side) can bud out a large, nearly soma-sized, vesicle to extrude most of the detectable mCherry fluorophore in one (or less frequently a few) large exopher(s) [4] (example of a touch neuron exopher in Figure 1A, cartoon of budding out exopher production in Figure 1B).

To gain insight into the intracellular events that accompany exopher formation, we examined ultrastructural features of ALM neuron somata from mCherry proteo-stressed touch receptor neurons, focusing primarily on neurons that we visually assessed to be beginning to bud out exophers prior to fixation (morphological stages of exophergenesis described in detail in reference [5]; see Figure 1B). We used high pressure freezing/freeze substitution (HPF/FS) and prepared electron microscopy serial sections from the group of visually selected “early bud” neuron mCherry adult day 2 (Ad2) animals. Electron micrographs generated from twelve distinct neurons revealed that the somata in mCherry-expressing neurons exhibit substantial swelling and contain multiple novel/altered structures.

We noted that the proteo-stressed ALM somas often contained 1-2 μm-sized rounded structures located close to neuronal nuclei (Supplementary Figure 1A-D). These round structures included a central granular matrix. A striking feature of the juxtanuclear structures was their peripheral-association with 10 nm-wide filaments (9.99 nm; > 150 filaments measured, +/- 0.80 SD), a diameter measure consistent with that of Intermediate Filaments (IF). Electron tomograms confirm that these 10 nm filaments can be readily distinguished from membrane bilayers (Supplementary Videos 1, 2).

Data from the twelve neurons we examined suggest a potential “growth/maturation” sequence for the spherical structures. Some of these spherical granular structures contain a patched meshwork-like border of single discontinuous filaments at the periphery, and a few disorganized short loose intermediate filaments inside (Supplementary Figure 1A, B). Some granular structures that may be more advanced in genesis featured a series of longer curved filaments assembled in parallel at the periphery, with each filament remaining separate from its neighbors, and fewer short filaments inside the structure (Supplementary Figure 1C). Finally, some rounded juxtanuclear structures display a periphery of loosely-parallel filaments, with some portions of the border having a densely packed layer of filaments; no internal filament structures evident (Supplementary Figure 1D). We also noted that the electron density of the central granular material appears higher in samples with greater filament association.

Although technical challenges precluded our immuno-EM verification of intermediate filament identification, the structures we documented in mCherry ALM neurons are strikingly reminiscent of maturing mammalian aggresomes that form under high proteostress and are characterized by intermediate filament proteins that coalesce around sequestered aggregated protein [8, 15-17]. Given these ultrastructural data observations, we hypothesized that aggresome-associated intermediate filaments might be important in exopher production.

Intermediate filament proteins IFD-1 and IFD-2 act to promote efficient exopher production

Intermediate filaments (IF) are ~ 10 nm diameter fibers [18, 19]. IFs expressed in neurons (neurofilaments, NFs) influence neuronal structure and intracellular transport [20, 21]. Consistent with critical roles in neuronal function, IFs have been implicated in multiple neurodegenerative diseases and their sequelae [22]. For example, neurofilaments (NFs) can surround aggresomes in neurons that express toxic aggregating proteins [23] and NFs are major components of α-synuclein-containing Lewy bodies that characterize Parkinson's disease pathology [24]. The secretion of NFs in cerebrospinal fluid, and more recently, blood plasma, serves as a highly utilized indicator of neuronal injury and neurodegeneration in human clinical assessment [25]. The precise roles of NFs in neuropathology are not well understood, nor does much data address how NFs come to be secreted components present in CSF and blood plasma.

Given the prominent IF-like structures observed in the EM analysis of proteostressed touch neurons expressing exogenous *bzIs166*[P*mec-4*mCherry] as they begin to produce exopher buds, we first used genetic disruption approaches to test potential requirements for IF proteins in exophergenesis. We found that RNAi targeting of multiple IF genes (in a touch neuron expressing mCherry strain that was engineered to allow RNAi knockdown only in neurons) suppressed exopher levels (Supplementary Figure 2), the first implication of IF functions in large-vesicle extrusions from neurons in a living organism. Given the relatively strong RNAi suppression effects for both members of the IFD subclass *ifd-1* and *ifd-2*, the documented transcriptional expression of *ifd-1* [26] and *ifd-2* [26-28] in touch neurons, and the limited study of the biological roles of the *C. elegans* IFD genes to date [29-33], we pursued genetic confirmation of IFD family members *ifd-1* and *ifd-2* contributions to exophergenesis.

We tested whether null alleles of *ifd-1* and *ifd-2* act as exopher suppressors. We obtained a mutant strain containing the *ifd-1(ok2404)* deletion (1863/1927 base pairs deleted) and used CRISPR/Cas9 technology to generate deletion allele *ifd-2*(*bz187)*, which is missing the start codon and first three *ifd-2* exons. The *ifd-1(Δ)* and *ifd-2(Δ)* mutants exhibited normal or near normal developmental timing (*ifd-2(Δ)* ~5 hour average delay to L4) and longevity (Supplementary Figure 3D-G), WT morphology and brood size (Supplementary Figure A-C). *ifd-1(Δ)* and *ifd-2(Δ)* mutants also exhibited WT osmotic stress survival (Supplementary Figure 3I), normal (*ifd-2(Δ))* or elevated oxidative stress sensitivity (for *ifd-1(Δ)*), (Supplementary Figure 3I) (osmotic and oxidative stresses are associated with proteostasis disruption [12, 13]) and WT or

modest suppression *(ifd-2(Δ))* of baseline *gst-4*::GFP expression (GST-4::GFP is a *daf-16*/FOXO/ SKN-1/NRF responsive glutathione-S-transferase reporter commonly used to report stress conditions [34]), (Supplementary Figure 3J-K). In terms of touch neuron-specific features, we recorded normal touch neuron function and touch neuron morphology during aging (Supplementary Figure 4A-B). Likewise, distribution and extent of mCherry collection is not markedly changed in touch neurons when *ifd-1* or *ifd-2* are deleted (Supplementary Figure 4C-D). We conclude that *ifd-1* and *ifd-2* deletions do not confer substantial consistent systemic physiological disruption in the whole animal or markedly perturb the basic biology of the touch neurons in which we characterize exophergenesis.

We crossed the *bzIs166*[P_{mec-4}mCherry] reporter into the *ifd-1(Δ)* and *ifd-2(Δ)* backgrounds and measured exophers at Ad2. We found that *ifd-1(Δ)* and *ifd-2(Δ)* each suppress exopher production (Figure 1C), confirming initial RNAi outcomes and establishing a role for *C. elegans* IFDs in promoting exopher formation. To confirm exopher suppression in a reporter background different from transgenic mCherry, we crossed *uIs31*[P_{mec-17}GFP] (a *mec-17* promoter-driven cytosolic-GFP transgene commonly used as a cytoplasmic touch neuron reporter), with *ifd-1(Δ) and ifd-2(Δ)* and measured exophers at Ad2. Both *ifd-1(Δ)* and *ifd-2(Δ)* deletions significantly suppress exophers visualized with the GFP marker (Supplementary Figure 5). Thus *ifds* appear to act generally – affecting exopher outcomes in multiple reporter backgrounds, rather than altering a specific cellular response to elevated mCherry expression.

Despite the fact that null alleles of *ifd-1* and *ifd-2* remove extensive protein coding sequences, neither *ifd-1(Δ)* nor *ifd-2(Δ)* fully eliminated exophers, suggesting that *ifd-1* and *ifd-2* might function in redundant pathways that promote exopher formation. To address whether *ifd-1* and *ifd-2* might act in the same, or in parallel, pathways in exophergenesis, we constructed an *ifd-1(Δ)*; *ifd-2(Δ)* double mutant and compared exopher levels to those in single *ifd* mutants (Figure 1C). We found that exopher production in the *ifd-1(Δ); ifd-2(Δ)* double mutant was suppressed to the same extent as in the single mutants, suggesting that *ifd-1* and *ifd-2* are likely to act in the same pathway to influence exopher production.

Intermediate filament proteins IFD-1 and IFD-2 act touch neuron autonomously to promote exopher production

We created a single-copy GFP::IFD-2 transgene, expressed from the native *ifd-2* promoter, and tested for rescue of the *ifd-2(Δ)* phenotype. *bzSi76*[$P_{ifd\text{-}2}$GFP::IFD-2] rescues the *ifd-2(Δ)* exopher deficit, confirming the *ifd-2* gene role in modulating exopher levels as well as demonstrating functionality of the GFP::IFD-2 fusion protein (Supplementary Figure 9A).

IFD-1 and IFD-2 were previously reported to be primarily expressed in the intestine [32], although single cell sequence data indicates their expression in touch neurons as well [26-28]. To test for a cell-autonomous role for IFDs in neuronal exopher production, we expressed single-copy fluorescently-tagged reporters exclusively in the touch receptor neurons under the control of the touch neuron promoter *mec-7*. We added GFP to the

N-terminus of IFD-1 and mNeonGreen to the N-terminus of IFD-2, and used miniMos technology [35] to introduce the transgenes in single copy; we also crossed mCherry into the background to enable soma and exopher tracking and to modestly potentiate exopher production. We introduced the *bzSi3*[P_{mec-7}GFP::IFD-1] and *bzSi37*[P_{mec-7}mNeonGreen::IFD-2] transgenes into cognate *ifd* deletion backgrounds and assayed ALMR exopher production at Ad2. We found that single copy *bzSi3*[P_{mec-7}GFP::IFD-1] rescues the exopher deficit phenotype of the *ifd-1(Δ)* mutant (Figure 1D). Similarly, single copy *bzSi37*[P_{mec-7}mNeonGreen::IFD-2] rescues the exopher deficit phenotype of the *ifd-2(Δ)* mutant (Figure 1E). Touch-neuron-specific genetic complementation supports cell-autonomous activity for IFDs in exophergenesis.

Because *ifd-2* is also expressed in the intestine [36] (Supplementary Figure 8) and mutants can have intestinal morphology defects [32], we also tested for rescue of the neuronal exopher phenotype in a single copy *bzSi45*[P_{vha-6}mNeonGreen::IFD-2]; mCherry line, in which mNeonGreen::IFD-2 is specifically expressed in the intestine. We find that intestinal expression of mNeonGreen::IFD-2 does not rescue the neuronal exopher phenotype of *ifd-2(Δ)* (Supplementary Figure 10), consistent with a driving role for *ifd-2* in exophergenesis that lies outside of the intestine.

In sum: 1) touch neuron-specific rescue of the exopher support that IFD-1 and IFD-2 likely act touch neuron autonomously to influence exopher production; and 2) fluorescently tagged IFD-1 and IFD-2 proteins confer functional complementation of

exophergenesis and are therefore likely to localize to, and indicate the identity of, the native subcellular compartments in which they are bioactive.

Elevated gene dosage of *ifd-1* or *ifd-2* neither increases, nor dominant-negatively suppresses, exophergenesis. We wondered whether enhanced expression of *ifd* genes might drive exopher formation. To address the potential impact of elevated *ifd* gene dosage on exopher levels, we quantitated exophers under conditions of high gene copy rescue accomplished with extrachromosomal arrays. We find that a high copy number *ifd-2* transgene rescues the cognate *ifd-2(Δ)* allele (Supplementary Figure 6B), but does not drive higher levels of exophergenesis than occurs in *ifd*+ mCherry controls (Supplementary Figure 13D), suggesting that the *ifd*-dependent mechanisms influencing exopher levels are unlikely to be anchored in simple elevated *ifd-2* expression.

We also note that high copy number *ifd* transgenes in *ifd-1(Δ)* or *ifd-2(Δ)* mutants do not confer dominant negative effects on exophergenesis (Supplementary Figure 6), suggesting that *ifd* influence on exopher production is unlikely to depend on stoichiometric interactions with concentration-limited partner proteins.

Finally, we did detect some capacity for high copy number trans-complementation of *ifd-2* for *ifd-1* and *visa versa* (Supplementary Figure 6A,C), suggesting that despite the clear genetic requirements for both *ifd-1* and *ifd-2* for normal exopher production levels (Figure 1C), over-expression of these closely related intermediate filament proteins can provide partial functional substitution (Supplementary Figure 6A,C).

IFD-1 and IFD-2 colocalize in juxtanuclear foci that are distinct from Golgi, lysosomes and mitochondria

Specialized cellular distribution can inform on protein function, and thus we studied the subcellular localization patterns of functional fluorescently tagged GFP::IFD-1 and mNeonGreen::IFD-2 proteins expressed in touch neurons from single copy transgenes. We found that in the mCherry background, GFP::IFD-1 and mNeonGreen::IFD-2 typically appear in one to three ~ 1 µm foci located near the nuclear membrane (Figure 2A-B, Supplementary Figure 11A, Supplementary Figure 12), with two IFD foci being most commonly observed during early adult life (Supplementary Figure 11A). The IFD foci increase in size from L4 to later adulthood (Figure 2C, Supplementary Figure 11B). GFP::IFD-1 foci assembly and overall size does not depend on *ifd-2* (Supplementary Figure 7). Of note, the IFD foci appear akin in size and position to the 10nm-diameter filament-associated structures we observed in EM in the absence of expressed tagged IFD proteins (Supplementary Figure 1).

We found that similar concentrated juxtanuclear IFD foci can be visualized using multiple different fluorescent reporter-tagged versions of IFD-1 and IFD-2 (*i.e.,* for mNeonGreen, RFP, and mScarlet fluorescent tags (Supplementary Figure 12)), indicating that the subcellular localization pattern of IFDs is independent of fluorescent tag identity. Elevated expression of the tagged *ifd-1* or *ifd-2* reporters does not change subcellular localization or alter exopher levels (Supplementary Figure 7, Supplementary Figure 12). Although we could not detect expression from native *ifd* promoters or native

ifd transgenes in touch neurons (Supplementary Figure 8) (a reporter outcome we often observe for native promoter-single copy reporters including touch neuron channel *mec-4*, dynein heavy chain *dhc-1*, and *rab-11,* a GTPase required for recycling endosome function, for example [37, 38]), the functional complementation and rescue of the IFD reporters, lack of dominant negative effects of expressed *ifd* reporter transgenes, and consistent localization of different reporter fusion proteins to the same distinctive subcellular site (see below) support that IFD-1 and IFD-2 normally concentrate into juxtanuclear foci in proteo-stressed touch neurons.

To determine whether IFD-1 and IFD-2 colocalize with each other in the juxtanuclear foci, we tested for co-incidence in strains that expressed both GFP::IFD-1 and RFP::IFD-2 in touch neurons (Figure 2D). We find that GFP::IFD-1 and RFP::IFD-2 signals are nearly completely colocalized (quantitation in Figure 2H), consistent with genetic data that suggest that IFD-1 and IFD-2 influence exophers via the same pathway (Figure 1C).

To address whether the juxtanuclear IFD foci correspond to known cell organellar compartments, we tracked IFD-1 and IFD-2 localization relative to Golgi, lysosomes, and mitochondrial reporters. We found that tagged IFD proteins did not colocalize substantially with Golgi marker AMAN-2::tagBFP (Figure 2E, I), late endosome and lysosome marker LMP-1::mScarlet (Figure 2F, J), or mitochondria tagged with MitoROGFP (Figure 2G, K). Thus, our data support that the IFDs localize to a neuronal compartment distinct from Golgi, lysosomes, and mitochondria.

IFD foci are homologous to mammalian aggresomes

Under high proteostress conditions, ubiquitinated and non-ubiquitinated aggregated proteins in mammalian (and other) cells can be linked to adapters such as HDA-6/HDAC6, SQST-1/p62, and the HSP-1/BAG3/14-3-3 complex that connect to dynein motors and move along microtubule tracks to juxtanuclear sites to deposit aggregate cargos [39-41]. IFs concentrate at these juxtanuclear sites, which are called aggresomes. Since our data reveal juxtanuclear concentration for IFDs and implicate IFDs in the proteostress response of exophergenesis, we tested the hypothesis that IFD foci are *C. elegans* aggresome counterparts by manipulating facets of aggresome biogenesis and probing for colocalization of IFDs and aggresome proteins reported in the mammalian literature.

To test microtubule (MT) requirements for juxtanuclear IFD concentration, we treated $P_{mec\text{-}7}$GFP::IFD-1 expressing animals with the potent microtubule inhibitor colchicine [42, 43] from L4 to Ad2 (Figure 3B-C, Supplementary Figure 15A-B). We find that colchicine increases the number of dispersed GFP::IFD-1 foci, reduces their size, and disrupts the juxtanuclear concentration, suggesting a requirement for MTs in the development and juxtanuclear localization of the *C. elegans* IFD compartment, as occurs for mammalian aggresomes.

Colchicine treatment acts systemically and could act via non-autonomous influences, and thus we also used the auxin-inducible degradation system [38] to degrade dynein

heavy chain component DHC-1 specifically in touch neurons. We introduced a degron-tagged *dhc-1* allele into a strain engineered for touch neuron-specific expression of the ubiquitin ligase adapter TIR1, which promotes rapid degradation of degron-linked sequences when auxin is added to the culture. We treated animals with auxin from L4 to Ad2 to enable auxin-promoted degradation of DHC-1::degron and scored GFP::IFD-1 inclusions. We found that in the presence of auxin (and therefore when DHC-1::degron was degraded), IFD inclusions were small, mobile, dispersed, and more numerous than in controls (Figure 3D-E, Supplementary Figure 15C-D). We conclude that a touch neuron-expressed DHC-1-containing dynein motor acts cell autonomously in IFD collection and concentration into large juxtanuclear inclusions, similar to dynein motor roles in mammalian aggresome formation.

We also tested for molecular associations of IFDs with homologs of aggregate adapter proteins documented to contribute to, and associate with, mammalian aggresomes. Mammalian aggregate collection and delivery to aggresomes occurs via at least three distinct molecular adapters that link aggregates to dynein motors for MT transport to juxtanuclear IF-rich inclusions [8, 41, 44, 45]: SQSTM1/p62 autophagy/adapter, HDAC6 deacetylase, and 14-3-3 protein, the latter of which functions in an adapter complex that includes BAG3 and chaperone Hsc70 [45] (Figure 3A). We constructed strains harboring GFP::IFD-1 and tagged *C. elegans* homologs of *sqst-1*/SQSTM1, *hsp-1*/HSP1 and *ftt-2*/14-3-3. For each adapter tested, we find colocalization with the juxtanuclear GFP::IFD-1 protein, akin to their characterized mammalian counterparts (Supplementary Figure 20G, Figure 3F-G).

Mammalian aggresomes can collect ubiquitinated proteins [8, 46, 47] and therefore we also asked whether IFD inclusions colocalize with sites of ubiquitin concentration. We co-expressed single copy transgene mNeonGreen::UBQ-2 in touch neurons together with mScarlet::IFD-1 (Figure 4A) or mScarlet::IFD-2 (Figure 4B) and found that although some fluorescently tagged ubiquitin is dispersed or concentrated elsewhere in the neuronal soma as expected, mNG-tagged ubiquitin also concentrates in the IFD-1 and IFD-2 inclusions. We conclude that, like mammalian aggresomes, the *C. elegans* neuronal juxtanuclear IFD inclusions are associated with concentrated ubiquitinated proteins. Data highlight the homology of formation and composition between the *C. elegan's* neuronal IF structures and mammalian aggresomes.

C. elegans aggresomes can include neurotoxic HttPolyQ aggregates

Ubiquitin colocalization (Figure 4A-B) is suggestive of concentrated misfolded/ aggregated proteins. To address whether a characterized toxic aggregating human neurodegenerative disease protein can concentrate in the IFD-aggresome inclusions, we focused on polyglutamine expansion proteins, which have been found to aggregate and stress *C. elegans* neurons [48, 49]. We constructed and co-expressed a single copy transgene encoding mNG::HttQ74, which includes much of the first exon of the human Huntingtin gene fused to a HttQ74 expansion [50], together with mScarlet::IFD-1 or mScarlet::IFD-2 reporters. We identified strong localization of mNG::HttQ74 to IFD-1 and IFD-2 inclusions in the touch neuron soma (Figure 4C-D) when mNG::HttQ74 is expressed at levels at which visible aggregation is present. We also examined a

published HttQ128::CFP line expressed from an integrated high-copy-number array along with mScarlet::IFD-1 and observed coincident fluorescence (Figure 4E). Our data establish that expanded polyglutamine proteins can concentrate at IFD inclusions, consistent with the idea that IFDs mark and sequester a domain of aggregated protein, and similar to what has been reported for mammalian aggresomes.

Interestingly, we did not measure differences in HttQ74 aggregate or ubiquitin concentration numbers or size in the *ifd-2(Δ)* background (Supplementary Figure 4E-I), indicating that major changes in the overall distribution of aggresome cargos are unlikely to explain the exopher production deficit in the *ifd-2(Δ)* mutant.

It may be noteworthy that we found that IFDs and HttQ128::CFP associations can adopt multiple relative configurations, with IFDs and polyQ aggregates being mostly coincident for smaller (presumptively newly formed) aggresomes in early adult life (Figure 4C-D), but more frequently exhibiting less complete “covering” with advancing time or when relative expression of HttQ128::CFP and IFDs appears unbalanced (Figure 4E, Supplementary Figure 16).

We also characterized the localization of highly expressed touch-neuron mCherry, relative to IFD foci. mCherry *bzIs166*[$P_{mec\text{-}4}$mCherry] expression marks touch neurons and exophers and increases proteostress to elevate baseline exopher numbers; mCherry can concentrate into particular subcellular foci [4, 5]. Our imaging data suggest that there are multiple pools of mCherry in the cell. We found dimmer mCherry

concentrations colocalized with IFD-1 in very few ALM neurons, but most highly concentrated mCherry in touch neuron somata was within LMP-1::GFP positive structures (LMP-1 is the lysosomal membrane protein LAMP1 ortholog [51]; Supplementary Figure 17B). Thus, although mCherry is a powerful transgenic reporter that allows visualization and identification of exophers and touch neurons [4, 5, 11], the mCherry concentration in the cell is most likely to reflect lysosomal collection and does not strictly align with that of the IFD-associated aggresome. That exophers are filled with heterogenous cargo has been well documented at the cell biological and EM levels [4].

In summary, colocalization analyses indicate that cargoes of different character (*i.e.*, expanded poly-Q proteins and mCherry) are differentially handled, concentrated, and/or stored prior to expulsion within exophers, and that the expanded polyQ proteins associate with, and linger within, IFD inclusions in proteostressed neurons (Figure 4C-D, Supplementary Figure 16, Supplementary Figure 17).

IFD-positive foci can be expelled within exophers, but not all exophers contain IFD-1 foci

A critical question in deciphering the roles of IFDs in exophergenesis is whether the IFD inclusions are themselves expelled from the soma within exophers, and if so, whether IFD inclusion is mandatory for exophergenesis. We examined exophers in a strain that co-expressed mSc::IFD-1 and mNG::HttQ74 after 6 hours of food withdrawal, a culture condition that increases exopher production [11]. Focusing first on the simplest question

of whether IFD-1 can be extruded into exophers, we found that out of 30 total exopher events we scored, 14 included detectable mSc::IFD-1 (Supplementary Figure 18A-B, (top)), establishing that tagged intermediate filament mSc::IFD-1 can be extruded in exophers. To our knowledge, this is the first documentation of the active extrusion of an intermediate filament-containing aggresome from a neuron, of basic interest as circulating human neurofilaments are clinical manifestations of neuronal stress and neurodegeneration.

We also quantitated GFP::IFD-1 ejection in the *bzIs166*[$P_{mec\text{-}4}$ mCherry] background. We find that GFP::IFD-1 foci can be co-extruded in about 15% of exopher events in the mCherry background (Supplementary Figure 19A-B). Interestingly, entire aggresome contents of the soma were ejected in 4/9 exopher events; the remaining 5 cases had one GFP::IFD-1-aggresome focus in soma and one in the exopher (Supplementary Figure 19C). Since mSc::IFD-1 and GFP::IFD-1 are present in only some of the exophers formed in a particular background (~ 50% (HttPolyQ) or ~15% (mCherry)), we conclude that IFD-1 extrusion is not a mandatory mechanistic requirement in all exophergenesis events.

Ejected IFD foci colocalize with mNG::HttQ74 in most extrusion events

To assess the IFD-1 status relative to ejected cargo, we looked at the mNG::HttQ74 overlap with the mSc::IFD-1 that were ejected in exophers (*i.e.*, in exophers that included mSc::IFD-1 puncta/ae). Of the 14 mSc::IFD-1-positive exophers we reported in Supplementary Figure 18B bottom, 11 exophers contained species in which mSc::IFD-1

and mNG::HttQ74 colocalized to the same puncta; only 3 exopher events had mSc::IFD-1 foci in exophers(s) that lacked co-enrichment of mNG::HttQ74 (Supplementary Figure 18B). We conclude that IFD-1-aggresomes hosting HttQ74-cargo are often components of extruded exophers in this test strain.

In a complementary analysis focused on cases in which HttQ74 aggregates leave the cell, we looked at the same 30 exopher events with an initial scoring of the mNG::HttQ74 reporter, and later checking for co-association of the IFD reporter. We found that 22 of the 30 exophers contained at least one identifiable mNG::HttQ74-enriched punctum (Supplementary Figure 18C top). Of those 22 exopher events that included mNG::HttQ74 punctae, we asked whether the ejected HttQ74 was accompanied by IFD-1. We found 11 out of 22 exophers also displayed mSc::IFD-1 colocalized with mNG::HttQ74 (Supplementary Figure 18C bottom). Data indicate that HttQ74-aggregates are often extruded into exophers as IFD-1^{+} aggresomes, although HttQ74 can leave the soma in the exopher compartment nearly as frequently without co-IFD-1 association. We conclude that IFD-1 association is not strictly required for HttQ74 extrusion.

Adapter proteins SQST-1 and FTT-2 promote aggresome collection but are not essential for GFP::IFD-1 aggresome formation

We reasoned that if IFDs engage aggresome biology to influence exopher production, disruption of homologs of adapters that influence mammalian aggresome loading might also modulate aggresome features. To test this possibility, we examined available

viable mutants for *C. elegans* counterparts of three aggregate collection pathways: *hda-6*/HDAC6, *sqst-1/*SQSTM1, and *ftt-2*/14-3-3. We scored aggresome dimensions as reported by GFP::IFD-1 in adapter mutant backgrounds (Supplementary Figure 20A-B, D-E, Supplementary Figure 21A-B).

We find that no individual adapter disruption eliminates the IFD compartment. Thus, no single aggregate collection pathway appears essential, and multiple routes likely function in parallel for aggresome delivery, consistent with reported mammalian biology [45, 52].

We did quantitate some change in aggresome dimensions in *sqst-1(ok2892),* in which ALM touch neurons have significantly smaller GFP::IFD-1 puncta, with increased puncta numbers (Supplementary Figure 20D-E). Likewise, *ftt-2(n4426)* ALMs have significantly smaller GFP::IFD-1 aggresomes without a change in number of aggresomes per neuron (Supplementary Figure 21A-B). Changes in aggresome features are consistent with roles for SQST-1 and FTT-2 in GFP::IFD-1-reported aggresome filling.

Adapter proteins SQST-1, HDA-6, and FTT-2 modulate exopher production

Regarding exopher production, we found that *sqst-1(ok2892)* increases variation in exopher levels, but overall we find no significant change in exopher number compared to WT in the *sqst-1* mutant (Supplementary Figure 20F). Enhanced variation might be attributed to the roles SQST-1 plays in both aggresome formation and autophagy (autophagy disruption usually increases exopher levels as reported in ref. [4], and in

Supplementary Figure 11E). *hda-6(ok3204)* (which did not significantly impact GFP::IFD-1 formation) increased exopher levels (Supplementary Figure 20A-C) which might reflect summed multiple roles tubulin cytoskeletion and aggresome loading.

The 14-3-3 mutant *ftt-2(n4426),* which induced a significant reduction in aggresome size (Supplementary Figure 21A-B), exhibits a clear exopher suppressor phenotype (Supplementary Figure 21C). Testing *ftt-2(RNAi)* impact on exophers in both touch neuron-sensitized and neuron-specific RNAi backgrounds, we find a suppression of exopher formation (Supplementary Figure 22B-C). We conclude that 14-3-3 protein FTT-2 positively influences exopher levels.

14-3-3 protein FTT-2 can promote exopher formation

To test touch neuron (TN) autonomy of *ftt-2* impact on exopher production we introduced a single copy of *ftt-2* expressed from the touch neuron *mec-7* promoter (P_{mec-7}FTT-2::mSc; P_{mec-4}mCherry) in an otherwise WT *ftt-2(+)* background. When we tested exopher levels in this strain, which is wild type *ftt-2* at the endogenous genomic locus and harbors a second copy of P_{mec-7}FTT-2::mSc inserted via MiniMos single site insertion (i.e. elevated *ftt-2* expression), we quantitated significantly increased TN exopher levels (Supplementary Figure 21D) [53]. Data support cell autonomous activity of FTT-2 in exopher modulation and suggest that enhanced FTT-2 activity can drive exopher formation.

To assess additional requirements of the BAG3/HSP-1/14-3-3 adaptor complex protein FTT-2 in exopher biology we knocked down *hsp-1/Hsc70* [39] (Supplementary Figure 22A). RNAi against *hsp-1* significantly reduced exophers in an RNAi strain engineered to enhance knockdown in touch neurons via expression of SID-1 dsRNA transporter (Supplementary Figure 22D). Results suggest that the FTT-2 aggresome-related binding partner, HSP-1, plays a role in touch neuron exophergenesis and support that a FTT-2/HSP-1 complex can act to modulate exopher levels.

Taken together, our data both support a partial conservation of aggresome-related mechanisms from nematode to human and implicate a role for the aggresome components in modulation of exopher levels.

Human neuronal intermediate filament protein hNFL can complement *C. elegans* *ifd-2* deletion to promote exopher formation

Mammalian intermediate filament proteins are integrated into the neuronal proteostasis network and can associate with juxtanuclear aggresomes [8, 23, 54, 55]. Roles for mammalian IFs in neuronal aggregate extrusion have not been reported, but our *C. elegans* observations raise the possibility that higher organism neuronal IFs might act in exopher-related biology [56, 57]. To begin to address this possibility, we asked if a human neuronally-expressed intermediate filament protein can complement an *ifd(Δ)* for exopher production deficits.

We focused on testing human neurofilament light chain (hNFL) because hNFL is a mammalian neuron-specific intermediate filament protein and hNFL exhibits ~24/45%

sequence identity/similarity to *C. elegans ifd-1* and *ifd-2* (for comparison, human Bcl2 and *C. elegans ced-9,* homologs demonstrated to complement for apoptosis regulation across species [58], score as 24/43% identity/similarity). Moreover, human NFL is clinically evaluated as a circulating blood/CSF biomarker of neuronal injury and neurodegenerative disease [59, 60], despite mysteries surrounding its origins in circulation.

We optimized the human NFL gene for expression in *C. elegans* based on codon bias and inclusion of short introns using *C. elegans* Codon Adapter Software [61]. We first documented the subcellular distribution of the tagged mNG::hNFL expressed under the direction of a *mec-7* promoter from a single copy insertion in touch neurons (Supplementary Figure 23). mNG::hNFL concentrated to juxtanuclear foci that colocalize with *C. elegans* intermediate filament reporter mSc::IFD-1 (Figure 5A). mScarlet::hNFL colocalizes with ubiquitin, mNG::UBQ-2 (Figure 5B), and with mNG::HttQ74 (Figure 5C) in aggresome compartments. Although the predominant localization of mNG::hNFL is to one or two punctate juxtanuclear locations (Supplementary Figure 23D, quantified in Supplementary Figure 23F-K with both single copy and high copy mNG::hNFL reporters), we did note that FP-tagged hNFL could also be distributed more broadly in the neuron as compared to *C. elegans* FP::IFDs, also appearing in the axon, nucleus, and in filamentous patterns in the cytoplasm in some neurons (Supplementary Figure 23A-C). Nonetheless, *C. elegans* IFDs and hNFL clearly localize similarly to aggresome compartments.

Having documented distribution of human hNFL that reflects that of *C. elegans* IFDs at aggresomes, we introduced the $P_{mec\text{-}7}$mNG::hNFL single copy transgene into an *ifd-2(Δ);* mCherry background and compared exopher production in *ifd-2(Δ)* vs. *ifd-2(Δ)*; $P_{mec\text{-}7}$mNG::hNFL. Single copy $P_{mec\text{-}7}$mNG::hNFL can partially rescue *ifd-2(Δ)* exopher deficits (P = 0.0046; Figure 5E). The mNG::hNFL single copy construct, similarly to tagged IFD constructs, does not significantly elevate or suppress exopher levels on its own, indicating that the rescuing activity is unlikely to be caused by transgenic protein aggregation (Supplementary Figure 24). hNFL rescue of *ifd-2(Δ)* exopher deficits supports that human neuronal intermediate filament protein hNFL can likely serve a conserved role in *C. elegans* exopher biology and suggests a novel potential cellular activity for hNFL in extrusion of human neuronal materials.

Can hNFL itself be extruded via an exopher-like mechanism? Akin to what we documented for the *C. elegans* IFD-aggresome (Supplementary Figure 18A-B, Supplementary Figure 19A-B), we found that hNFL inclusions are expelled within approximately half of *C. elegans* exophers (Figure 5D).

In sum, our finding that human hNFL partially compensates for *ifd-2* function (Figure 5E), shows overlapping subcellular localization with *C. elegans* IFD and aggresome components (Figure 5A-C), and is expelled from the soma in exophers (Figure 5D), raises the possibility that mammalian IFs may play roles in cellular extrusion that are conserved from nematodes to humans, inviting the re-examination of mammalian aggresome biology in the context of mechanisms of human aggregate spread.

Discussion

Overview and Significance. The fundamental mechanisms by which proteo-stressed neurons manage toxic aggregates and damaged organelles remain a central question in neurodegenerative disease [2]. In mammals, processes strikingly similar to *C. elegans* exophergenesis have recently been described for HeLa cells [62], PC12 cells [62], and *in vivo* extrusions from mouse cardiomyocytes [63, 64][65, 66]. Moreover, *in vivo* transcellular extrusion of mitochondria from retinal ganglion cells for degradation by neighboring cells is reminiscent of exopher-like biology, and transcellular extrusion and degradation is increased in mouse AD model brain and observable in human neurodegenerative diseased brain [67]. Emerging data thus highlight a newly identified cell strategy for offloading aggregates and organelles that may operate across phyla. Although molecular links among the associated extrusion events remain to be rigorously established, initial observations are consistent with the hypothesis that exopher-like responses are within the capacity of a variety of stressed cells in a range of tissues across organisms (see review on heterophagy, ref. [68]).

Here we report on initial steps toward deciphering mechanisms by which *C. elegans* neurons transfer neurotoxic contents out of the cell in large exopher extrusions, finding that specific intermediate filament proteins IFD-1 and IFD-2 are required within the stressed neuron for efficient exophergenesis. At the cell biological level, intermediate filament proteins IFD-1 and IFD-2 concentrate into stress-responsive juxtanuclear

puncta that are strikingly analogous in position and composition to what has been reported for mammalian aggresomes; additional cargo adapter/aggresome component 14-3-3/FTT-2 is also needed for efficient exophergenesis. The conserved nature of the associated biology is suggested by our finding that expression of human neuronal intermediate filament protein hNFL in *C. elegans* neurons can localize to the IF-aggresome and functionally substitute for *C. elegans ifd-2* in exopher production.

Stressed *C. elegans* neurons produce aggresomes similarly to stressed mammalian cells. The original description of mammalian aggresomes (focused in CHO and HEK cultured cells) defined multiple aggresome features, including prominent juxtanuclear concentration of aggregates with distinct localization from Golgi and lysosomes, association with intermediate filaments under proteostress conditions (aggregate-prone protein over-expression or inhibition of the proteasome), colocalization with ubiquitinated and heterogeneous cargoes, and requirements for microtubule and dynein motor integrity for biogenesis [8]. Follow up studies established that p62/SQST1, HDAC6, and the 14-3-3/BAG3/HSP1 complex associate with small foci that move into the large perinuclear aggresome [39, 69]. Most of these mammalian aggresome features are in common with the IFD-associated puncta in proteo-stressed *C. elegans* touch neurons, including collection of aggregated polyQ protein, enrichment in folding chaperones, ubiquitin, and dynein motor adapters, and a requirement for intact microtubules and dynein activity to collect such materials into one or two

juxtanuclear sites. FTT-2/14-3-3, and possibly the associated chaperone partner HSP-1/Hsc70, aggresome formation components, impact exopher levels.

Aggresome appearance associated with the expression of human neurodegenerative disease proteins [70, 71] or ROS stresses [72] has been reported for *C. elegans* cells, but the data we present contribute the first multi-component characterization of *C. elegans* neuronal aggresomes and definitively establishes that aggresome formation mechanisms are at least partially conserved from nematodes to humans. *C. elegans* are thus a legitimate model for deciphering the relative role of aggresomes in maintaining neuronal proteostasis in an *in vivo* context.

Our molecular identifications of specific intermediate filaments and 14-3-3 data intersect with increasing documentation of intermediate filament roles in proteostasis modulation. Adult mammalian neural stem cells rely on IF vimentin-associated aggresomes to activate proteostasis during quiescence exit, with IF vimentin, at the aggresome site, serving in spatial organization of proteasomes to the aggresome [73]. In mouse primary neuronal culture models of alpha-synuclein spread, 14-3-3θ protein promoted release of alpha-synuclein [74]. Detailed study of these processes in multiple models may thus further underscore commonalities of mechanism.

Aggresome development in a transparent animal.

Ultrastructural analysis of the early bud stage of exophergenesis suggests the assembly of a juxtanuclear domain surrounded by intermediate filament-sized fibers that may

progressively mature to a mesh-like structure *in vivo* (Supplementary Figure 1). The literature on aggresome growth and assembly details is limited, and it has been suggested that in HEK cell aggresome biogenesis, early seeding of an aggresome requires biogenesis factors, but later major expansion might occur via cargo diffusion [75].

Detailed mechanisms of aggresome development and maturation should be genetically and cell biologically tractable in physiological context in the *C. elegans* model, with findings coupled to assays of exophergenesis to expand on the molecular relationship of aggresomes, aggregate loading, and aggregate extrusion.

Our data also suggest that intermediate filament assembly at polyQ aggregates may follow a complex biogenesis in which “coverage” of aggregates with IFDs (i.e., co-localization) appears complete initially (at the young adult time in which neuronal exopher production is at its early peak), but with time, the polyQ collection domain supersedes the IFD capacity to fully surround the large aggregate. We noticed that under single copy expression of tagged IFD and HttQ74 reporters, extensive co-localization of IFD and aggregates is common; but when HttQ128 is highly expressed from multi-copy transgenes, IFDs do not fully envelop HttQ128 (Supplementary Figure 16) and the proportion of HttQ128 to IFD increases. Noteworthy is that dynamic patterns of polyQ concentration have also been reported *in vivo* in *C. elegans* [76] and in HEK cells [77], however functional significance and relationship to IFs have not been parsed out.

In mammals, some IFs “uncoat” from aggresomes prior to lysosome-mediated degradation for internal content degradation in a mechanism that involves subunits released from over-stressed proteasomes [78, 79]. It is interesting to speculate that partial coverage, or “uncoating”, induced under high proteostress or later in life might compromise an exophergenesis trigger. The impact of partially associated configuration of IFs and HttPolyQ on neuronal health awaits detailed study.

Aggresomes engage distinct cargos in different ways. The contents of *C. elegans* exophers are highly heterogeneous and can include multiple protein cargos and a range of organelles in a final common extrusion vesicle [4, 80]. Some of this distribution may be accomplished by collection of specific targets into aggresome-like compartments via multiple pathways, at least one of which is the 14-3-3/HSP-1 route. We find that aggregating polyQ co-localizes primarily to aggresomes, but in contrast, highly expressed mCherry is mainly loaded into lysosomes prior to extrusion in exophers. Thus, although both polyQ and mCherry cargos are loaded into exophers their pre-exit soma concentration and storage strategies are different.

Aggregates, intermediate filaments, aggresomes, and extrusion. Our data implicate aggresome-associated proteins that collect, and associate with protein aggregates, in modulating exophergenesis levels, and by extension, our findings raise the possibility that aggresome structures play significant roles in influencing mammalian aggregate extrusions. The documentation of multiple IFs and aggregate collection factors (IFD-1/IF, IFD-2/IF, hNFL, FTT-2/14-3-3, HSP-1/HSP1) localized to the same soma

compartment with shared functional capacity to modulate exopher extrusion levels support an intersection between aggresome biology and extrusion. How aggregates interface with IFs at the aggresome compartment, and the precise function of intermediate filaments associated with these compartments, remains to be clarified.

Literature suggests that IF vimentin is actually not necessary for either basic cellular function or aggregate collection at the juxtanuclear aggresome [73]; our molecular identifications of specific intermediate filaments and 14-3-3 proteins intersect with increasing documentation of these proteins in mammalian proteostasis modulation [73, 81], rather than aggresome formation *per se*. Adult mammalian neural stem cells rely on IF vimentin for normal activation of proteostasis and aggregate elimination during NSC quiescence exit, with vimentin implicated in spatial organization of proteasomes and autophagosomes to the aggresome domain [73]. In mouse primary neuronal culture models of alpha-synuclein spread, 14-3-3θ protein promoted release of alpha-synuclein [74]. The mature IF meshwork could act as a proteostasis-linked signaling scaffold around aggresomes, promoting internal degradation under balanced proteostasis but exophergenesis under highest stress activation. 14-3-3 proteins might influence aggresome loading, aggresome decoration, or might drive cytoskeletal rearrangements needed for extrusion [82, 83]. Future study of IFs and 14-3-3 with attention to exopher-related biology is likely to further underscore commonalities of extrusion mechanisms across phyla.

Refining understanding of *in vivo* biology that influences exopher formation. Our studies address multiple hypotheses regarding the aggresome/exopher connection, to influence refinement of exophergenesis models.

1) IFDs exert neuron-intrinsic influences on exophergenesis. Although *ifd-1* or *ifd-2* deficiency might be hypothesized to induce or inactivate a systemic stress response, we document multiple examples of touch neuron-specific rescue of exophergenesis deficits, and find few changes in stress and health indicators at the nervous system-wide or organism-wide levels in *ifd* null deletion backgrounds. Our data support a touch neuron-autonomous role in extrusion efficiency for IFD-1 and IFD-2 rather than general roles in animal or neuronal health.

2) Aggresome compartment size is not correlated with exopher production levels. Measures of the aggresome compartment relative to Ad2 extrusion in different mutant backgrounds do not support correlation of aggresome compartment dimensions with exopher levels (Supplementary Figure 14). Aggresome size increases with age; but exopher production levels do not rise in a corresponding temporal pattern (Supplementary Figure 11B). We conclude that the exophergenesis trigger is not directly responsive to aggresome compartment size and infer that if compartment volume influences transfer, additional molecular conditions must also be met prior to exopher extrusion (Supplementary Figure 14).

3) Modulation of *ifd* expression is unlikely to be a driving component of the exopher mechanism. Since *ifd* over-expression is not sufficient to induce

exophergenesis, *ifd* expression modulation is unlikely to drive the exopher level (Supplementary Figure 6, Supplementary Figure 13).

4) Elevated *ifd* expression does not exert dominant negative effects on exophergenesis, suggesting that IFD action in promoting exophers does not require association with a rate-limiting interaction partner (Supplementary Figure 13).

5) Concentrated aggresome-like IFDs can be eliminated in exophers. IFD-marked aggresome foci can frequently leave the neuron together with cargo (Supplementary Figure 18). It is not uncommon that the entire aggresome content of the soma-exopher pair exits the soma (Supplementary Figure 19C); nor is it uncommon to observe one aggresome ejected and one left behind. (Supplementary Figure 19). The point to underscore is that aggresomes can be removed for remote disassembly and degradation, a novel concept in the field.

6) IFs are not required partners for extruded aggregates. IFs can be co-extruded with polyQ aggregates, but aggregates in the exopher compartment are not always co-localized to IF foci. Since co-extrusion of IF and aggregates occurs in many, but not all, cases, IFDs are not likely to be essential structural components of all aggregate cargos in exophers (Supplementary Figure 18-19).

Novel Insights into aggregate management and collection across species

Our data highlight a potential alternative mechanism for clearing aggresomes in mammals, which might have been missed in cell culture studies, but is highly relevant to the question of how pathological aggregates may spread in neurodegenerative disease. We suggest that aggresomes might serve a staging role for specific types of neuron-threatening contents including disease protein aggregates, with the overall level of proteo-stress influencing the decision for extrusion.

Implications of IF roles in exophergenesis for human biology. Presence of neurofilament light protein (hNFL) in CSF and blood are measured in the clinic as biomarkers for neuronal disease and injury [84-86]. Exactly how hNFL is released into human fluid spaces is not well documented. We found that IFD-1 and IFD-2, sharing 24% identity and 45% similarity with mammalian neuronal intermediate filament NFL, can be expelled within exophers in a significant fraction of exopher events. Interestingly, intermediate filaments were a major reported protein component of extruded material from cardiomyocytes (a suggested mammalian exopher variant [56, 63]), consistent with the idea that mammalian cells can extrude intermediate filament aggresomes via an exopher-related mechanism.

Our findings in *C. elegans* reveal a novel way in which IFs are released from proteo-stressed neurons and raise the possibility that the commonly used biomarker of human neuronal injury and disease might also reflect active neuronal exopher expulsion mechanisms, an option not generally considered.

Exopher-like mechanisms involving IFs might influence a range of disease processes. Heritable mutations in neurofilaments can cause several neurological diseases including Giant Axonal Neuropathy, Charcot-Marie-Tooth (CMT) disease, Amyotrophic Lateral Sclerosis (ALS), and Parkinson's disease (PD) [87, 88]. The molecular mechanisms underlying these diseases remain unclear. Our data introduce the possibility that modulated neuronal trash expulsion under stress conditions might be unexpected contributors to disease pathology.

Neurofilaments have also been widely implicated in a number of neurodegenerative diseases due to their concentrated presence within characteristic pathological inclusions [84, 86]. Pathological neurofilament accumulations are features in Parkinson's disease (with α-synuclein), in Alzheimer's disease (with Aβ and tau), in polyglutamine CAG trinucleotide repeat disorders, and in ALS. For example, the likely relationship between aggresomes and the Lewy body inclusions diagnostic for Parkinson's disease have been often pointed out [89]. We document a novel functional role for IFDs and human NFL in extrusion—we provide the first definitive demonstration that the specific IF proteins that intimately associate with aggresomes and their neurotoxic cargo, actually regulate exopher formation and thus ejection of neurotoxic cargo, and often IFs themselves, from neurons. Research into IFD or NFL management and ejection requirements in *C. elegans* may help explain basic mechanisms promoting aggresome- and -Lewy body like inclusion pathology that results in disease, while also providing the molecular understanding to clinical assays used currently to assess pathology.

Additional information: Supplementary information is available for this paper.

Acknowledgements. We thank past and present members of the Exopher Club for exopher-related discussions, and members of M.D. and B.D.G. laboratories at Rutgers University. We thank H. Ushakov for injections that created some transgenic lines.

Research was supported by the National Institutes of Health under award numbers R37AG56510, R01AG047101, and 1F31AG066405-01A1. K.N. and D.H.H. were supported by NIH OD010943. We thank Yunpeng Xu for sharing detailed control studies on neuronal RNAi efficacy. We thank Florian Geissler/Rudolf E Leube for providing plasmid DNA templates for IFD promoter amplification [36] and Malene Hansen for RNAi allele(s) and RNAi-related discussions. Some strains were provided by the CGC (which is funded by NIH Office of Research Infrastructure Programs (P40 OD010440) and the OK *C. elegans* Deletion Mutant Consortium). Content is solely the responsibility of all authors and does not necessarily represent the official views of the National Institutes of Health.

Author Contributions M.L.A., J.F.C., R.A., S.A., I.M., A.J.S., and R.J.G., conducted and designed experiments, along with M.D., M.L.A., and B.D.G, who wrote the manuscript with input from J.F.C., R.A., and R.J.G.. G.B. provided some plasmid constructions. K.C.N. and D.H.H. carried out electron microscopy fixation, interpretation, and analysis.

Competing interests statement: The authors declare that they have no competing financial interests.

Data Availability: Correspondence and requests for materials should be addressed to Monica Driscoll via email (driscoll@dls.rutgers.edu).

Reprints and permissions information is available at www.nature.com/reprints.

Methods

Strains and media. We cultured *C. elegans* strains at 20°C with standard methods as described [5]. We fed animals *Escherichia coli* OP50 unless we initiated RNAi or a 6-hour fasting protocol to induce proteostress-exophers. Extrachromosomal arrays were harbored on antibiotic selection plates (Hygromycin B or G418). For exopher measurements, L4 animals were removed from selection plates and placed onto standard OP50 plates for later observation.

Strains. New transgenic alleles are provided in figure legends and in the strain list, Table 1. Reporters for FP::IFD were expressed from the touch neuron specific *mec-7* promoter to focus on cell autonomous effects; single copy reporters from the native *ifd-1* and *ifd-2* promotoers did not provide adequate neuronal signal for visualization. P_{mec-7}FP::IFD constructs were effective at complementation of the cognate *ifd* alleles and were neither dominant negative nor exopher-inducing on their own. Animals expressing *igIs*1[P_{mec-7} YFP P_{mec-3}HttQ128::CFP] must be manually selected for CFP expression to avoid silencing of the CFP, which we have not been able to easily reverse (high copy number silencing has been documented [90, 91]). PolyQ constructs are quite challenging to generate due to the extent of repeat sequences therein; still in an attempt to make and study a more co-operative polyQ in touch neurons, we constructed a single copy *bzSi39*[P_{mec-7}mNG::HttQ74] allele. The artificial polyQ protein aggregates minimally. We used CRISPR to generate AID degron-tagged alleles of *hsp-1* and *ftt-2* but found that these alleles were lethal (*hsp-1*) or suppressed exophers (*ftt-2*) even without auxin-i.e., tagging induced the loss of function phenotype which prevented use for inducible tissue specific disruption.

See **Table 1** for strain list.

Plasmid constructions. New allele information is described in **Table 1.** We created single-copy integration using MiniMOS technology and pCFJ1662 hygromycin or pCFJ910 G418-resistance conferring backbones [35]. For extra-chromosomal array transgenesis and selection we used hygromycin or G418 selection by exposing animals to selection plates. To make selection plates, we used 5mg/mL for hygromycin or 32mg/mL for G418 and added 200ul per 6cm OP50-seeded plate.

See **Table 1** for RNAi bacteria clone sequences.

Human homolog optimization and expression. Both IFD-1 and IFD-2 are most closely related to the named mammalian (taxid : 9606) neurofilament light polypeptide (NP_006149.2) with e-values of 2e-15 and 3e-13 for IFD-1 and IFD-2 respectively, sharing 24% identity. To optimize human genes for *C. elegans* expression based on codon and intron bias and *C. elegans* amino acid to tRNA ratio, we used *C. elegans* Codon Adapter GGA Software [61]. Nucleotide coding regions of mammalian proteins are provided. NCBI Reference Sequence: NM_006158.5 for *homo sapiens* neurofilament light. Optimized hNFL sequence avaible in Supplementary Table 1.

CRISPR-CAS9 genomic *ifd-2* deletion. *ifd-2(bz187)* is a deletion of base pairs 816271-815275. The first 3 exons are affected by the genomic deletion which eliminates 996 base pairs, including the *ifd-2* initiation codon. Guide RNA and repair oligo available in Supplementary Table 1.

RNAi. We achieved gene inactivation by feeding animals RNAi bacteria (HTT115) from L4-Ad2 or for 2 generations as noted, using standard methods. We performed RNAi experiments in strains in which neurons are RNAi-enhanced via SID-1 expression [4, 5] required for effective feeding RNAi effects in neurons [53]. We used two transgenes for

neuronal RNAi enhancement, initially working with the $P_{mec\text{-}18}$*sid-1* transgene, which enhances touch neuron RNAi. RNAi studies in our group later established that the pan-neuronal $P_{rgef\text{-}1}$*sid-1* constructs reliably enabled stronger RNAi knockdown of most touch neuron genes we targeted, and thus we focused more on use of the panneuronal knockdown strain. As noted in the strain list, some strains expressed panneuronal *sid-1* in the background of a *sid-1* null mutant, such that only transcripts in neurons or touch neurons could be targeted for degradation. Whenever possible, we confirmed RNAi knockdown effects using alternative approaches.

As a RNAi-target control: We performed RNAi knockdown of *C. elegans* intermediate filament D genes, exposing animals to RNAi clone from L4-Ad2, and assaying ALMR exophers on Ad2 in a screen strain that is mutant for IFDs (ZB5247*: ifd-1(ok2404)*; *ifd-2(bz187)*; *bzIs166*[$P_{mec\text{-}4}$ mCherry]; *uIs71*[(pCFJ90) $P_{myo\text{-}2}$mCherry + $P_{mec\text{-}18}$SID-1]). In this *ifd-1(ok2404)*; *ifd-2(bz187)* double mutant background, RNAi directed against *ifd-1* or *ifd-2* does not change exopher levels compared to the EV control, suggesting that off-target effects associated with disruption in non-neuronal tissues are not potent in this study and that deletion phenotypes are likely to reflect null outcomes predicted from their deletion structures. RNAi knockdowns were 200 ALMR/clone, 4 trials.

Age synchronization. To synchronize animals, we selected L4 stage hermaphrodites and transferred them to test plates. The day after moving was considered adult day 1, Ad1. We scored animals on adult day 2 (Ad2) unless otherwise noted. For scoring exophers, we measured animals on plates using a Kramer pseudo-stereo dissecting scope (20x objective) and immobilized using 100ul of 10mM tetramisole; exophers were also visible in live animals without anesthetic. We scored ALMR neurons for exopher events in a binary (yes/no) manner.

Exopher features for scoring. Exophers are readily visible at 400X total magnification with high power dissecting microscopes. We performed exopher characterization methods as described in detail [5]. We note that baseline exopher levels in the $P_{mec\text{-}4}$mCherry strain is generally in the range of 5-15% ALMR exophers on Ad2. The general or overall (mean) variability of other genetic backgrounds can differ. It is critical to *always* compare control and experiment on the same day because of the baseline variability—a test outcome must be compared to the background of its paired control.

Microscopy. Most high resolution fluorescence micrograph data were captured on Zeiss Axiovert Z1 microscope equipped with X-Light V2 Spinning Disk Confocal Unit (CrestOptics), 7-line LDI Laser Launch (89 North), Photometrics Prime 95B Scientific CMOS camera, using Metamorph 7.7 software. A 100x oil immersion objective, 63x oil immersion, or 40x objective was used.

Fluorescent colocalization analysis. We imaged touch neurons for colocalization experiments. Where needed, we used DIC confirmation to identify touch neurons of interest. For mNG::HttQ74 and HttQ128::CFP colocalization, we used only neurons in which visible mNG-aggregation was observable in the cell (as opposed to dim cytosolic mNG signal) for colocalization calculations. We analyzed thresholded multi-color image

channels using ImageJ FIJI with JACoP analysis software to calculate Pearson's and Mander's overlap coefficients [92].

We used Pearson's coefficient to quantitate colocalization of organelle tags and calculated Mander's overlap of thresholded double-channel images by using the channel relevant to tag IFD over the channel of the other protein tag. We manually analyzed images in each 0.2 - 0.25 um Z-stack for colocalization often observing Z-stacks laterally in 3D projection for 3-dimensional observation.

Soma GFP::IFD-1 focus measurement. We imaged whole touch neurons using 0.1 - 0.2 um Z-stacks. We measured the largest diameter of each inclusion by calculating the longest pixel length using ImageJ software. We omitted neurons with the presence of an exopher(s) from GFP::IFD-1 size calculations. We calculated the number of IFD inclusions using a standard threshold.

Drug assays. For proteostasis drug treatments, we dissolved MG132 (Sigma-Aldrich C2211) and Spautin-1 (Sigma-Aldrich SML0440) in DMSO at 10mM concentration and administered by placing 40µL of each solution over the bacterial food lawn. We exposed animals to drug-plates from L4-Ad2. For DHC-1::degron AID-system treatments, we dissolved auxin in ethanol to 0.4M. We added 25µL 0.4M auxin and 175µl distilled water. We pipeted 200µl solution, per plate, on top of well-seeded OP50 plates. We exposed both control and experimental animals to auxin plates from L4-Ad2 - only the experimental animals harbored *bzSi6*[$P_{mec\text{-}7}$TIR-1::TagBFP] necessary for auxin-inducible degradation [38].

Osmotic stress. We determined sensitivity to acute osmotic stress by moving L4 stage animals to NGM plates containing 450 mM concentrations of NaCl and scored exophers after an overnight exposure. We scored animals for exophers using ringed cytology slides on a fluorescent Kramer dissecting microscope.

Oxidative stress experiments. We determined exopher sensitivity of animals to acute oxidative stress using paraquat (methyl viologen, Sigma). We transferred L4 animals to freshly prepared NGM plates containing paraquat 200 mM and assessed percent survival after an overnight exposure.

Development assay. We measured post-embryonic development (PED) time by transferring eggs to an NGM plate. We performed a 50-gravid animal egg lay lasting one hour upon a new NGM plate. 60 hours after the egg lay, we checked plates every hour and the percentage of progeny to develop was assessed; we removed young adults after counting. We measured the time from hatching to the L4-adult transition qw the time to development. For significance tests we used a standard two-tailed t-test comparing the mean value of three trials.

Fertility. We measured brood size by placing individual L4 stage worms onto NGM plates. We transferred animals to new plates daily for three days, allowing progeny develop to adulthood before paralysis and quantification.

Lifespan. We measured lifespan was measured on NGM plates, transferring animals to fresh plates each day until day 5 of adulthood (Ad5) and after every 4 days thereafter. We assessed viability every 2 days as response to gentle prodding with a platinum pick. Animals that either had internal hatching of progeny or expulsion of internal organs were not counted as deaths.

Mechanosensory touch function. We lightly stroked animals with a fine-hair pick behind the pharynx 5 times and scored a positive response as an animal movement in the reverse direction. For example, if an animal responded 2 out of 5 times, the animals has a 40% response rate.

GST-4::GFP reporter assay. GST-4 is a glutathione S-transferase that facilitates the Phase II detoxification process. *gst-4* expression is regulated by *daf-16* and *skn-1 and* is a common reporter of cytosolic stress. We mounted animals expressing *dvIs19*[(pAF15)$P_{gst\text{-}4}$GFP::NLS] +/- *ifd(Δ)* on microscope slides for 40x imaging and reported maximum intensity per animal in AU.

Electron microscopy. We prepared animals for TEM analysis by high pressure freezing and freeze substitution (HPF/FS), and followed a standard to preserve ultrastructure. After HPF in a Baltec HPM-010, we exposed animals to 1% osmium tetroxide, 0.1% uranyl acetate in acetone with 2% water added, held at −90°C for 4 days before slowly warming back to -60°C, -30°C, and 0°C, over a 2 day period. We rinsed the samples several times in cold acetone and embedded the samples into a plastic resin before curing them at high temperatures for 1–2 days. We collected serial thin sections on plastic-coated slot grids and post-stained them with 2% uranyl acetate and then with 1:10 Reynold's lead citrate, and examined with a JEOL JEM-1400 Plus electron microscope. By observing transverse sections for landmarks such as the 2nd bulb of the pharynx, it was possible to reach the vicinity of the ALM soma before collecting about 1,500 serial thin transverse sections.

We identified 29 ALM somata in serial sections from 23 blocks. We selected 12 candidate cells that were initially identified using light microscopy to contain touch neurons in the bud phase of exophergenesis. We imaged juxtanuclear regions of interest at high-magnification in serial sections, and we took high power electron tomograms (15K or 20K) in those neighborhoods, comparing regions showing either aggresome-like structures, mitochondria, or large lysosomes. We closely examined those regions for evidence of intermediate filaments surrounding and/or lying inside of the organelles. We used IMOD and TrakEM software for 3D analysis of the regions of interest, and for model-making.

Statistical analysis. Each trial is graphed as a percentage of ALMR exopher occurrence (binary); we used Cochran–Mantel–Haenszel analysis for P - value calculation of at least 3 or more biological trials. For IFD measurements, we used two-tailed t-tests. We analyzed the comparison of number of IFD-inclusions by one-way ANOVA (with Dunnets post-test as noted).

Blinding. For exopher measurements, we recorded strain information in a non-visible location. The data were unblinded following completion of the experiment. For blinding microscopy analysis, we mounted and imaged all animals on a slide for a given strain. Post-acquisition, the file names were assigned a random number and re-coded. The images were unblinded following analysis of the entire data set.

Figure legends

Figure 1. Intermediate filaments IFD-1 and IFD-2 act cell autonomously in the exopher pathway.

For most exopher scoring throughout this work we applied the Cochran-Mantel-Haenszel test (CMH), error bars are SEM; * P < 0.05, ** P < 0.005, *** P < 0.0005.

A) **A typical exopher is readily visualized by mCherry.** In strain ZB4065 *bzIs166*[$P_{mec\text{-}4}$mCherry] mCherry is expressed from an integrated high-copy-number transgene array and induces exophergenesis. Ventral touch neuron, AVM (**A**nteroior **V**entral **M**icrotubule touch neuron) and ALMR (**A**nterior **L**ateral **M**icrotubule, **R**ight side) mechanosensory touch neuron and an ALMR-derived exopher are pictured. Scale bar = 2 µm.

B) **Exophers form via a budding out mechanism.** Cartoon depiction of the exophergenesis process. 1) A normal neuronal soma depicted. 2) The neuronal soma swells, cellular contents polarize, and a swelling and budding out process generates a prominent exopher bud. 3) The exopher bud continues to extend outward; the exopher bud matures into a distinct exopher. The exopher can initially remain attached by a thin filament which commonly breaks later.

C) **Deletion of *ifd-1* or *ifd-2* decreases ALMR exophers and the double mutant has exopher levels similar to single mutants**. We scored ALMR exopher production on Ad2 in the *ifd-1(ok2404)* deletion mutant, the *ifd-2(bz187)* deletion mutant, and the double *ifd* deletion mutant *ifd-1(*Δ*);ifd-2(*Δ*)*, all of which harbored the exopher-inducing *bzIs166*[$P_{mec\text{-}4}$mCherry] integrated transgene. The ALMR exopher percentage in the *ifd-1(*Δ*);ifd-2*(Δ*)* double mutant is not significantly different from the single mutant *ifd-1*(P = 0.351); double mutant compared to *ifd-2* P = 0.0952. ALMRs scored > 391/strain, 6 trials.

D) **Single copy P_{mec-7}GFP::IFD-1 rescues the exopher suppression phenotype of the *ifd-1(ok2404)* mutant.** We scored ALMR exophers at Ad2 in *bzIs166*[P_{mec-4}mCherry] compared to *bzIs166*[P_{mec-4}mCherry]; *ifd-1(ok2404)*. P_{mec-4}mCherry is not significantly different compared to *bzIs166*[P_{mec-4}mCherry];*ifd-1(ok2404);bzSi3*[P_{mec-7}GFP::IFD-1] (P = 0.427). N > 552 ALMR/strain, 10 trials.

E) **Single copy P_{mec-7}*mNeonGreen*::IFD-2 rescues the exopher suppression phenotype of the *ifd-2(bz187)* mutant.** We measured Ad2 exophers in ALMR, *bzIs166*[P_{mec-4}mCherry] compared to *bzIs166*[P_{mec-4}mCherry];*ifd-2(bz187). bzIs166*[P_{mec-4}mCherry] is not significantly different from *bzIs166*[P_{mec-4}mCherry];*ifd-2(bz187);bzSi37[*P_{mec-7}mNeonGreen::IFD-2] (P = 0.40). N > 179 ALMR/strain, 5 trials.

Note: *mec*-7 is a heavily utilized and widely confirmed touch neuron promoter in *C. elegans* neurobiology, but we note that caveats regarding its use are that the promoter directs high level expression, and some low level expression in non-touch neurons could occur.

Figure 2. Soma IFD-1 and IFD-2 colocalize to juxtanuclear inclusions that become larger with age and are distinct from other organelles.

For images as indicated, touch cell soma outline is indicated by a continuous line and nucleus is marked by a dotted line, except in A, B where nuclear membrane is clear.

A) **GFP::IFD-1 concentrates in juxtanuclear inclusions.** Shown is a representative Ad2 ALM touch neuron, DIC-GFP merge, strain ZB4723 *bzIs166*[P_{mec-4}mCherry]; *ifd-1*(*ok2404*)X; *bzSi3*[P_{mec-7}GFP::IFD-1], expressing a rescuing, single-copy GFP::IFD-1 transgene. Solid white lines outline the touch neuron soma. Image is representative of N > 40 for this strain. Scale bar = 2 µm.

B) **mNeonGreen::IFD-2 concentrates in juxtanuclear inclusions.** Shown is a representative Ad2 ALM touch neuron, DIC-GFP merge, strain expressing *bzIs166*[P_{mec-4}mCherry];*bzSi37*[P_{mec-7}mNeonGreen::IFD-2]. Solid white lines outline the touch neuron soma. Image is representative of N > 20 with visible expression for this strain. Scale bar = 2 µm.

C) **IFD-1-positive inclusions become larger with age. Top:** L4 larval stage ALM neuron. **Bottom:** Ad11 ALM neuron. Strain expresses *bzIs166*[P_{mec-4}mCherry];

bzSi3[P_{mec-7}GFP::IFD-1]**.** Solid white lines outline the touch neuron soma. Images representative of > 100 observations. Scale bar = 2 µm.

D) IFD-1 and IFD-2 colocalize to juxtanuclear inclusions. Representative of adult touch neuron, strain expressing *bzEx279*[P_{mec-7}GFP::IFD-1 P_{mec-7}RFP::IFD-2]. Image is representative of N > 20. Scale bar = 2 µm. Quantitation of colocalization in panel E.

E) GFP::IFD-1 does not extensively colocalize with a Golgi marker. Representative of adult touch neuron, strain expressing *bzIs166*[P_{mec-4}mCherry]; *bzEx265*[P_{mec-4}TagBFP::AMANS-2];*bzSi3*[P_{mec-7}GFP::IFD-1]. Image is representative of N > 20. Scale bar = 2 µm. Quantitation of colocalization in panel F.

F) GFP::IFD-1 does not extensively colocalize with the LMP-1::mSc lysosome marker. Representative of adult touch neuron, strain expressing *bzIs3*[P_{mec-7}GFP::IFD-1]; *pwSi222*[P_{mec-7}LMP-1::mScarlet]. Representative of N > 20. Scale bar = 2 µm. Quantitation of colocalization in panel G.

G) IFD inclusion does not colocalize with mitoROGFP mitochondria marker. Representative of adult touch neuron, strain expressing *bzEx253*[P_{mec-7}RFP::IFD-2]; *zhsEx17*[P_{mec-4}mitoLS::ROGFP]. Representative of N > 20. Scale bar = 2 µm. Quantitation of colocalization in panel H.

Note: We did note that IFD inclusions were often found next to Golgi or lysosomes, and thus the possibility that the IFD compartments might interact with these organelles, potentially via transient associations, should be entertained in future study.

H) Colocalization correlation of GFP::IFD-1 and RFP::IFD-2 signals (panel D) graphed as Pearson's Coefficient of red and green channel. N = 10, error bars are SEM.

I) Colocalization correlation of GFP::IFD-1 and TagBFP::AMANS-2 signals (panel E) graphed as Pearson's Coefficient of blue and green channel. N = 10, error bars are SEM.

J) Colocalization correlation of GFP::IFD-1 and mSc::LMP-1 signals (panel F) graphed as Pearson's Coefficient of red and green channel. N = 10, error bars are SEM.

K) Colocalization correlation of RFP::IFD-2 and mitoROGFP (panel G) graphed as Pearson's Coefficient of red and green channel. N = 10, error bars are SEM.

Figure 3. Genesis of juxtanuclear IFD inclusions depends on functional microtubules and dynein. Aggregate adapter proteins 14-3-3/FTT-2 and HSP-1 colocalize with IFD-positive organelles.

White dashed line outlines nucleus in panels where indicated.

A) **Example of a mammalian aggregate-adapter complex.** Adapted from Xu 2013 [45], created with BioRender.com. 14-3-3 proteins are able to bind directly to dynein components. 14-3-3 binds BAG3 bound Hsc70/(HSP-1). Hsc70/HSP-1 recognizes and binds ubiquitinylated aggregates. The complex moves along the microtubule tracks to deliver to the aggresome compartment. *C. elegans* counterpart names are indicated.

B) **Microtubule inhibition via colchicine treatment from L4 to Ad2 reduces IFD-1-positive inclusion formation.** Strain expressing *bzIs166*[$P_{mec\text{-}4}$mCherry]; *bzSi3*[$P_{mec\text{-}7}$GFP::IFD-1]**. Left:** Control, DMSO added from L4 to Ad2, Ad2 ALM. **Right:** 5 mM colchicine added from L4 to Ad 2, Ad2 ALM. Scale bar = 2 µm. Image representative of N > 90.

C) **Microtubule inhibition via colchicine increases the number of IFD-1 puncta.** Number of IFD-1-positive puncta per Ad2 ALM. Control DMSO, colchicine 5 mM. L4 to Ad2 exposure. $P < 0.0005$, N > 27/strain, 3 trials, two-tailed t-test, error bars are SEM.

D) **Touch neuron-specific dynein knockdown via auxin inducible degradation of DHC-1::degron reduces IFD-positive puncta formation.** Knockdown strain expresses *bzIs166*[$P_{mec\text{-}4}$mCherry]; *bzSi6*[$P_{mec\text{-}7}$TIR-1::TagBFP]; *bzSi3*[$P_{mec\text{-}7}$GFP::IFD-1]; *dhc-1*(*ie28*[DHC-1::degron::GFP]) and control strain lacks the TIR-1 component (*bzSi6*[$P_{mec\text{-}7}$TIR-1::TagBFP]) and is therefore DHC-1 is not susceptible to degradation. **Left:** Control TIR-1 -/-, Ad2 ALM. **Right:** TIR-1 +/+, Ad2 ALM; 5 mM auxin exposure to the control and the experimental, from L4 to Ad2. Scale bar = 2 µm. Image representative of N > 90.

E) **Touch neuron-specific dynein knockdown increases the number of GFP::IFD-1 puncta:** Number of IFD-1-positive puncta per Ad2 ALM. Auxin

exposure to both the control and the experimental from L4 to Ad2. $P < 0.05$, $N > 25$ / strain, 3 trials, two-tailed t-test, error bars are SEM.

F) **FTT-2::mSc colocalizes with juxtanuclear GFP::IFD-1.** Representative of adult touch neuron expressing *bzSi51*[$P_{mec\text{-}7}$FTT-2::mSc]; *bzIs3*[$P_{mec\text{-}7}$GFP::IFD-1], $N > 10$. Scale bar = 2*µm*. Quantitation of co-localization of N = 10, graphed as Mander's overlap coefficient of GFP channel over mScarlet channel.

G) **mSc::HSP-1 colocalizes with GFP::IFD-1.** HSP-1/Hsc70 is essential for recognizing ubiquitinated aggregates for aggresomal collection in mammalian biology [45, 93]. Representative of adult touch neuron expressing *bzSi53*[$P_{mec\text{-}7}$mSc::HSP-1]; *bzIs3*[$P_{mec\text{-}7}$GFP::IFD-1]. Representative of $N > 10$. Scale bar = 2 *µm*. Quantitation of co-localization of N = 10, graphed as Mander's overlap coefficient of GFP channel over mScarlet channel.

Figure 4. Disease-associated human Htt-polyglutamine expansion protein colocalizes with IFD-1 in touch neurons.

White dashed line outlines the nucleus in all panels.

A) **mNG::UBQ-2 ubiquitin expressed from a single-copy-number transgene colocalizes with mSc::IFD-1.** *ubq-2* includes a canonical ubiquitin fused to the L40 ribosomal large subunit protein; the single ubiquitin polypeptide generated by cleavage can covalently attach to target proteins [94]. We expressed mNG::UBQ-2 from single copy *bzSi38*[$P_{mec\text{-}7}$mNG::UBQ-2], which expresses in touch neurons. mNG::UBQ-2 concentrates to specific subcellular structures including perinuclear IFD-1 and additional foci that are distinct, which would be expected for the range of activities/sites in which ubiquitin is engaged, such as on late endosomes. Adult touch neuron expressing *bzSi38*[$P_{mec\text{-}7}$mNG::UBQ-2]; *bzSi34*[$P_{mec\text{-}7}$mSc::IFD-1] image is representative of $N > 10$. Scale bar = 2 µm. Quantitation of co-localization of N = 10, graphed as Mander's overlap coefficient of mScarlet channel over mNeonGreen channel.

B) **mNG::UBQ-2 ubiquitin colocalizes with mSc::IFD-2.** Representative adult touch neuron expressing *bzEx422*[$P_{mec\text{-}7}$mNG::UBQ-2]; *bzEx421*[$P_{mec\text{-}7}$mSc::IFD-2]. mNG::UBQ-2 concentrates to specific subcellular structures including perinuclear IFD-2 and additional foci that are distinct, which would be expected for the range of activities/sites in which ubiquitin is engaged, such as on late

endosomes. Image is representative of N > 10. Scale bar = 2 µm. Quantitation of co-localization of N = 10, graphed as Mander's overlap coefficient of mScarlet channel over mNeonGreen channel. Although we cannot rule out that high expression drives the mNG::UBQ-2 to the IFD domain, the compartmentalization to specific subcellular localizations is a pattern reported in other ubiquitin studies [95, 96].

C) **HttQ74::mNG expressed from a single-copy-number transgene colocalizes with mSc::IFD-1.** Representative adult touch neuron expressing *bzSi*39[P_{mec-7}HttQ74::mNG]; *bzSi34*[P_{mec-7}mSc::IFD-1]. Images selected were those in which mNG was visibly aggregated in the cell, as opposed to homogenous dim cytosolic signal. Representative of N > 10 with mNG aggregates. Quantitation of colocalization of N = 10, graphed as Mander's overlap coefficient of mScarlet channel over mNeonGreen channel. Scale bar = 2 µm.

D) **HttQ74::mNG expressed from a single-copy-number transgene colocalizes with mSc::IFD-2.** Representative adult touch neuron expressing b*zSi40*[P_{mec-7}mNG::HttQ74]; *bzEx420*[P_{mec-7}mSc::IFD-2] of animals that display visible mNG aggregation. Image is representative of N > 10. Scale bar = 2 µm. Quantitation of co-localization of N = 10 of animals that display visible mNG aggregation, graphed as Mander's overlap coefficient of mScarlet channel over mNeonGreen channel.

E) **HttQ128::CFP expressed from an integrated high-copy-number array colocalizes with mSc::IFD-1.** Representative adult touch neuron expressing *igIs*1[P_{mec-7} YFP P_{mec-3}HttQ128::CFP]; *bzSi34*[P_{mec-7}mSc::IFD-1]. Representative of N > 10 with an overlapping localization. Scale bar = 2 µm. Quantitation of co-localization of N = 10, graphed as Mander's overlap coefficient of mScarlet channel over mNeonGreen channel. See Supplementary Figure 16 for additional localization patterns for HttQ128::CFP and mSc::IFD-1.

Figure 5. IF roles in aggregate collection and neuronal aggregate expulsion may be partially conserved.

A) **mNG::hNFL localizes to the IFD-1 positive aggresome.** Shown is a representative ALM touch neuron. We optimized the coding sequence of human NFL, NM_006158.5, for *C. elegans* expression based on published codon biases

as described in Methods. We added mNeonGreen fluorophore and expressed the construct under the *mec-7* touch neuron promoter. Strain expressing *bzEx269*[P_{mec-7}mNG::hNFL] and *bzSi34*[P_{mec-7}mSc::IFD-1]. Solid white lines outline the touch neuron soma, dotted outline is the nucleus. Image is representative of N > 20. Scale bar = 2 µm. Graphed as Mander's overlap coefficient of mScarlet channel over mNeonGreen channel, N = 10 graphed, error bars are SEM.

B) mSc::hNFL colocalizes with mNG::UBQ-2 ubiquitin. Representative adult touch neuron expressing *bzEx313*[P_{mec-7}mNG::UBQ-2]; *bzSi43*[P_{mec-7}mSc::hNFL]. Image is representative of N > 10. Scale bar = 2 µm. Quantitation of co-localization of N = 10, graphed as Mander's overlap coefficient of mScarlet channel over mNeonGreen channel.

C) mSc::hNFL colocalizes with mNG::HttQ74. Representative adult touch neuron expressing *bzSi39*[P_{mec-7}mNG::HttQ74]; *bzSi43*[P_{mec-7}mSc::hNFL] of animals that display visible mNG aggregation. Image is representative of N > 10. Scale bar = 2 µm. Quantitation of co-localization of N = 10 of animals that display visible mNG aggregation, graphed as Mander's overlap coefficient of mScarlet channel over mNeonGreen channel.

D) hNFL-labeled aggresomes can be extruded from touch neurons in exophers. Representative image (N > 10) of mNG::hNFL extrusion in exophers. Strain expressing *bzEx311*[P_{mec-7}mNG::hNFL] with *bzIs166*[P_{mec-4}mCherry] in the *ifd-2(bz187)* background. Image shows ALMR neuron with three exophers (white arrowheds). Two exophers are positioned in the middle of the image surrounded by scattered mCherry debris, starry night phenotype (SN) from hypodermal exopher digestion [4]. The third exopher pictured, a mature distant exopher, contains a large mNG::hNFL inclusion, shown in focus and zoomed in. The exposure is altered to show details. **Graph on right:** Out of N = 34 Ad2 ALMs with an exopher from strain expressing *bzSi48*[P_{mec-7} mNG::hNFL]; *bzIs166*[P_{mec-4}mCherry], 16 exophers included mNG::hNFL puncta.

E) Touch neuron specific hNFL rescues an *ifd-2* deficit in exophers. Single copy P_{mec-7}mNG::hNFL rescues the exopher suppression phenotype of the *ifd-2(bz187)* mutant. We measured Ad2 exophers in ALMR. *bzIs166*[P_{mec-4}mCherry] compared to *bzIs166*[P_{mec-4}mCherry];*ifd-2(bz187)* and *bzIs166*[P_{mec-4}mCherry];*ifd-2(bz187)* compared to *bzIs166*[P_{mec-4}mCherry];*ifd-2(bz187);bzSi48[*P_{mec-7}mNeonGreen::hNFL], both significantly different, P < 0.005, N = 200 ALMR / strain, 4 trials. . * P < 0.05, ** P < 0.005, *** P < 0.0005.

Supplementary Figure Legends

Supplementary Videos. Demonstration of the distinctive structural differences between membrane layers and intermediate filament types.

$P_{mec\text{-}4}$ mCherry animals were staged as adult day 2 with an exopher bud phenotype.

Video 1: Whorl membrane geometry. Movie 1 shows a focus through series in which individual membranes continue through the full depth of the series without dropping out (unlike members of a filament bundle). Membranes often lie in closely packed layers but may bend sharply to double back on themselves. Scale bar is 50 nm.

Video 2: Intermediate Filaments associated with the circular organelle. Movie 2 shows filaments in a focus-through series demonstrates that (unlike membranes) these filaments do not continue through the full depth of the series, but individually disappear (or appear) at different depths within the series. Some longer filaments run for a distance around the organelle, bending gradually, but these filaments are loosely associated and rarely touch one another. Filaments deeper inside the organelle tend to be short, and run at odd angles to one another, rarely pairing. Scale bar is 50 nm.

Supplementary Figure 1. Ultrastructural analysis reveals the presence of intermediate filament assemblies in distinctive perinuclear structures in proteo-stressed ALM neurons.

We selected $P_{mec\text{-}4}$mCherry animals at adult day 2 with touch neurons that had early exopher buds that had not separated from the neuron of origin (12 ALMs examined in EM). We identified touch neuron somata after extensive transverse thin section series. ALM neuron somata (L/R pair) lay on opposite sides of the midbody, at similar distances from the head and can be unambiguously identified via their characteristic microtubule-filled dendrite features.

A) Lower power TEM view of an ALM neuron in transverse section, embedded in the hypodermis next to the cuticle. A distinctive circular structure (white arrow) lies close to the nucleus (Nuc) and a small mitochondrion (M). Electron lucent contents are dominated by the presence of single filaments. No ribosomes are detectable here, nor other small organelles, which would be expected if the contents derived from typical cytoplasm. Shorter filaments ~ 10 nm in width lie at random angles within the circular organelle, while a single layer of discontinuous filaments of similar width coats the periphery of the organelle. Filament measures are consistent with their identification as intermediate filaments (9.98 nm; > 150

filaments measured). A bundle of microtubules lies just beneath the cuticle layer (cuticle annotated with black arrowheads). Scale bar 500 nm.

B) Higher magnification view of the circular organelle from panel A, showing the filaments in higher resolution (white arrows). Red arrow indicates one of the longer filaments taking position at the outer edge of the organelle. Filaments sometimes adopt a zig-zag pattern of bent filaments as they bundle. Note the thinness of IFs compared to the membrane bilayer surrounding the nearby mitochondrion. Demonstration of how intermediate filaments can be visually distinguished from membrane are included in Supplementary Video 1 and Supplementary Video 2. Scale bar 200 nm.

C) Closeup view of a similar rounded organelle (soma of a different animal) in which most intermediate filaments (red arrows) have assembled into a loose bundle that curves as the bundle envelopes most of the periphery. A small number of shorter filaments lie deeper inside the organelle. Scale bar is 200 nm.

D) Thinner view from an electron tomogram shows curving individual filaments bordering the circular structure, but with a denser, tighter accumulation of filaments (between red arrows), at the edge of the organelle. Note also the bundle of microtubules (blue arrows) lying just outside the indicated organelle. Some very dark ribosomes are now seen within the structure, as well as granular matrix material of moderate electron density that likely represents proteinaceous aggregates. Scale bar is 200 nm.

Discussion. Although successive sequencing is not possible for individual samples, we speculate that the juxtanuclear structures might mature by increasing and expanding the proteinaceous center and adding more intermediate filaments to the periphery.

Ultrastructure of mammalian aggresomes has been reported in cultured HEK cells, with aggresomes described as electron dense cores of (CFTR)-aggregated protein deposits devoid of membrane surroundings, deposited likely intimate to the nuclear membrane, and surrounded by 8 - 10 nm sized filaments that form loosely parallel bundles [8]. Distorted ‘tangles’ of IFs within the dense aggresome core have been noted; organelles can be positioned nearby the aggresome similar to our EM observations (mitochondria in Supplementary Figure 1A) and microscopy observations (Figure 2G).

Overall, we note that limited low resolution EM data exist on aggresome-focused EM [16, 17, 97]. Although the initial description described IF “cages” was based on fluorescent microscopy [8], available EM data suggest at best loose and somewhat disorganized IF networks in aggresome structure, similar to what we report here.

Supplementary Figure 2. RNAi knockdown of intermediate filament genes can decrease exopher production.

Intermediate filament RNAi knockdown in a neuron-specific RNAi strain decreases exopher percentage. We performed RNAi knockdown of each of 9 *C. elegans* intermediate filament genes, exposing animals to RNAi clones for 2 generations, and assaying ALMR exophers on Ad2, screen strain ZB5184 *bzIs166* [P*mec-4*mCherry1] II; *sid-1(qt9)* V; *sqIs71* [P*rgef-1*GFP; P*rgef-1sid-1*;pBS]. Note that in this strain, RNAi should be effective only in all neurons, and not other tissues; expression in touch neurons (as well as all other neurons) is anticipated to be targeted. Our control RNAi studies have found that use of the P_{rgef-1} promoter to express dsRNA transporter SID-1 allows most potent neuronal RNAi targeting, and thus we use P*rgef-1sid-1* for initial RNAi rather than a touch neuron specific promoter strain, in which we find outcomes more variable. Sequence-confirmed RNAi clones were empty vector negative control (EV), *ifa-1*, *ifa-2*, *ifa-3*, *ifb-1*, *ifb-2*, *ifc-1*, *ifc-2*, *ifd-1*, and *ifd-2.* RNAi knockdown N = 250 ALMR/clone, 5 trials. * P < 0.05, ** P < 0.005, *** P < 0.0005.

Supplementary Figure 3 Health, development, lifespan and stress response measures in the *ifd* null mutants.

Strains were ZB4065 *bzIs166*[P_{mec-}4mCherry], ZB4722 *ifd-1(ok2404);bzIs166*[P_{mec-}4mCherry], and ZB4655 *ifd-2(bz187); bzIs166*[P_{mec-}4mCherry].

A) Body length in µM as measured from 10x images taken from dissection microscope. Synchronized Ad2 animals. N > 30, NS, 3 trials, One-way *anova.*

B) Body width as measured from 10x images taken from dissection microscope. Synchronized Ad2 animals. N > 30, NS, 3 trials, One-way *anova.*

C) Brood size. Progeny number per adult. Larval animals were placed onto individual plates. Progeny of these animals were counted during their entire life span and is given as an average number per individual. N = 9, P = NS, 3 trials, One-way *anova.*

D) Development for *ifd-1(ok2404)*. Hours from egg to develop into young adult stage. Isolated embryos (synchronized by an hour egg lay using 50 animals) were placed onto each plate. Individual larvae were monitored every day to identify L4 stage animals. We determined time of development by calculating the average number of days animals needed to reach adulthood. N > 150, P = 0.72, 3 trials. We calculated statistical significance using an unpaired two-tailed t-test where mean values of 3 trials were considered using GraphPad Prism.

E) Development for *ifd-2(bz187)*. We determined hours from egg into young adult stage. We placed isolated embryos (synchronized by an hour egg lay using 50 animals) onto each plate and monitored individual larvae every day for L4 stage markers. We calculated time of development as the average number of days animals needed to reach adulthood. N > 150, P = 0.38, 3 trials. We calculated statistical significance using an unpaired two-tailed t-test in which mean values of 3 trials were compared using GraphPad Prism [98].

F) Survival curve. *ifd-1(ok2404); bzIs166*[P_{mec-}4mCherry].

G) Survival curve. *ifd-2(bz187); bzIs166*[P_{mec-}4mCherry].

Graphed as days until death. We scored newly hatched animals for viability every day using a platinum wire for mechanical stimulation; movement response was scored as alive. We transferred animals at least every two days to prevent mix-up with their hatched progeny. We excluded animals that could not be located on the plate from statistical analysis. N > 150, *ifd-1* P = 0.9442; *ifd-2* P = 0.1152, 3 trials, We performed statistical analysis using the survival function and the Gehan-Breslow-Wilcoxon Test of GraphPad Prism [98].

H) Oxidative stress. Hours on paraquat are graphed vs. survival; strains *ifd-1(ok2404);bzIs166*[P_{mec-}4mCherry] and *ifd-2(bz187); bzIs166*[P_{mec-}4mCherry]. Oxidative stress is associated with proteostasis disruption [13]. For oxidative stress we used 200 mM paraquat in NGM agar. We stored plates overnight at room temperature and subsequently inoculated with concentrated OP50 overnight culture. Following overnight incubation at room temperature plates were ready to use. We started oxidative stress experiments by transferring L4 larvae onto the bacterial lawn. We scored animals hourly for viability using mechanical stimulation with a platinum wire. Plates without paraquat were used as controls. N > 150*, ifd-1* P = 0.0004, *ifd-2* P = 0.076, 3 trials. We performed statistical analysis using the survival function and the Gehan-Breslow-Wilcoxon Test of GraphPad Prism [98].

I) Osmotic stress. Percent survival after 24 hours of exposure to 450 mM NaCl concentrated plates; strains *ifd-1(ok2404);bzIs166*[P_{mec-}4mCherry] and *ifd-2(bz187); bzIs166*[P_{mec-}4mCherry]. Osmotic stress is associated with proteostasis disruption [12]. For osmotic stress we used NGM agar with 450 mM NaCl. We stored plates overnight at room temperature and subsequently inoculated with concentrated OP50 overnight culture; afterovernight incubation at room temperature plates were ready for assay. We started osmotic stress experiments by transferring L4 larvae onto the bacterial lawn followed by an

overnight incubation. Subsequently, we washed in recovery buffer (M9 buffer with 150 mM NaCl) and transferred to normal NGM plates. The viability of each animal was scored after an additional overnight incubation using mechanical stimulation. N > 150, *ifd-1* P = 0.329, *ifd-2* P = 0.76, 3 trials; we used a two-tailed t-test for significance calculation [98].

J) GST-4 expression in *ifd-1(ok2404).* GST-4 is a glutathione S-transferase that facilitates the Phase II detoxification process. GST-4 expression is regulated by *daf-16* and *skn-1* and GST-4::GFP is a common reporter of cytosolic stress. Maximum intensity per animal reported in AU. GST-4::GFP expression is NS (P = 0.16) in *ifd-1* mutants. N > 30, 3 trials. Two-tailed t-test. Strains: *dvIs19*[(pAF15)$P_{gst\text{-}4}$GFP::NLS] and *dvIs19*[(pAF15) $P_{gst\text{-}4}$GFP::NLS]; *ifd-1(ok2404).*

K) GST-4 expression in *ifd-2(bz187).* Maximum intensity per animal reported in AU. GST-4::GFP expression is reduced in *ifd-2* animals (P = 0.0256). N > 30, 3 trials. Two-tailed t-test. Strains: dvIs19[(pAF15)$P_{gst\text{-}4}$GFP::NLS] and dvIs19[(pAF15)$P_{gst\text{-}4}$GFP::NLS]; *ifd-2(bz187).*

Note that increasing proteostress by disruption of proteosome or autophagy generally increases exopher production [4] and Supplementary Figure 11 E – this is the opposite effect of the loss of *ifds,* which suppresses exopher formation, arguing against the *ifd* deletions as generators of systemic stress that influence exophers.

Supplementary Figure 4. Neuronal ALM morphology and mechanosensory touch function remain preserved in *ifd* mutants.

A) ALM morphology of strains *ifd-1(ok2404);bzIs166*[P_{mec}-4mCherry] and *ifd-2(bz187);bzIs166*[P_{mec}-4mCherry]. We scored axonal beading and soma outgrowth percentage on Ad2 (the peak of exophergenesis [4]). Beading and outgrowths are associated with age, stress, and neurodegeneration [99]. NS, One-way *anova*. N > 30, 3 trials.

B) Mechanosensory touch function on Ad1, Ad5, Ad10 for *ifd-1(ok2404);bzIs166*[P_{mec}-4mCherry] and *ifd-2(bz187);bzIs166*[P_{mec}-4mCherry]. We lightly stroked animals with a fine-hair pick behind the pharynx five times and recorded response (direction reversal). For example, if an animal responded 2

out of 5 times, the animals had a 40% response rate. NS, One-way *anova.* Ad1 - 3 trials, N > 90, Ad5 - 1 trial N > 30, Ad10 - 3 trials, N > 90.

C) *ifd-2* mutants display normal number of mCherry collections per ALM. Animals expressing *bzIs166*[P_{mec-4} mCherry] with the *ifd-1* or *ifd-2* mutation have the same number of mCherry aggregates as wildtype – 4.67, 4.56, and 4.31 mean mCherry collections per cell respectively. N = 8.34, 42, 39, 41, one-way *anova* with Dunnett's post-test, 3 trials, P = 0.98 for *ifd-1,* P = 0.79 for *ifd-2.*

D) *ifd-2* mutants display normal size of mCherry collections per ALM. WT mCherry collections per ALM expressing *bzIs166*[P_{mec-4} mCherry] measures a mean punta diameter of 8.34 AU; there is a NS change in the size of mCherry collections per cell in the *ifd-1* mutant (8.57 AU mean diameter) or *ifd-2* mutant (8.57 AU mean diameter). N = 42, 39, 41, one-way *anova* with Dunnett's post-test, 3 trials, P = 0.69 for *ifd-1,* P = 0.15 for *ifd-2.*

E) *ifd-2* mutants display normal number of HttQ74 aggregates per ALM. Animals expressing *bzSi39* mNG::HttQ74 have 1.28 small mNG::HttQ74 puncta per cell (36% WT ALMs imaged display no aggregation at all). In the *ifd-2* mutant, there is a NS change in number of mNG::HttQ74 puncta per cell. N > 35, P = 0.24. 3 trials, standard two-tailed t-test.

F) *ifd-2* mutants display normal size of HttQ74 aggregates per ALM. WT animals expressing *bzSi39* have a maximum puncta diameter of 6.5AU per ALM; there is a NS change in the size of maximum HttQ74 puncta per cell in the *ifd-2* mutant. Represented data censored for ALMs that have no detectable aggregate per cell. N > 22, P = 0.78, 3 trials, standard two-tailed t-test.

G) *ifd-2* mutants have normal levels of mNG::UBQ-2 aggregation in ALM neurons. WT mNG::UBQ-2 localizes to IF-aggresomes as well as other cellular compartments in ALM touch cells. To assess ubiquitin concentration levels we assigned blinded images of ALM neurons a category corresponding to the level of mNG::UBQ-2 concentration observed in the cell. The scale ranged from zero to three, with three being the most concentration, either in terms of the number of concentrated collections or in intensity of concentration. There is no significant difference between the categories of concentration in the *ifd-2* mutant. Strain ZB5582 *bzSi38*[mNG::UBQ-2], ZB5581 *bzSi38*[mNG::UBQ-2]; *ifd-2(bz187).* P = 0.32, standard two-tailed t-test, N = > 45, 3 trials.

H) ***ifd-2* mutants have normal numbers of mNG::UBQ-2 concentrations in ALM neurons.** Using strains ZB5582 *bzSi38*[mNG::UBQ-2] and ZB5581 *bzSi38*[mNG::UBQ-2]; *ifd-2(bz187),* we counted the number of mNG::UBQ-2 foci per ALM in WT and the *ifd-2* mutant. We found no significant change. P = 0.97, standard two-tailed t-test, N > 45, 3 trials.

I) ***ifd-2* mutants have normal levels of mNG::UBQ-2 main concentrations in ALM neurons.** Considering there was an average of 4.4 small foci in the WT mNG::UBQ-2 ALM neurons, which ranged from 0 foci per ALM to 19 foci per ALM, we asked whether the number of main, most concentrated foci per ALM changed, disregarding the smaller less concentrated foci. We found no significant difference between WT and the *ifd-2* mutant. We used strain ZB5582 *bzSi38*[mNG::UBQ-2] and ZB5581 *bzSi38*[mNG::UBQ-2]; *ifd-2(bz187).* P = 0.81, standard two tailed t-test, N > 45, 3 trials.

Supplementary Figure 5. *ifd-1* and *ifd-2* deletions decrease ALMR exophers as reported by a highly expressed cytosolic GFP reporter.

A) We scored ALMR exopher production on Ad2 in the *ifd-1(ok2404)* deletion mutant and the *ifd-2(bz187)* deletion mutant, each of which also harbored *uIs31*[P_{mec-17}GFP] integrated transgene. N > 331, 6 trials. *ifd-1*(P < 0.0005); *ifd-2* (P < 0.0005). Data support that *ifd* disruptions modulate exopher levels independently of the fluorescent reporter used for exopher detection. * P < 0.05, ** P < 0.005, *** P < 0.0005.

B) Representative Ad2 exopher produced from touch neurons in *uIs31*[P_{mec-17}GFP].

Although GFP is not a physiological substrate, we note that exophers have been identified in amphid neurons by dye filling fluorescence labeling that does not involve transgene reporter introduction [4].

Supplementary Figure 6. Touch neuron-specific tagged high-copy number IFD transgenes can rescue the IF exopher deficit.

A) We scored ALMR exophers at Ad2 in *bzIs166*[P_{mec-4}mCherry] compared to *bzIs166*[P_{mec-4}mCherry]; *ifd-1(ok2404), (*P < 0.05). *bzIs166*[P_{mec-4}mCherry]

compared to *bzIs166*[P_{mec-4}mCherry]; *ifd-1(ok2404); bzEx253*[P_{mec-7}GFP::IFD-2 OE] is NS, P = 0.0642. N > 425, 11 trials.

B) We scored ALMR exophers at Ad2 in *bzIs166*[P_{mec-4}mCherry] compared to *bzIs166*[P_{mec-4}mCherry]; *ifd-2(bz187)* (P < 0.05). *bzIs166*[P_{mec-4}mCherry] compared to *bzIs166*[P_{mec-4}mCherry]; *ifd-2(bz187); bzEx253*[P_{mec-7}RFP::IFD-2 OE] is NS. N > 240, 7 trials.

C) We scored ALMR exophers at Ad2 in *bzIs166*[$P_{mecmi-4}$mCherry] compared to *bzIs166*[P_{mec-4}mCherry]; *ifd-1(ok2404); ifd-2(bz187)* (P < 0.054). *bzIs166*[P_{mec-4}mCherry] compared to *bzIs166*[P_{mec-4}mCherry]; *ifd-1(ok2404); ifd-2(bz187); bzEx270*[P_{mec-7}GFP::IFD-1 OE] is NS. N >128, 4 trials.

Supplementary Figure 7. IFD-1-puncta form without *ifd-2*.

A) IFD-1-positive puncta size remains the same in *ifd-2(bz187)*. Diameter, in µm, of Ad2 IFD-1-positive puncta in ALM neurons remains similar to WT in the same in the *ifd-2* background, in a strain expressing *bzIs166*[P_{mec-4} mCherry]; *bzSi3*[P_{mec-7} GFP::IFD-1]. P = NS, N > 55, 3 trials, two-tailed t-test, error bars are SEM.

B) IFD-1-positive puncta form juxtanuclearly with or without *ifd-2(bz187).* Percentage of juxtanuclear IFD-1-positve puncta per ALM does not significantly differ in strains expressing *bzIs166*[P_{mec-4} mCherry]; *bzSi3*[P_{mec-7} GFP::IFD-1], with or without *ifd-2(bz187)*. P = NS, N > 37, 3 trials, two-tailed t-test, error bars are SEM. Juxtanuclear location assessed in a binary manner.

C) IFD-1-positive puncta number per ALM neuron remains the same in control and *ifd-2(bz187).* Number of IFD-1-positive inclusions in Ad2 ALM somas does not change in mutant *ifd-2(bz187)* versus WT in strains expressing *bzIs166*[P_{mec-4} mCherry]; *bzSi3*[P_{mec-7} GFP::IFD-1]. NS, N > 39, 3 trials, two-tailed t-test, error bars are SEM.

Supplementary Figure 8. Expression of GFP-tagged *ifd-1* and *ifd-2* from their native promoters are detectable in *C. elegans* intestine.

A) High copy number *bzEx419*[P_{ifd-1}GFP::IFD-1], crossed with touch neuron marker, *bzIs166*[P_{mec-4} mCherry], is not readily visible in ALM touch neurons. Merge of

GFP, mCherry, and DIC channel - same image view as in left, but different stack of the animal. mCherry-tagged neuron is out of the focal plane. Images are representative of N > 10. Scale bar = 2 µm.

B) High copy number *bzEx418*[P_{ifd-2}GFP::IFD-2] crossed with touch neuron marker, *bzIs166*[P_{mec-4} mCherry], is not readily visible in ALM touch neurons. Merge of GFP, mCherry, and DIC channel - same image view as in left, but different stack of the animal. mCherry-tagged neuron is out of the focal plane. Images are representative of N > 10. Scale bar = 2 µm.

In-line endogenous tag of IFDs show visible expression in *C. elegans* gut.

C) N-terminal GFP tag of the endogenous *ifd-1* gene (*Syb5616*) crossed with touch neuron marker, *bzIs166*[P_{mec-4}mCherry]. Merge of GFP, mCherry, and DIC channel – same animal, different z-stack. mCherry-tagged neuron is out of the gut focal plane. GFP is not detectable in ALM touch neurons. Images are representative of N > 10. Scale bar = 2 µm.

D) N-terminal GFP tag of the endogenous *ifd-1* gene *ifd-1(bz477)* crossed with touch neuron marker, *bzIs166*[P_{mec-4}mCherry]. Merge of GFP, mCherry, and DIC channel – same animal, different z-stack. mCherry-tagged neuron is out of the focal plane of the gut. GFP is not visible in ALM touch neurons. Images are representative of N > 10. Scale bar = 2 µm.

Although endogenously tagged constructions are optimal for physiological evaluation of reporters, often visualization of single copy tags is commonly difficult in touch neurons, which is the case for native *ifd-1* and *ifd-2*. For this reason we relied on single copy transgenes expressed in touch neurons from the strong *mec-7* promoter, which does confer genetic rescue of *ifd* deletion deficits without conferring detectable dominant negative or over-expression phenotypes.

Supplementary Figure 9. Single copy transgene of P_{ifd-2} GFP::IFD-2 expressed from the native promoter rescues the *ifd-2* exopher deficit.

A) We expressed GFP::IFD-2 from the native *ifd-2* promoter; mCherry background and scored for exopher levels. We compared ALMR exophers at Ad2 in *bzIs166*[P_{mec-4}mCherry] compared to *bzIs166*[P_{mec-4}mCherry]; *ifd-2(bz187) (P = 0.017). bzIs166*[P_{mec-4}mCherry] compared to *bzIs166*[P_{mec-4}mCherry]; *ifd-2(bz187); bzSi76*[P_{ifd-2}GFP::IFD-2] (P = NS). N > 229, 5 trials. Cochran-Mantel-Haenszel test, error bars are SEM.

B) Single copy GFP::IFD-2 tag expressed from the native *ifd-2* promoter does not change exopher levels. We expressed GFP::IFD-2 from the native *ifd-2* promoter; mCherry background, and scored for exopher levels. We compared ALMR exophers at Ad2 in *bzIs166*[P_{mec-4}mCherry] to *bzSi76*[P_{ifd-2}GFP::IFD-2] and found no significant difference, although in two trials, *bzSi76*[P_{ifd-2}GFP::IFD-2] displayed exopher levels higher than 15%, P = 0.15, 6 trials, N > 300.

Supplementary Figure 10. Intestine-specific *ifd-2* expression is not effective for rescue of *ifd-2(Δ)* defects in exopher production. *ifd-2* is expressed in intestine and can influence intestinal morphology [98], raising the question as to whether the intestine might signal non-autonomously to impact exopher production. We therefore expressed *ifd-2* from the *vha-6* intestine-specific promoter in the *ifd-2(D)*; mCherry background and scored exopher levels. We compared ALMR exophers at Ad2 in *bzIs166*[P_{mec-4}mCherry] compared to *bzIs166*[P_{mec-4}mCherry]; *ifd-2(bz187)* (P=0.0053); *bzIs166*[P_{mec-4}mCherry] compared to *bzIs166*[P_{mec-4}mCherry]; *ifd-2(bz187); bzSi45*[P_{vha-6}mSc::IFD-2] (P = 0.29). *bzIs166*[P_{mec-4}mCherry]; *ifd-2(bz187)* compared to *bzIs166*[P_{mec-4}mCherry]; *ifd-2(bz187); bzSi45*[P_{vha-6}mSc::IFD-2] is P = 0.07, N > 130, 5 trials. Cochran-Mantel-Haenszel test, error bars are SEM.

Supplementary Figure 11. IFD-1 compartments are enlarged under neuronal stress conditions

Our previous work showed that exopher levels are high in early adult life (Ad1-Ad3) and then reach a low baseline for much of adult life that follows. Disruption of autophagy genes *bec-1, atg-7, lgg-1/-2* or exposure to autophagy inhibitor Spautin and/or proteasome inhibitor MG132 elevates exophers, consistent with the idea that exophers are generated under enhanced neuronal proteostress [4], unpublished observations on MG132 single agent.

A) **Number of IFD-1 inclusions per ALM neuron with increasing age.** Strain: ZB4632 *bzIs166*[P_{mec-4}mCherry]; *bzSi3*[P_{mec-7}GFP::IFD-1]. Life-stage points assayed: L4, Ad1, Ad2, Ad3, Ad4, Ad6, Ad10, Ad11, Ad12, Ad14. N = 25, 19, 34, 28, 30, 25, 9, 13, 12 for lifestages respectively. One-way *anova*, Dunnett's post-test, error bars are SEM. Note that the period of highest IFD-1 inclusion load coincides with that of the early adult peak in exophergenesis we previously reported [4].

B) IFD-1-positive inclusions increase in size with age. GFP::IFD-1 diameter in ALM neurons in µm. Strain: ZB4632 *bzIs166*[P_{mec-4}mCherry];*bzSi3*[P_{mec-7}GFP::IFD-1]**.** Life-stage points assayed: L4, Ad1, Ad2, Ad3, Ad4, Ad6, Ad10, Ad11, Ad12, Ad14. N = 25, 19, 34, 28, 30, 25, 9, 13, 12 for life stages, respectively. Error bars are SEM. Note that exopher levels are high during early adult life but then return to baseline for much of adult life; we observe a second peak in exopher production later in life that is much more variable in occurrence and specific time of onset [4]. Note that the size of the IF foci does not always correlate with extrusion level, especially later in life.

C) IFD-1-positive inclusions increase in average size under enhanced proteostress induced by mCherry expression. GFP::IFD-1 diameter in ALM neurons in µm on Ad2. Strain ZB4998 *bzSi3*[P_{mec-7}GFP::IFD-1], ZB4632 *bzIs166*[P_{mec-4}mCherry]; *bzSi3*[P_{mec-7}GFP::IFD-1]**,** P > 0.005, N > 50/strain, 3 trials, two-tailed t-test, error bars are SEM. *bzIs166*[P_{mec-4}mCherry] produces a high level of mCherry in touch neurons and elevates exopher production and thus we consider *bzIs166*[P_{mec-4}mCherry] to induce proteostress. EM data support major cell biological changes in *bzIs166*[P_{mec-4}mCherry] touch neurons, some reflective of protein aggregation [4].

D) IFD-1-positive inclusions increase in size under enhanced proteostress induced by proteasome and autophagy inhibitors. We treated strain ZB4632 *bzIs166*[P_{mec-4}mCherry]; *bzSi3*[P_{mec-7}GFP::IFD-1] with both 10 mM proteasome inhibitor MG132 and 10 mM autophagy inhibitor Spautin-1, proteostresses that are known to enhance exopher production, from L4 to Ad3 and measured GFP::IFD-1 inclusion size at Ad3. GFP::IFD-1 diameter in ALM neurons in µm. P < 0.05, N > 50/strain, 3 trials, two-tailed t-test, error bars are SEM. P < 0.05, *. P < 0.005, **. P < 0.0005, ***.

E) *epg-9*/ATG101 mutant significantly increases the percentage of ALMR exopher production on Ad2. EPG-9 works with the UNC-51 complex to regulate induction of autophagy and is essential for autophagy function [100]. Strain: ZB4993 *epg-9(bp320)III*; *bzIs166*[P_{mec-4}mCherry]; *bzSi3*[P_{mec-7}GFP::IFD-1], ZB4632 *bzIs166*[P_{mec-4}mCherry]; *bzSi3*[P_{mec-7}GFP::IFD-1]. P < 0.0005, N > 83 / strain, 3 trials, error bars are SEM. Cochran-Mantel-Haenszel test, error bars are SEM.

F) IFD-1-positive puncta number per cell increases in the *epg-9*/ATG101 mutant. Strain: ZB4993 *epg-9(bp320)*III; *bzIs166*[P_{mec-4}mCherry]; *bzSi3*[P_{mec-7}GFP::IFD-1], ZB4632 *bzIs166*[P_{mec-4}mCherry]; *bzSi3*[P_{mec-7}GFP::IFD-1]. P = 0.07, N > 30/strain, 3 trials, two-tailed t-test, error bars are SEM.

G) Maximum IFD-1-positive puncta size increases in *epg-9*/ATG101 mutant. Strain: ZB4993 *epg-9(bp320)III*; *bzIs166*[P_{mec-4}mCherry]; *bzSi3*[P_{mec-7}GFP::IFD-1], ZB4632 *bzIs166*[P_{mec-4}mCherry]; *bzSi3*[P_{mec-7}GFP::IFD-1]. Maximum GFP::IFD-1 punctae diameter per ALM, in µm. $P < 0.005$, $N > 30$/strain, 3 trials, two-tailed t-test, error bars are SEM.

Supplementary Figure 12. Multiple IFD-1 and IFD-2 fluorescently-tagged reporter proteins (tags GFP, RFP, mScarlet, mNeonGreen) exhibit similar localization to juxtanuclear foci.

Adult ALM soma outlined with continuous line, nucleus outlined with dotted-line. Scale bar = 2 µm. Images representative of $N > 10$.

A) ZB5021 *bzSi34*[P_{mec-7}mSc::IFD-1]
B) ZB4998 *bzSi3*[P_{mec-7}GFP::IFD-1]
C) ZB5091 *bzSi37*[P_{mec-7}mNG::IFD-2]; *bzIs166*[P_{mec-4}mCherry]
D) ZB4866 *bzEx253*[P_{mec-7}RFP::IFD-2]; *zdIs5*[P_{mec-4}GFP]. Free touch neuron GFP diffuses throughout the cytoplasm.

Supplementary Figure 13. Transgenic IF tags are neither dominant negative for exopher production nor exopher-elevating on their own.

A) Single copy *bzIs3*[P_{mec-7}GFP::IFD-1] does not affect Ad2 ALMR exopher levels. $P = 0.92$, $N > 571$/strain, 10 trials, Cochran-Mantel-Haenszel test, error bars are SEM. Strains: control ZB4065 *bzIs166*[P_{mec-4}mCherry] and ZB4632 *bzIs166*[P_{mec-4}mCherry];*bzSi3*[P_{mec-7}GFP::IFD-1].

B) Single copy *bzIs37*[P_{mec-7}mNG::IFD-2] does not affect Ad2 ALMR exopher percentage. $P = 0.75$, $N > 100$, 3 trials, Cochran-Mantel-Haenszel test, error bars are SEM. Strains: control ZB4065 *bzIs166*[P_{mec-4}mCherry] and ZB5091 *bzIs166*[P_{mec-4}mCherry];*bzSi37*[P_{mec-7}mNeonGreen::IFD-2].

C) Over-expressed (OE) GFP::IFD-1 array does not affect Ad2 ALMR exopher percentage. $P = 0.0904$, $N > 208$, 7 trials, Cochran-Mantel-Haenszel test, error bars are SEM. Strains: control ZB4065 *bzIs166*[P_{mec-4}mCherry] and ZB4501 *bzIs166*[P_{mec-4}mCherry];*bzEx270*[P_{mec-7}GFP::IFD-1].

D) Over-expressed (OE) RFP::IFD-2 array does not affect Ad2 ALMR exopher percentage. P = 0.987, N > 425, 11 trials, Cochran-Mantel-Haenszel test, error bars are SEM. Strains: control ZB4065 *bzIs166*[P_{mec-4}mCherry] and ZB4792 *bzIs166*[P_{mec-4}mCherry];*bzEx253*[P_{mec-7}RFP::IFD-2].

Supplementary Figure 14. The size of the GFP::IFD-1 concentration does not correlate with exopher rate.

A) GFP::IFD-1-aggresomes can be cleared from the soma, but size of aggresomes that frequently remain in the soma does not correlate with an exopher event. We imaged 95 Ad3 ALMs from a strain ZB4632 *bzIs166*[P_{mec-4}mCherry];*bzSi3*[P_{mec-7}GFP::IFD-1]. 51/95 (54%) displayed an exopher event while 44/95 (46%) did not. We categorized the neurons into two groups: one group that did make an exopher ('exopher-population') and a group that did not display an exopher event at time of collection ('no-exopher population'). We measured the diameter (in AU) of the aggresome in the soma in both groups.

We found that the 'exopher+ population' included several cases in which there was no remaining GFP::IFD-1 aggresome in the soma (7/44, or ~16%) (consistent with the idea that the neuron ejects GFP::IFD-1 aggresomes discussed in Supplementary Figure 19, showing ~18% GFP::IFD-1-aggresome ejection rate). There was one case in which there was no detectable GFP::IFD-1 aggresome in the 'no-exopher' population.

Not considering cases in which there was not a GFP::IFD-1 aggresome to measure, we measured no significance in the size of the soma aggresome between the population of animals that made an exopher versus the population that did not make an exopher. P = 0.219 excluding datapoints with 0 aggresome, two-tailed t-test.

B) Early (L4) aggresome size does not predict Ad1-3 exophergenesis. To ask if early aggresome size could indicate likelihood of later exophergenesis on adult day 2 or 3, we looked at L4 aggresome size and number per cell, and later scored for exopher production. We imaged 216 L4 neurons and successfully recovered 154/216 animals post-imaging. After 2-3 days on NGM-plates, we scored for exophers (Ad2 and Ad3). Out of 154 animals, 24 had an ALM exopher evident on Ad2/Ad3.

To analyze, we binned the animals into two populations: one population that did not make an exopher ('no-exopher') and a population that that did make an exopher ('exopher'). We found no difference in early (L4) aggresome number per cell between the two populations. P = 0.67, two-tailed t-test, N successfully imaged on Ad2 = 50, 31, 18, 24, 26 in 5 biologic trials respectively.

C) Continuing analysis from B, we measured GFP::IFD-1 diameter (AU) in the L4 ALMs in both populations and found NS, P = 0.47 two-tailed t-test.

Supplementary Figure 15. IFD puncta measures under conditions of microtubules or dynein-mediated transport disruption.

A) Microtubule inhibition via colchicine treatment from L4 to Ad2 reduces ALM IFD-1 puncta size. Strain is ZB4632 *bzIs166*[P_{mec-4}mCherry]; *bzSi3*[P_{mec-7}GFP::IFD-1]; diameter of IFD-1-positive organelle in ALM Ad2 in µm. Control DMSO, colchicine 5 mM L4 to Ad2 exposure. P < 0.0005, N > 99/strain, 3 trials, two-tailed t-test, error bars are SEM.

B) Microtubule inhibition via colchicine treatment from L4 to Ad2 reduces the juxtanuclear location IFD-1 puncta. Strain is ZB4632 *bzIs166*[P_{mec-4}mCherry]; *bzSi3*[P_{mec-7}GFP::IFD-1]; control DMSO, colchicine 5 mM L4 to Ad2 exposure. P < 0.0005, N > 99 / strain, 3 trials, two-tailed t-test, error bars are SEM.

C) Cell-specific DHC-1 dynein knockdown via AID reduces ALM Ad2 IFD-1 puncta size. Strains are ZB4871 *bzIs166*[P_{mec-4}mCherry]; *bzSi6*[P_{mec-7}TIR-1::TagBFP]; *bzSi3*[P_{mec-7}GFP::IFD-1]; *dhc-1*(*ie28*[DHC-1::degron::GFP]) and ZB4872 *bzIs166*[P_{mec-4}mCherry]; *bzSi3*[P_{mec-7}GFP::IFD-1]; *dhc-1*(*ie28*[DHC-1::degron::GFP]). Diameter of IFD-1-positive organelle in ALM Ad2 is measured in µm. Control is -/- for P_{mec-7}TIR-1, *dhc-1* knockdown strain is +/+ for P_{mec-7}TIR-1. Both strains were exposed to 5 mM auxin from L4 to Ad2. P < 0.005, N > 86 / strain, 3 trials, two-tailed t-test, error bars are SEM.

D) Cell-specific DHC-1 dynein knockdown via AID reduces the juxtanuclear location of Ad2 ALM IFD-1 puncta. Strains are ZB4871 *bzIs166*[P_{mec-4}mCherry]; *bzSi6*[P_{mec-7}TIR-1::TagBFP]; *bzSi3*[P_{mec-7}GFP::IFD-1]; *dhc-1*(*ie28*[DHC-1::degron::GFP]) and ZB4872 *bzIs166*[P_{mec-4}mCherry]; *bzSi3*[P_{mec-7}GFP::IFD-1]; *dhc-1*(*ie28*[DHC-1::degron::GFP]). Control strains is -/- for P_{mec-7}TIR-1, *dhc-1* knockdown strain is +/+ for P_{mec-7}TIR-1. Both strains were exposed

to 5 mM auxin from L4 to Ad2. $P < 0.005$, $N > 30$ / strain, 3 trials, two-tailed t-test, error bars are SEM.

Supplementary Figure 16: Highly expressed HttQ128::CFP and mScarlet::IFD-1 reveal variable colocalization.

A) **Localization patterns of HttQ128::CFP and IFD-1 interaction.** In this strain, HttQ128::CFP is expressed from a high-copy-number integrated transgene array. Expression is higher than in the single-copyHttQ74 strain, and the polyQ tract is longer. In this background, we note that the IFD compartment often does not appear to fully surround the HttQ128 signal. Biophysical analyses support heterogeneity in aggregate properties *in vivo* in polyQ touch neurons [76]. Top row: Adult touch neuron soma displaying the three main patterns of interaction we note in lines that express mScarlet::IFD-1 and HttQ128::CFP. 1) HttQ128::CFP signal fully encompass IFD signal, with globular expansion from the IFD core. 2) HttQ128 and IFD display a bi-lobed globular interaction, where part of the bi-lobed structure has overlap. 3) HttQ128 and IFD overlap entirely (white arrows). Scale bar = 2 µm. Bottom row: side view z-stack (0.2 µm) for images in the top row. Scale bar = 2 µm. Strain: ZB5104 *igIs1*[P_{mec-7} YFP, P_{mec-3} htt57Q128::CFP, *lin-15(+)*]; *bzSi34*[P_{mec-7} mScarlet::IFD-1].

B) **HttQ128::CFP and mSc::IFD-1 compaction over time.** Figure represents a 5-day time-course of an ALM neuron expressing HttQ128::CFP and mSc::IFD-1. Neurons were imaged as an adult (A), rescued from microscope slides and placed back on plates. Three days later the same neuron was imaged (B). Two more days later (+5 days) the neuron was imaged again. Strain ZB5104 *igIs1*[P_{mec-7} YFP, P_{mec-3} Htt57Q128::CFP, lin-15(+)]; *bzSi34* [P_{mec-7} mScarlet::IFD-1]. Out of nine multi-day observations of when mSc and CFP are interacting, we find about half the time (4/9 observations), HttQ128 can globularly expand at the mSc::IFD-1-aggresome site. C and D show quantification of intensity of each fluorophore respectively across at least 2 time-points (taken 2 or more days apart).

C) **Quantification of HttQ128 collection at the aggresome site over time.** We imaged (nine) touch neurons that co-expressed interacting HttQ128::CFP and mSc::IFD-1 (time 1), then rescued the animals from microscope slides and placed animals back on plates for at least 2 days. We then imaged the same neurons again, at least 2 days later (time 2). When looking at the same

aggresome site over a period of at least 2 days, we conclude that HttQ128::CFP displays a dynamic collection pattern. HttQ128 can either globularly expand at the aggresome site (as measured by intensity, AU) in 4/9 neurons (and as depicted in Panel B), or decrease in intensity at the aggresome site, observed in 5/9 neurons.

D) **Quantification of mSc::IFD-1 collection at the HttQ128-filled aggresome.** In the same experimental set as in C, when looking at the same aggresome site over a period of at least two days, interestingly, we found that mSc::IFD-1 typically displays a reduction in collection over time, as measured by maximum intensity (AU) at the aggresome site. (8/9 neurons displayed reduced intensity at the aggresome site).

Interestingly, aggresome behavior in the absence of aggresome-targeted protein HttQ128 is different from when only GFP::IFD-1 is present over time (see Supplementary Figure 11B which shows GFP::IFD-1 aggresome growth over time in absence of aggresome-targetting-protein, HttQ128). Results suggest alternative behavior of the IF-aggresome upon introduction of an elevated aggresome-targetted-aggregate like HttQ128.

Supplementary Figure 17. Over-expressed mCherry is predominantly housed in LMP-1-bound lysosomal-organelles, which are distinct from the IF-compartment.

A) **IFD-positive organelles are often localized next to, but not overlapping with, a subset of mCherry concentrations when tagged IFD is expressed from a single copy transgene**. Representative Ad2 touch neuron, representative of N > 50. Strain ZB4632 *bzIs166[*P_{mec-4}mCherry]*; bzSi3*[P_{mec-7}GFP::IFD-1]. Scale bar = 2 µm

B) **mCherry is mostly in LMP-1-bound structures.** A representative adult ALM neuron (white solid outline) expressing the LMP-1::GFP lysosome marker. Representative of N > 250. LMP-1::GFP signal is enriched in the lysosome membrane forming a GFP ring (pseudo-colored blue) around the mCherry collection. mCherry degradation appears minimal within the LMP-1::GFP compartment as signal persists. GFP channel is pseudo-colored to blue to emphasize reporter difference in panel A. Strain ZB4509 *bzIs166[*P_{mec-4}mCherry]*; bzIs168*[P_{mec-7}LMP-1::GFP]. White dashed line outlines the nucleus. Scale bar = 2 µm.

Supplementary Figure 18. IFD + HttQ74 can be joint exopher cargo. HttQ74 aggregates frequently exit the cell, with concentrated HttQ74 foci colocalized with the IFD+ structure ~ 50% of the time.

A) **IFD-1-positive puncta extruded in an HttQ74-enriched exopher.** Shown is an adult touch neuron from strain ZB5171 *bzSi39*[P_{mec7} HttQ74::mNG]; *bzSi34*[P_{mec-7}mScarlet::IFD-1] on Ad1 after a 6 hour fast. Soma outline white, nucleus white dash; arrowhead points to the concentrated HttQ74 punctum that co-localizes to the IFD-1 domain or HttQ74::mNG-mSc::IFD-1 puncta. Scale bar = 2 µm, N > 10. Note that in this image much of the cytosolic mNG::HttQ74 gets extruded into the exopher, but there is notable concentration in the mSc::IFD-1-compartment.

B) **Top: IFD-1-positive organelles are included in 14/30 ALM exopher events.** We examined strain ZB5171 *bzSi39*[P_{mec7}HttQ74::mNG]; *bzSi34*[P_{mec-7}mScarlet::IFD-1] on Ad1, after a 6 hour fast to increase exopher yields, and determined how often mScarlet::IFD-1 was extruded in exophers. We observed 30 ALM exopher events, with 14 having mSc::IFD-1 included in the exopher. **Bottom: Exophers that contain an IFD aggresome frequently colocalize with mNG::HttQ74 aggregates.** We determined how often the 14 mScarlet::IFD-1-positive exopher events also included at least one event of concentrated HttQ74 puncta overlapping with mSc::IFD-1. In 11 ALM IFD-1-positive exophers there was at least one mNG::HttQ74 punctum colocalized with mSc::IFD-1.

C) **Top: HttQ74-aggregates are included in 22/30 ALM exopher events.** We examined the same strain and the same exopher events as in A. ZB5171 *bzSi39*[P_{mec7}HttQ74::mNG]; *bzSi34*[P_{mec-7}mScarlet::IFD-1] on Ad1, after a 6 hour fast to increase exopher yields. We determined how often HttQ74 aggregates were extruded in exophers. Out of N = 30 ALM exopher events, 22 exopher events had at least one HttQ74 aggregate included in the exopher. **Bottom: Ejected HttQ74 aggregates can colocalize with IFD.** We determined how often mNG::HttQ74 positive exopher events (N = 22) included species where HttQ74 is a cargo of the mSc-aggresome. 50% of ALM HttQ74-positive exophers had at least one incidence of HttQ74 including mSc::IFD-1.

Supplementary Figure 19. IFD-positive puncta can be extruded in exophers labeled with mCherry.

A) **IFD-1-positive puncta extruded in an exopher** tagged with *bzIs166*[P_{mec-4}mCherry] for touch-neuron-exopher visualization. Shown is an adult touch neuron from strain ZB4632 *bzIs166*[P*mec-4*mCherry];*bzSi3*[P*mec-7*GFP::IFD-1]. Soma outline in white, nucleus white-dash. Arrowhead points to the concentrated GFP::IFD-1 organelle, one concentration remains in the soma, and one concentration is ejected in the exopher. Scale bar = 2 um, representative of N > 10.

B) **IFD positive organelles are included in ALM exophers.** We examined strain ZB4632 *bzIs166*[P_{mec-4}mCherry]; *bzSi3*[P_{mec-7}GFP::IFD-1] on Ad3 and determined how often GFP::IFD-1 was extruded in exophers. In total, we observed 61 ALM Ad3 exopher events, with eleven having GFP::IFD-1 included in the exopher, 3x trials.

C) **The cell can eject the entire GFP::IFD-1-positive aggresome.** To ask if the neuron ejected the largest GFP::IFD-1 collection of the cell, we looked at the neurons that ejected a GFP:IFD-1 from panel B. Of the nine neurons in which GFP::IFD-1 was expelled in the exopher, four neurons ejected the only – and entire - GFP::IFD-1 organelle present.

Excluding datapoints in which there were no foci that remained in the soma, the size of the GFP::IFD-1 that remained in the soma versus the size of the foci that were expelled is NS. Data suggest that a cell can get rid of the entire IFD-organelle-compartment but that there is no obvious size difference in the ejected aggresomes versus the aggresome that remains in the soma. Strain ZB4632 *bzIs166*[P_{mec-4}mCherry]; *bzSi3*[P_{mec-7}GFP::IFD-1].

Supplementary Figure 20. Assessing *hda-6* and *sqst-1* impact on IFD compartments and exopher production

A) ***hda-6(ok3203)* does not significantly affect IFD-1 puncta number per cell in the *bzIs166*[P_{mec-4}mCherry] background.** Strain is ZB4801 *bzIs166*[P_{mec-4}mCherry]; *hda-6(ok3203); bzSi3*[P_{mec-7}GFP::IFD-1], ZB4632 *bzIs166*[P_{mec-4}mCherry]; *bzSi3*[P_{mec-7}GFP::IFD-1]. HDA-6 is an ortholog of human HDAC6, a cytoplasmic deacetylase with conserved function as an adapter, microtubule modulator, and autophagy regulator. Number of IFD-1 puncta in ALM Ad2, N > 60, 4 trials, two-tailed t-test, NS, error bars are SEM.

B) *hda-6(ok3203)* does not affect IFD-1 puncta size in *bzIs166*[P$_{mec-4}$mCherry] background. Strains are ZB4801 *bzIs166*[P$_{mec-4}$mCherry]; *hda-6(ok3203), bzSi3*[P$_{mec-7}$GFP::IFD-1], ZB4632 *bzIs166*[P$_{mec-4}$mCherry]; *bzSi3*[P$_{mec-7}$GFP::IFD-1]. Diameter of IFD-1 puncta measured in ALM Ad2 in µm. N > 60, 4 trials, two-tailed t-test, error bars are SEM.

C) *hda-6(ok3203)* increases exophergenesis in the *bzIs166*[P$_{mec-4}$mCherry] background on Ad2. Strains are ZB4801 *bzIs166*[P$_{mec-4}$mCherry]; *hda-6(ok3203), bzSi3*[P$_{mec-7}$GFP::IFD-1], ZB4632 *bzIs166*[P$_{mec-4}$mCherry]; *bzSi3*[P$_{mec-7}$GFP::IFD-1]. P > 0.0005, N > 150, 8 trials. Cochran-Mantel-Haenszel test, error bars are SEM.

D) IFD-1 puncta size decreases in *sqst-1*(*ok2892*). *sqst-1* encodes the ortholog of human SQSM1, an aggregate adapter protein implicated in mammalian aggresome formation and autophagy. Strains are ZB4632 *bzIs166*[P$_{mec-4}$mCherry]; *bzSi3*[P$_{mec-7}$GFP::IFD-1], ZB4838 *bzIs166*[P$_{mec-4}$mCherry]; *sqst-1ok2892*) IV; *bzSi3*[P$_{mec-7}$GFP::IFD-1]. Diameter of IFD-1 puncta in ALM Ad2 in µm. P < 0.05, N > 25, 3 trials, two-tailed t-test, error bars are SEM.

E) IFD-1 puncta number per ALM increases in *sqst-1*(*ok2892*). Strains are ZB4632 *bzIs166*[P$_{mec-4}$mCherry];*bzSi3*[P$_{mec-7}$GFP::IFD-1], ZB4838 *bzIs166*[P$_{mec-4}$mCherry]; *sqst-1(ok2892)IV*; *bzSi3*[P$_{mec-7}$GFP::IFD-1]. Number of IFD-1 puncta per Ad2 ALM indicated. P < 0.005, N > 25, 3 trials, two-tailed t-test, error bars are SEM.

F) *sqst-1*(*ok2892*) impacts variation in exophergenesis without significantly changing outcome in the *bzIs166*[P$_{mec-4}$mCherry] background. Strains are ZB4065 *bzIs166*[P$_{mec-4}$mCherry], ZB4991 *bzIs166*[P$_{mec-4}$mCherry]; *sqst-1*(*ok2892*). We scored ALMR exophers at Ad2 in *bzIs101*[P$_{mec-4}$mCherry] compared to *bzIs166*[P$_{mec-4}$mCherry]; *sqst-1(ok2892)IV*. NS, N > 250, 9 trials. Cochran-Mantel-Haenszel, error bars are SEM.

G) SQST-1 localizes to the IFD-1 puncta. Representative of adult touch neuron expressing *bpIs151*[P$_{sqst-1}$SQST-1::GFP + *unc-76*(+)]; *bzEx261*[P$_{mec-7}$RFP::IFD-2]. Representative of N > 10. Scale bar = 2 µm.

Supplementary Figure 21. FTT-2/14-3-3 adapter protein of the BAG3/HSP1/14-3-3 complex influences aggresome formation and exopher levels.

A) **IFD-1-positive puncta size decreases in *ftt-2(n4426).*** Diameter, in µm, of Ad1 IFD-1-positive puncta in ALM neurons decreases in the *ftt-2* predicted null background, in a strain expressing *bzIs166*[P_{mec-4} mCherry]; *bzSi3*[P_{mec-7} GFP::IFD-1]. P < 0.0001, N > 50, 3 trials, two-tailed t-test, error bars are SEM. We measured on Ad1 to reduce animal-bagging consequences.

B) **IFD-1-positive puncta number per ALM neuron remains the same in control and *ftt-2(n4426).*** Number of IFD-1-positive inclusions in Ad1 ALM somas does not change in mutant *ftt-2(n4426)* versus WT in strains expressing *bzIs166*[P_{mec-4} mCherry]; *bzSi3*[P_{mec-7} GFP::IFD-1]. NS, P = 0.87, N > 50 / strain, Ad1, 3 trials, two-tailed t-test, error bars are SEM.

C) **14-3-3/FTT-2 is required for efficient exopher production.** There is a significant reduction of percentage of ALMR exopher production on Ad1 in the genomic deletion *ftt-2(n4426*) strain expressing *bzIs166*[P_{mec-4} mCherry]; *bzSi3*[P_{mec-7} GFP::IFD-1]; P < 0.05, N > 275, 8 trials, Animals measured on Ad1 to avoid animal-bagging. Cochran-Mantel-Haenszel test, error bars are SEM; Ad1.

D) **Additional FTT-2 gene dose increases ALMR exophergenesis.** We scored ALMR exopher production on Ad2 in control animals expressing *bzIs166*[P_{mec-4}mCherry] and *bzIs166*[P_{mec-4}mCherry]; *bzSi47*[P_{mec-7}FTT-2::mSc]. The wild type *ftt-2(+)* allele is present; use of the strong *mec-7* promoter for TN specific expression of the added *ftt-2* copy might elevate expression. Single-copy integrated P_{mec-7}FTT-2::mSc increases ALMR Ad2 exophergenesis, N > 95, P = 0.035, 3 trials, Ad2.

Supplementary Figure 22. Homologs of mammalian aggregate-adapter complex members FTT-2 and HSP-1 have roles in exopher production.

* P < 0.05, ** P < 0.005, *** P < 0.0005.

A) **Mammalian aggregate-adapter complex.** Adapted from paper Xu 2013 [45] created using BioRender.com. 14-3-3 proteins bind directly to dynein components. 14-3-3 binds BAG3 bound Hsc70/(HSP-1). Hsc70/HSP-1 is able to recognize and bind ubiquitinylated aggregates. The complex moves along the microtubule tracks to deliver to the aggresome compartment.

B) **RNAi targeting in all cells + touch neurons supports a 14-3-3/FTT-2 role in efficient exopher production.** We knocked down *ftt-2* in a touch neuron

sensitized RNAi strain expressing *bzIs169*[P_{mec-18}SID-1 P_{sng-1}YFP](other cells in addition to touch neurons can be targeted in this background). $P < 0.05$, $N > 85$, 3 trials, Cochran-Mantel-Haenszel test, error bars are SEM. We measured on Ad1 to reduce animal-bagging occurrence.

C) **Pan-neuronal-specific RNAi against *ftt-2* significantly reduces exophergenesis.** We targeted *ftt-2* RNAi clone in a pan-neuronal-specific RNAi strain expressing *sqIs71*[P_{rgef-1}GFP; P_{rgef-1}SID-1;pBS]; *sid-1(qt9)*V; *bzIs101*[P_{mec-4}mCherry] (only neurons subject to *ftt-2* knockdown) to observed significantly reduced Ad2 ALMR exophergenesis. $P = 0.0025$, 5 trials, $N = 250$, Cochran-Mantel-Haenszel test, error bars are SEM. Data are consistent with observations in the *ftt-2(n4426)* putative null mutant and support FTT-2 function in neurons is required for efficient exopher production.

D) **HSP-1 is required for efficient exopher production in a touch neuron-sensitized RNAi strain.** *hsp-1*-targeted RNAi from L4 to Ad2 in a neuronally-sensitized RNAi strain harboring *bzIs169* [P_{mec-18}*sid-1* P_{sng-1}YFP]; *bzIs101* [P_{mec-4}mCherry] (all cells + touch neurons targeting) significantly reduces ALM exophergenesis. Ad2 $P < 0.0005$, $N > 130$, 4 trials, Cochran-Mantel-Haenszel test, error bars are SEM.

Discussion. Note that fertility disruption can be a concern for some knockdowns ([14] and our unpublished observations). *ftt-2* is expressed in the somatic tissues [101] and knockdown does not block progeny production; we scored on Ad1 to avoid bagging and retention of progeny that can occur at Ad2. *hsp-1* is a more broadly expressed essential gene that can disrupt fertility; so RNAi knockdown, though anticipated to be enhanced in touch neurons [53] and not blocking all progeny production in our experiment, might still impair exophers by compromising fertility or other tissue health.

We tested but did not find evidence of a requirement for an *unc-23*/BAG3 mutation or RNAi on exophers (data not shown). BAG3 and UNC-23 are only partially overlapping and we speculate that the HSP-1/14-3-3 complex might be simpler in nematodes as compared to mammals, or another protein may provide the UNC-23 role in the complex.

To more firmly establish cell autonomy we constructed degron tagged alleles of *ftt-2* and *hsp-1* for later auxin-induced degradation in touch neurons. We found that *degron::hsp-1* was homozygous lethal; and *degron::ftt-2* was constitutively lowered for exopher production, even in the absence of auxin, suggesting the tagged variant alone reflects the null phenotype. Although we were unable to use AID for touch neuron specific degradation, the *degron::ftt-2* tag serves as an independent allele to confirm the exopher suppression phenotype.

Supplementary Figure 23. Human intermediate filament Neurofilament Light Chain (hNFL) can adopt multiple localization patterns in *C. elegans* touch neurons, but prominently localizes to 1 or 2 juxtanuclear inclusions.

A-D) Human hNFL can adopt multiple localization patterns when expressed in the *C. elegans* touch neurons – A) filamentous/cytoplasmic (Strain: ZB5345 *bzEx311*[P_{mec-7}mNG::hNFL];*bzIs166*[P_{mec-4}mCherry]; *ifd-2(bz187).* **B)** axonal (and punctate featured. **C)** nuclear (and punctate) featured. D) most commonly, juxtanuclear and punctate. Scale bar = 2 µm. **B-D:** Strain: ZB5175 *bzEx269*[P_{mec-7}mNG::hNFL];*bzSi34*[P_{mec-7}mSc::IFD-1].

E-K) Human mNG::hNFL forms juxtanuclear inclusions in either single copy or high copy array lines. E- Top - filamentous/ cytosolic localization (rare). Bottom – typical punctate/collected localization. Strain: ZB5593 *bzIs166*[P_{mec-4}mCherry];*bzEx311*[P_{mec-7}mNG::hNFL].

Top **(F, G, H**) quantification of integrated single copy strain ZB5332 *bzSi48*[P_{mec-7} mNG::hNFL]; *bzIs166*[P_{mec-4}mCherry]. Bottom **(I, J, K)** quantification of high copy array quantification of strain ZB5593 *bzIs166*[P_{mec-4}mCherry];*bzEx311*[P_{mec-7}mNG::hNFL]. Collected or cytosolic localization phenotype quantified in **F** and **I**. Juxtanuclear location quantified in **G** and **J**. Number of collected punctate quantified in **H** and **K**. Scale bar = 2 *µm*. Representative of N > 10.

Supplementary Figure 24. Single copy transgenic hNFL tagged protein is not dominant negative for exopher production nor exopher-elevating on this own.

A) Single copy mNG::hNFL does not affect Ad2 ALMR exopher percentage. P = 0.442, N > 94, 3 trials, Cochran-Mantel-Haenszel test, error bars are SEM. Strains: control ZB4065 *bzIs166*[P_{mec-4}mCherry] and ZB5332 *bzIs166*[P_{mec-4}mCherry];*bzSi48*[P_{mec-7}mNG::hNFL].

References:

1. López-Otín, C., et al., *The hallmarks of aging*. Cell, 2013. **153**(6): p. 1194-217.
2. Davis, A.A., C.E.G. Leyns, and D.M. Holtzman, *Intercellular Spread of Protein Aggregates in Neurodegenerative Disease.* Annu Rev Cell Dev Biol, 2018. **34**: p. 545-568.
3. Hipp, M.S., P. Kasturi, and F.U. Hartl, *The proteostasis network and its decline in ageing*. Nat Rev Mol Cell Biol, 2019. **20**(7): p. 421-435.
4. Melentijevic, I., et al., *C. elegans neurons jettison protein aggregates and mitochondria under neurotoxic stress.* Nature, 2017. **542**(7641): p. 367-371.

5. Arnold, M.L., et al., *Quantitative Approaches for Scoring in vivo Neuronal Aggregate and Organelle Extrusion in Large Exopher Vesicles in C. elegans.* J Vis Exp, 2020(163).
6. Donnelly, K.M., et al., *Phagocytic glia are obligatory intermediates in transmission of mutant huntingtin aggregates across neuronal synapses.* Elife, 2020. **9**.
7. Ray, A., S.D. Speese, and M.A. Logan, *Glial Draper Rescues Aβ Toxicity in a Drosophila Model of Alzheimer's Disease.* J Neurosci, 2017. **37**(49): p. 11881-11893.
8. Johnston, J.A., C.L. Ward, and R.R. Kopito, *Aggresomes: a cellular response to misfolded proteins.* J Cell Biol, 1998. **143**(7): p. 1883-98.
9. Garcia-Mata, R., Y.S. Gao, and E. Sztul, *Hassles with taking out the garbage: aggravating aggresomes.* Traffic, 2002. **3**(6): p. 388-96.
10. Kopito, R.R., *Aggresomes, inclusion bodies and protein aggregation.* Trends Cell Biol, 2000. **10**(12): p. 524-30.
11. Cooper, J.F., et al., *Stress increases in exopher-mediated neuronal extrusion require lipid biosynthesis, FGF, and EGF RAS/MAPK signaling.* Proc Natl Acad Sci U S A, 2021. **118**(36).
12. Choe, K.P., *Physiological and molecular mechanisms of salt and water homeostasis in the nematode Caenorhabditis elegans.* Am J Physiol Regul Integr Comp Physiol, 2013. **305**(3): p. R175-86.
13. Hartl, F.U., *Cellular Homeostasis and Aging.* Annu Rev Biochem, 2016. **85**: p. 1-4.
14. Turek, M., et al., *Muscle-derived exophers promote reproductive fitness.* EMBO Rep, 2021. **22**(8): p. e52071.
15. Gamerdinger, M., et al., *BAG3 mediates chaperone-based aggresome-targeting and selective autophagy of misfolded proteins.* EMBO Rep, 2011. **12**(2): p. 149-56.
16. García-Mata, R., et al., *Characterization and dynamics of aggresome formation by a cytosolic GFP-chimera.* J Cell Biol, 1999. **146**(6): p. 1239-54.
17. Gautreau, A., et al., *Isolation and characterization of an aggresome determinant in the NF2 tumor suppressor.* J Biol Chem, 2003. **278**(8): p. 6235-42.
18. Herrmann, H. and U. Aebi, *Intermediate filaments: molecular structure, assembly mechanism, and integration into functionally distinct intracellular Scaffolds.* Annu Rev Biochem, 2004. **73**: p. 749-89.
19. Herrmann, H. and U. Aebi, *Intermediate Filaments: Structure and Assembly.* Cold Spring Harb Perspect Biol, 2016. **8**(11).
20. Helfand, B.T., et al., *A role for intermediate filaments in determining and maintaining the shape of nerve cells.* Mol Biol Cell, 2003. **14**(12): p. 5069-81.
21. Julien, J.P., *A role for neurofilaments in the pathogenesis of amyotrophic lateral sclerosis.* Biochem Cell Biol, 1995. **73**(9-10): p. 593-7.
22. Perrot, R. and J. Eyer, *Neuronal intermediate filaments and neurodegenerative disorders.* Brain Res Bull, 2009. **80**(4-5): p. 282-95.
23. Taylor, J.P., et al., *Aggresomes protect cells by enhancing the degradation of toxic polyglutamine-containing protein.* Hum Mol Genet, 2003. **12**(7): p. 749-57.
24. Spillantini, M.G., et al., *alpha-Synuclein in filamentous inclusions of Lewy bodies from Parkinson's disease and dementia with lewy bodies.* Proc Natl Acad Sci U S A, 1998. **95**(11): p. 6469-73.
25. Loeffler, T., et al., *Neurofilament-Light Chain as Biomarker of Neurodegenerative and Rare Diseases With High Translational Value.* Front Neurosci, 2020. **14**: p. 579.

26. Lockhead, D., et al., *The tubulin repertoire of C. elegans sensory neurons and its context-dependent role in process outgrowth.* Mol Biol Cell, 2016. **27**(23): p. 3717-28.
27. Kaletsky, R., et al., *The C. elegans adult neuronal IIS/FOXO transcriptome reveals adult phenotype regulators.* Nature, 2016. **529**(7584): p. 92-6.
28. Hammarlund, M., et al., *The CeNGEN Project: The Complete Gene Expression Map of an Entire Nervous System.* Neuron, 2018. **99**(3): p. 430-433.
29. Karabinos, A., *Intermediate filament (IF) proteins IFA-1 and IFB-1 represent a basic heteropolymeric IF cytoskeleton of nematodes: A molecular phylogeny of nematode IFs.* Gene, 2019. **692**: p. 44-53.
30. Kurup, N., et al., *Intermediate filament accumulation can stabilize microtubules in Caenorhabditis elegans motor neurons.* Proc Natl Acad Sci U S A, 2018. **115**(12): p. 3114-3119.
31. Carberry, K., et al., *Intermediate filaments in Caenorhabditis elegans.* Cell Motil Cytoskeleton, 2009. **66**(10): p. 852-64.
32. Geisler, F., et al., *Intestinal intermediate filament polypeptides in C. elegans: Common and isotype-specific contributions to intestinal ultrastructure and function.* Sci Rep, 2020. **10**(1): p. 3142.
33. Geisler, F., et al., *The intestinal intermediate filament network responds to and protects against microbial insults and toxins.* Development, 2019. **146**(2).
34. Leiers, B., et al., *A stress-responsive glutathione S-transferase confers resistance to oxidative stress in Caenorhabditis elegans.* Free Radic Biol Med, 2003. **34**(11): p. 1405-15.
35. Frøkjær-Jensen, C., et al., *Improved Mos1-mediated transgenesis in C. elegans.* Nat Methods, 2012. **9**(2): p. 117-8.
36. Sarov, M., et al., *A genome-scale resource for in vivo tag-based protein function exploration in C. elegans.* Cell, 2012. **150**(4): p. 855-66.
37. Lai, C.C., et al., *Sequence and transmembrane topology of MEC-4, an ion channel subunit required for mechanotransduction in Caenorhabditis elegans.* J Cell Biol, 1996. **133**(5): p. 1071-81.
38. Zhang, L., et al., *The auxin-inducible degradation (AID) system enables versatile conditional protein depletion in C. elegans.* Development, 2015. **142**(24): p. 4374-84.
39. Jia, B., Y. Wu, and Y. Zhou, *14-3-3 and aggresome formation: implications in neurodegenerative diseases.* Prion, 2014. **8**(2): p. 173-7.
40. Kawaguchi, Y., et al., *The deacetylase HDAC6 regulates aggresome formation and cell viability in response to misfolded protein stress.* Cell, 2003. **115**(6): p. 727-38.
41. Zhou, L., et al., *p62/sequestosome 1 regulates aggresome formation of pathogenic ataxin-3 with expanded polyglutamine.* Int J Mol Sci, 2014. **15**(9): p. 14997-5010.
42. Chalfie, M. and J.N. Thomson, *Structural and functional diversity in the neuronal microtubules of Caenorhabditis elegans.* J Cell Biol, 1982. **93**(1): p. 15-23.
43. Bounoutas, A., R. O'Hagan, and M. Chalfie, *The multipurpose 15-protofilament microtubules in C. elegans have specific roles in mechanosensation.* Curr Biol, 2009. **19**(16): p. 1362-7.
44. Matsumoto, G., et al., *N-Acyldopamine induces aggresome formation without proteasome inhibition and enhances protein aggregation via p62/SQSTM1 expression.* Sci Rep, 2018. **8**(1): p. 9585.

45. Xu, Z., et al., *14-3-3 protein targets misfolded chaperone-associated proteins to aggresomes.* J Cell Sci, 2013. **126**(Pt 18): p. 4173-86.
46. Kolodziejska, K.E., et al., *Regulation of inducible nitric oxide synthase by aggresome formation.* Proc Natl Acad Sci U S A, 2005. **102**(13): p. 4854-9.
47. Zaarur, N., et al., *Proteasome failure promotes positioning of lysosomes around the aggresome via local block of microtubule-dependent transport.* Mol Cell Biol, 2014. **34**(7): p. 1336-48.
48. Brignull, H.R., et al., *Polyglutamine proteins at the pathogenic threshold display neuron-specific aggregation in a pan-neuronal Caenorhabditis elegans model.* J Neurosci, 2006. **26**(29): p. 7597-606.
49. Parker, J.A., et al., *Expanded polyglutamines in Caenorhabditis elegans cause axonal abnormalities and severe dysfunction of PLM mechanosensory neurons without cell death.* Proc Natl Acad Sci U S A, 2001. **98**(23): p. 13318-23.
50. Narain, Y., et al., *A molecular investigation of true dominance in Huntington's disease.* J Med Genet, 1999. **36**(10): p. 739-46.
51. Kostich, M., A. Fire, and D.M. Fambrough, *Identification and molecular-genetic characterization of a LAMP/CD68-like protein from Caenorhabditis elegans.* J Cell Sci, 2000. **113 (Pt 14)**: p. 2595-606.
52. Yan, J., et al., *SQSTM1/p62 interacts with HDAC6 and regulates deacetylase activity.* PLoS One, 2013. **8**(9): p. e76016.
53. Calixto, A., et al., *Enhanced neuronal RNAi in C. elegans using SID-1.* Nat Methods, 2010. **7**(7): p. 554-9.
54. Mignot, C., et al., *Dynamics of mutated GFAP aggregates revealed by real-time imaging of an astrocyte model of Alexander disease.* Exp Cell Res, 2007. **313**(13): p. 2766-79.
55. Mayer, R.J., et al., *Intermediate filament-ubiquitin diseases: implications for cell sanitization.* Biochem Soc Symp, 1989. **55**: p. 193-201.
56. Nicolás-Ávila, J., M. Sánchez-Diaz, and A. Hidalgo, *Isolation of exophers from cardiomyocyte-reporter mouse strains by fluorescence-activated cell sorting.* STAR Protoc, 2021. **2**(1): p. 100286.
57. Siddique, I., et al., *Exophers are components of mammalian cell neurobiology in health and disease.* bioRxiv, 2021: p. 2021.12.06.471479.
58. Hengartner, M.O. and H.R. Horvitz, *C. elegans cell survival gene ced-9 encodes a functional homolog of the mammalian proto-oncogene bcl-2.* Cell, 1994. **76**(4): p. 665-76.
59. Lewczuk, P., et al., *Plasma neurofilament light as a potential biomarker of neurodegeneration in Alzheimer's disease.* Alzheimers Res Ther, 2018. **10**(1): p. 71.
60. Ashton, N.J., et al., *A multicentre validation study of the diagnostic value of plasma neurofilament light.* Nat Commun, 2021. **12**(1): p. 3400.
61. Redemann, S., et al., *Codon adaptation-based control of protein expression in C. elegans.* Nat Methods, 2011. **8**(3): p. 250-2.
62. Choong, C.J., et al., *Alternative mitochondrial quality control mediated by extracellular release.* Autophagy, 2020: p. 1-13.
63. Nicolás-Ávila, J.A., et al., *A Network of Macrophages Supports Mitochondrial Homeostasis in the Heart.* Cell, 2020. **183**(1): p. 94-109.e23.

64. Nicolás-Ávila, J.Á., M. Sánchez-Diaz, and A. Hidalgo *Isolation of exophers from cardiomyocyte-reporter mouse strains by fluorescence-activated cell sorting*. STAR protocols, 2021. **2**, 100286 DOI: 10.1016/j.xpro.2020.100286.
65. Zhang, K., et al., *TREM2(hi) resident macrophages protect the septic heart by maintaining cardiomyocyte homeostasis.* Nat Metab, 2023.
66. Grune, J., et al., *Neutrophils incite and macrophages avert electrical storm after myocardial infarction.* Nat Cardiovasc Res, 2022. **1**(7): p. 649-664.
67. Lampinen, R., et al., *Neuron-astrocyte transmitophagy is altered in Alzheimer's disease.* Neurobiol Dis, 2022. **170**: p. 105753.
68. Nicolás-Ávila, J.A., et al., *Macrophages, Metabolism and Heterophagy in the Heart.* Circ Res, 2022. **130**(3): p. 418-431.
69. Johnston, H.E. and R.S. Samant, *Alternative systems for misfolded protein clearance: life beyond the proteasome.* Febs j, 2020.
70. Guthrie, C.R., G.D. Schellenberg, and B.C. Kraemer, *SUT-2 potentiates tau-induced neurotoxicity in Caenorhabditis elegans.* Hum Mol Genet, 2009. **18**(10): p. 1825-38.
71. Guthrie, C.R., et al., *MSUT2 is a determinant of susceptibility to tau neurotoxicity.* Hum Mol Genet, 2011. **20**(10): p. 1989-99.
72. Civelek, M., et al., *The polyphenol quercetin protects from glucotoxicity depending on the aggresome in Caenorhabditis elegans.* Eur J Nutr, 2020. **59**(2): p. 485-491.
73. Morrow, C.S., et al., *Vimentin Coordinates Protein Turnover at the Aggresome during Neural Stem Cell Quiescence Exit.* Cell Stem Cell, 2020. **26**(4): p. 558-568.e9.
74. Underwood, R., et al., *14-3-3 mitigates alpha-synuclein aggregation and toxicity in the in vivo preformed fibril model.* Acta Neuropathol Commun, 2021. **9**(1): p. 13.
75. Lu, M., et al., *Expression-level dependent perturbation of cell proteostasis and nuclear morphology by aggregation-prone polyglutamine proteins.* Biotechnol Bioeng, 2015. **112**(9): p. 1883-92.
76. Fisher, R.S., et al., *An apparent core/shell architecture of polyQ aggregates in the aging Caenorhabditis elegans neuron.* Protein Sci, 2021. **30**(7): p. 1482-1486.
77. Lu, M., et al., *Live-cell super-resolution microscopy reveals a primary role for diffusion in polyglutamine-driven aggresome assembly*. J Biol Chem, 2019. **294**(1): p. 257-268.
78. Erpapazoglou, Z., O. Walker, and R. Haguenauer-Tsapis, *Versatile roles of k63-linked ubiquitin chains in trafficking.* Cells, 2014. **3**(4): p. 1027-88.
79. Hao, R., et al., *Proteasomes activate aggresome disassembly and clearance by producing unanchored ubiquitin chains.* Mol Cell, 2013. **51**(6): p. 819-28.
80. Arnold, M.L., et al., *Q&A: Trash talk: disposal and remote degradation of neuronal garbage*. BMC Biol, 2018. **16**(1): p. 17.
81. Morrow, C.S. and D.L. Moore, *Vimentin's side gig: Regulating cellular proteostasis in mammalian systems.* Cytoskeleton (Hoboken), 2020. **77**(11): p. 515-523.
82. Krtková, J., et al., *14-3-3 Regulates Actin Filament Formation in the Deep-Branching Eukaryote Giardia lamblia.* mSphere, 2017. **2**(5).
83. Sluchanko, N.N. and N.B. Gusev, *14-3-3 proteins and regulation of cytoskeleton.* Biochemistry (Mosc), 2010. **75**(13): p. 1528-46.
84. Lee, Y., et al., *Neurofilament Proteins as Prognostic Biomarkers in Neurological Disorders.* Curr Pharm Des, 2020. **25**(43): p. 4560-4569.

85. Bacioglu, M., et al., *Neurofilament Light Chain in Blood and CSF as Marker of Disease Progression in Mouse Models and in Neurodegenerative Diseases.* Neuron, 2016. **91**(1): p. 56-66.
86. Gordon, B.A., *Neurofilaments in disease: what do we know?* Curr Opin Neurobiol, 2020. **61**: p. 105-115.
87. Gentil, B.J., M. Tibshirani, and H.D. Durham, *Neurofilament dynamics and involvement in neurological disorders.* Cell Tissue Res, 2015. **360**(3): p. 609-20.
88. Lépinoux-Chambaud, C. and J. Eyer, *Review on intermediate filaments of the nervous system and their pathological alterations.* Histochem Cell Biol, 2013. **140**(1): p. 13-22.
89. Goldman, J.E., et al., *Lewy bodies of Parkinson's disease contain neurofilament antigens.* Science, 1983. **221**(4615): p. 1082-4.
90. Aljohani, M.D., et al., *Engineering rules that minimize germline silencing of transgenes in simple extrachromosomal arrays in C. elegans.* Nat Commun, 2020. **11**(1): p. 6300.
91. Grishok, A., J.L. Sinskey, and P.A. Sharp, *Transcriptional silencing of a transgene by RNAi in the soma of C. elegans.* Genes Dev, 2005. **19**(6): p. 683-96.
92. Bolte, S. and F.P. Cordelières, *A guided tour into subcellular colocalization analysis in light microscopy.* J Microsc, 2006. **224**(Pt 3): p. 213-32.
93. Meriin, A.B., et al., *Hsp70-Bag3 complex is a hub for proteotoxicity-induced signaling that controls protein aggregation.* Proc Natl Acad Sci U S A, 2018. **115**(30): p. E7043-e7052.
94. Jones, D., et al., *A portable regulatory element directs specific expression of the Caenorhabditis elegans ubiquitin gene ubq-2 in the somatic gonad.* Dev Biol, 1995. **171**(1): p. 60-72.
95. Sampuda, K.M., M. Riley, and L. Boyd, *Stress induced nuclear granules form in response to accumulation of misfolded proteins in Caenorhabditis elegans.* BMC Cell Biol, 2017. **18**(1): p. 18.
96. Bakowski, M.A., et al., *Ubiquitin-mediated response to microsporidia and virus infection in C. elegans.* PLoS Pathog, 2014. **10**(6): p. e1004200.
97. Gamerdinger, M., S. Carra, and C. Behl, *Emerging roles of molecular chaperones and co-chaperones in selective autophagy: focus on BAG proteins.* J Mol Med (Berl), 2011. **89**(12): p. 1175-82.
98. Geisler, F., et al., *Intestinal intermediate filament polypeptides in C. elegans: Common and isotype-specific contributions to intestinal ultrastructure and function.* Scientific Reports, 2020. **10**(1): p. 3142.
99. Toth, M.L., et al., *Neurite sprouting and synapse deterioration in the aging Caenorhabditis elegans nervous system.* J Neurosci, 2012. **32**(26): p. 8778-90.
100. Liang, Q., et al., *The C. elegans ATG101 homolog EPG-9 directly interacts with EPG-1/Atg13 and is essential for autophagy.* Autophagy, 2012. **8**(10): p. 1426-33.
101. Aristizábal-Corrales, D., et al., *The 14-3-3 gene par-5 is required for germline development and DNA damage response in Caenorhabditis elegans.* J Cell Sci, 2012. **125**(Pt 7): p. 1716-26.

Intermediate Filaments Associated with Aggresome-like Structures in Proteostressed *C. elegans* Neurons and Influence the Rate of Large Vesicle Extrusion as Exophers

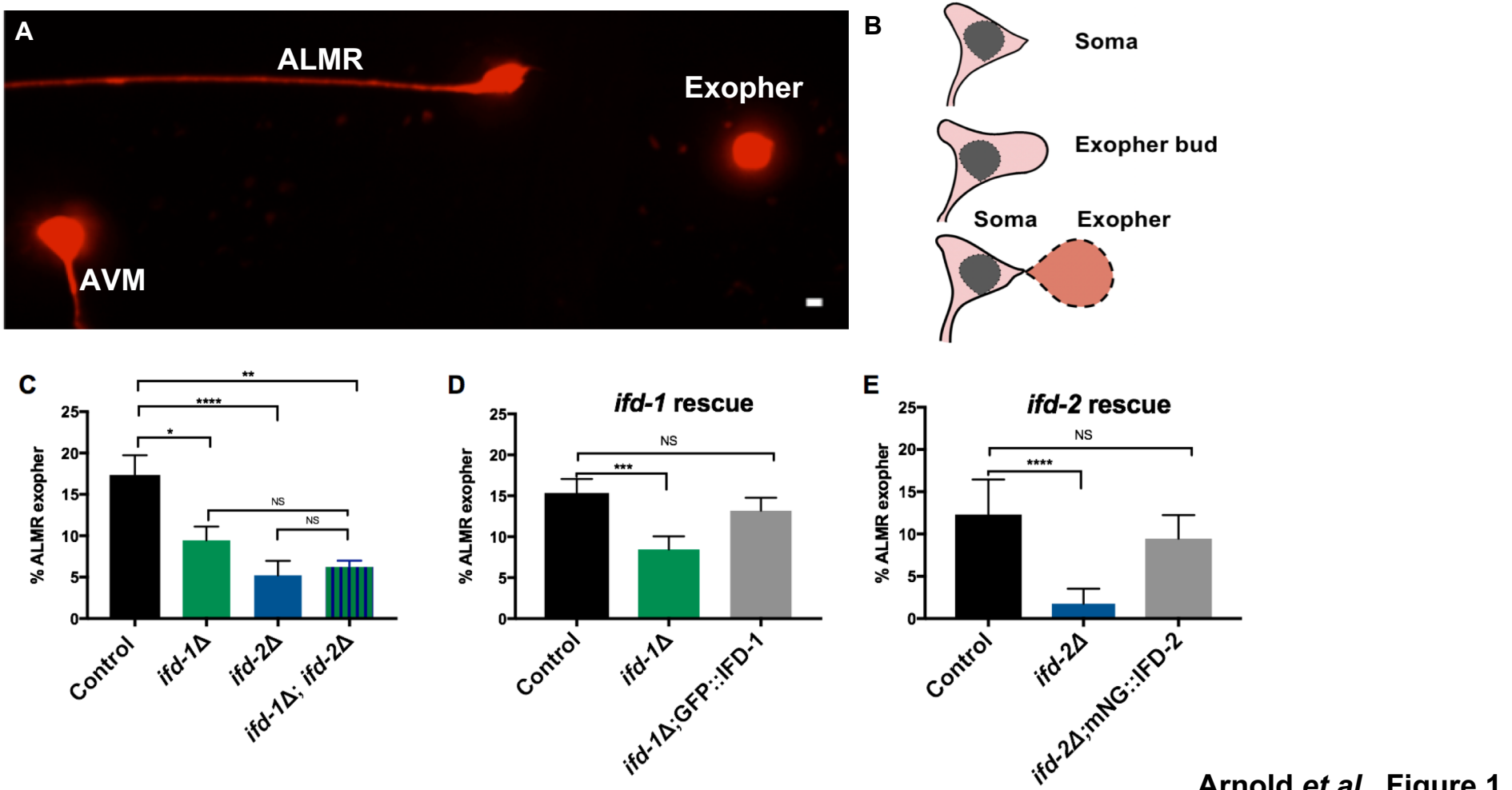

Arnold *et al.*, Figure 1

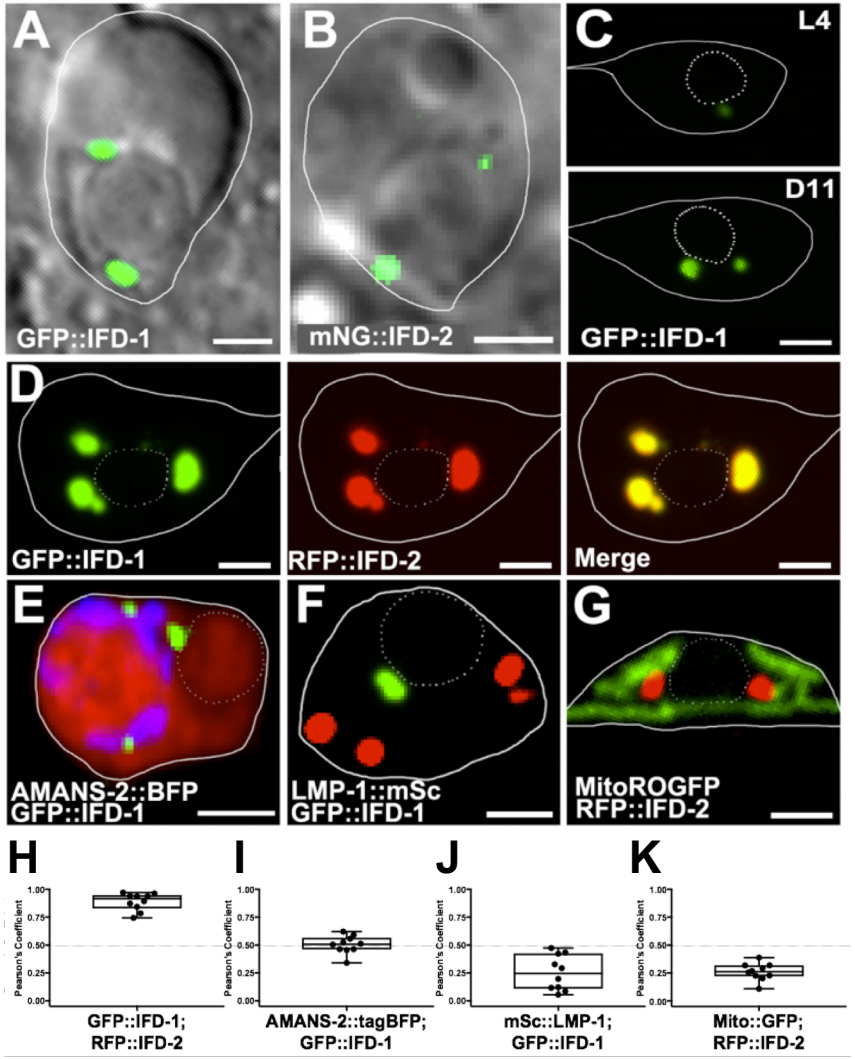

Arnold *et al.*, Figure 2

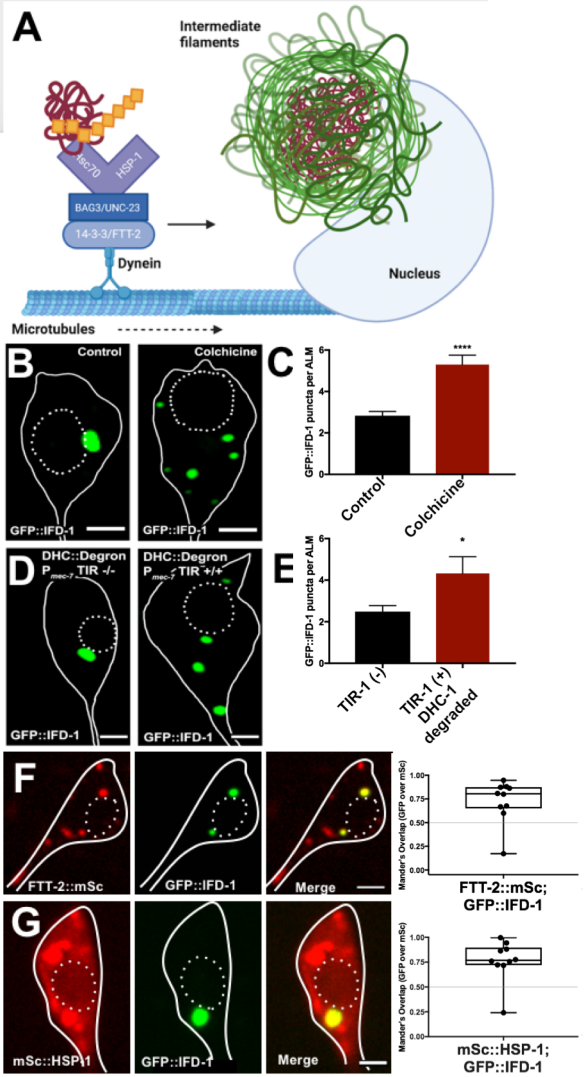

Arnold *et al.*, Figure 3

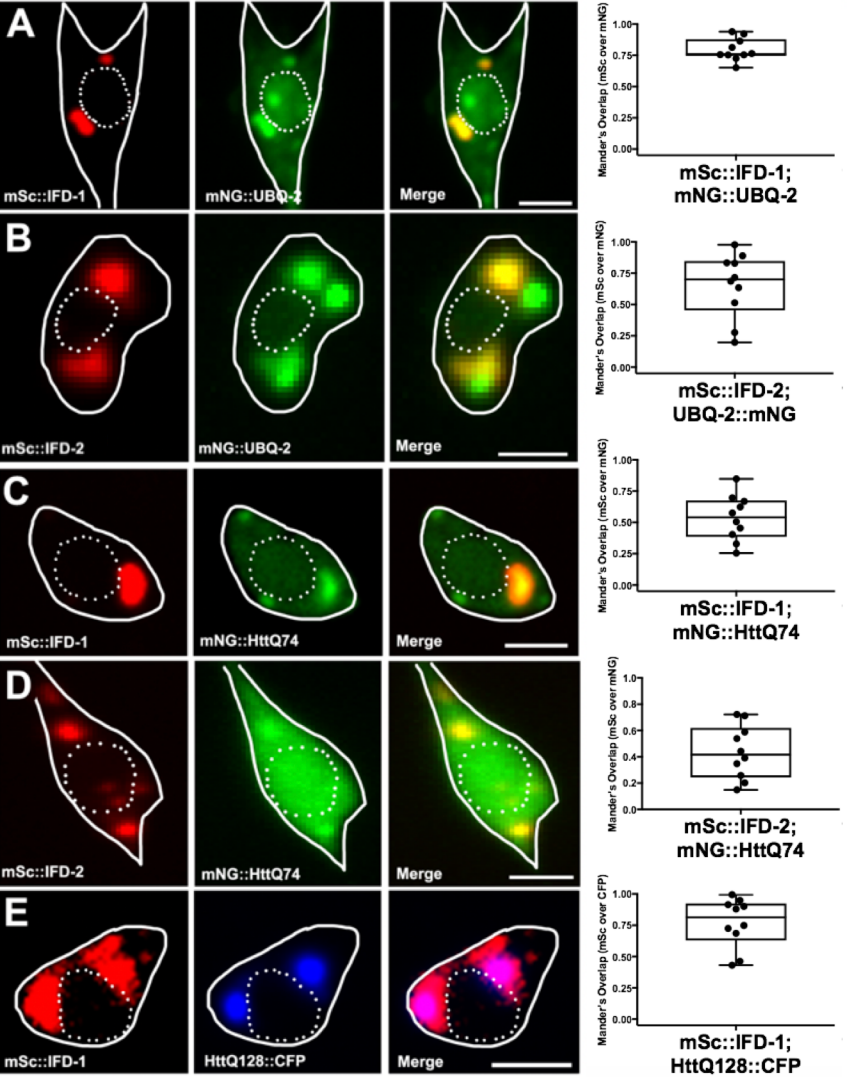

Arnold *et al.*, Figure 4

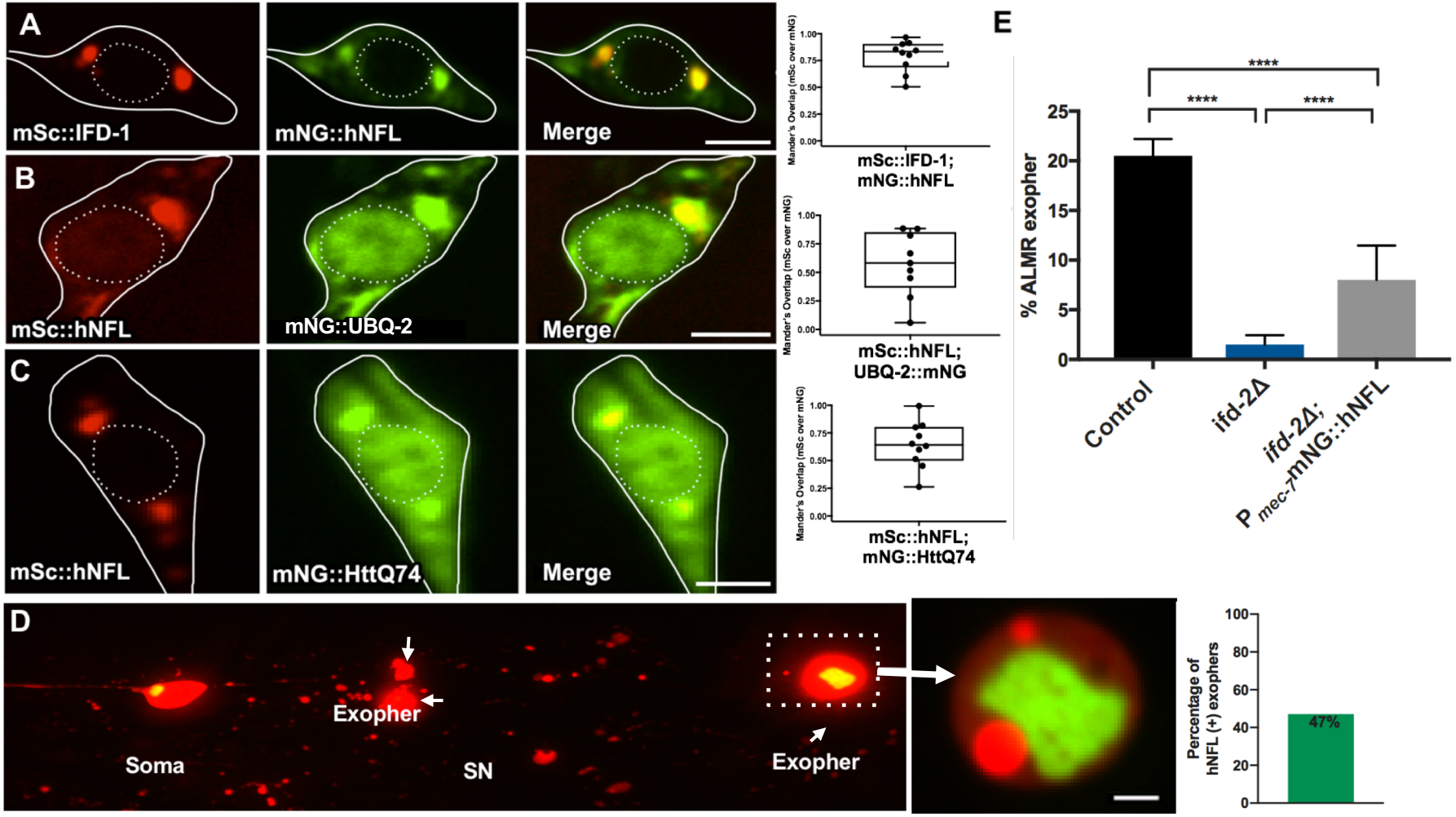

Arnold *et al.*, Figure 5

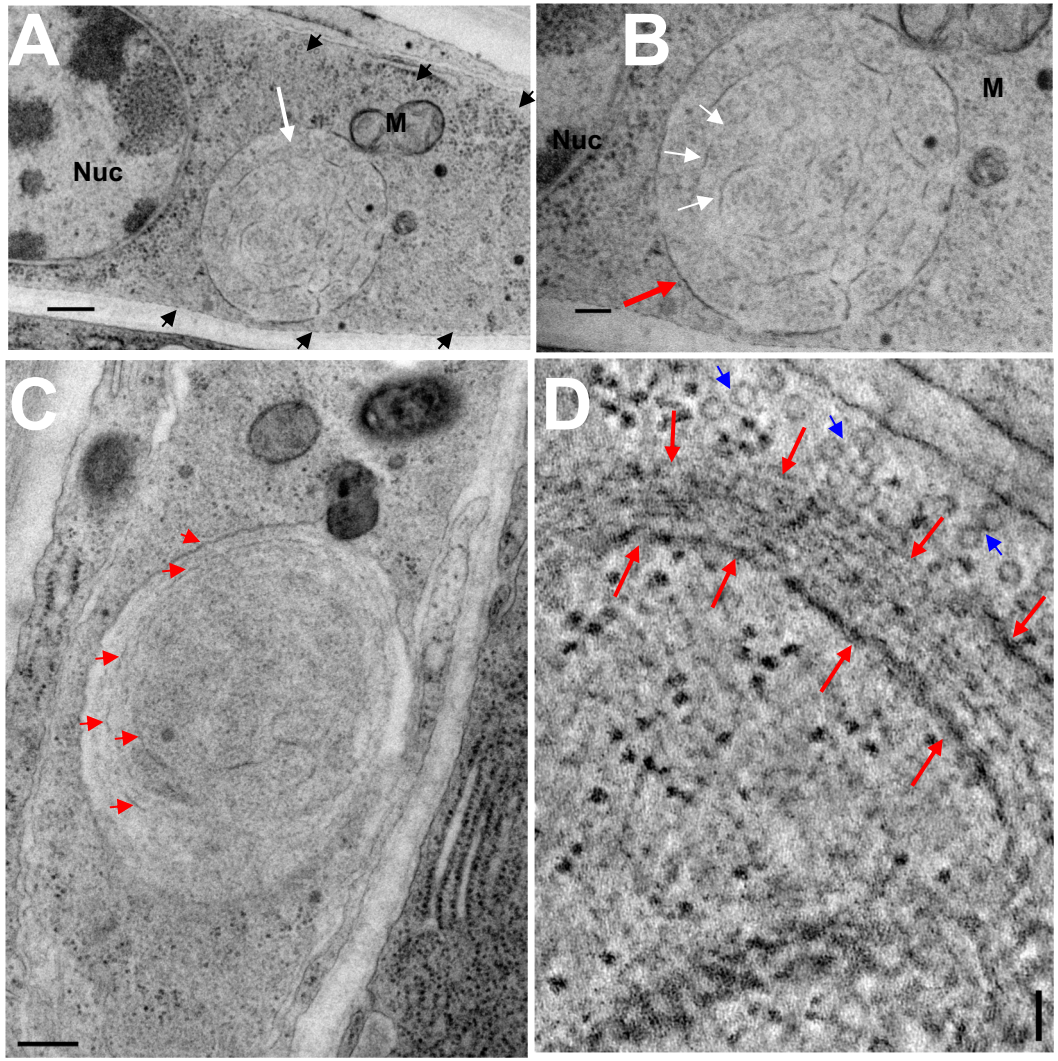

Arnold *et al.*,
Supplementary Figure 1

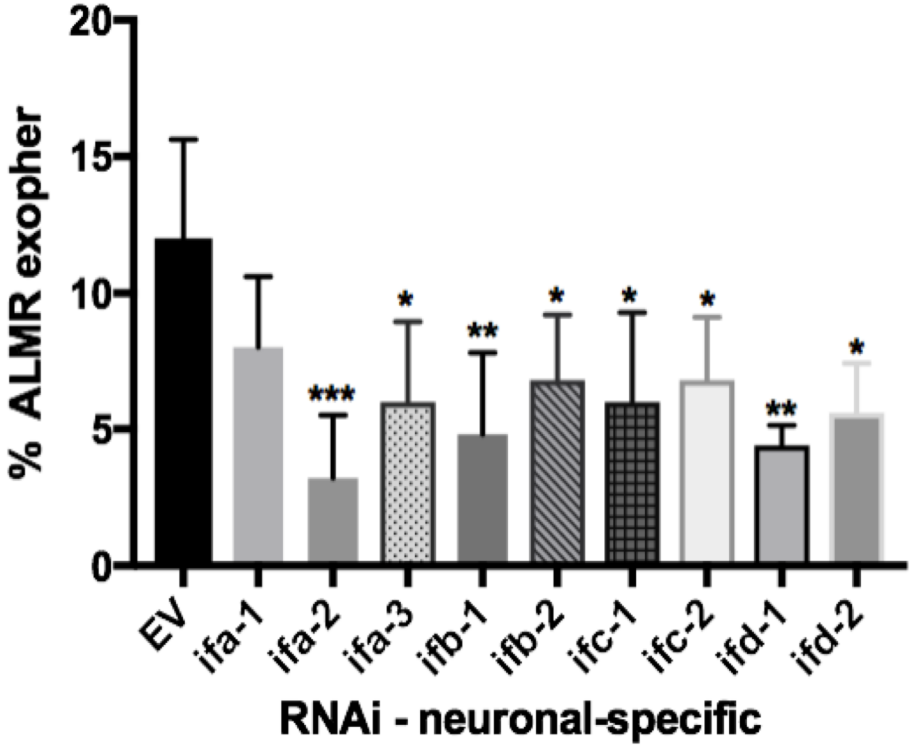

Arnold *et al.*,
Supplementary Figure 2

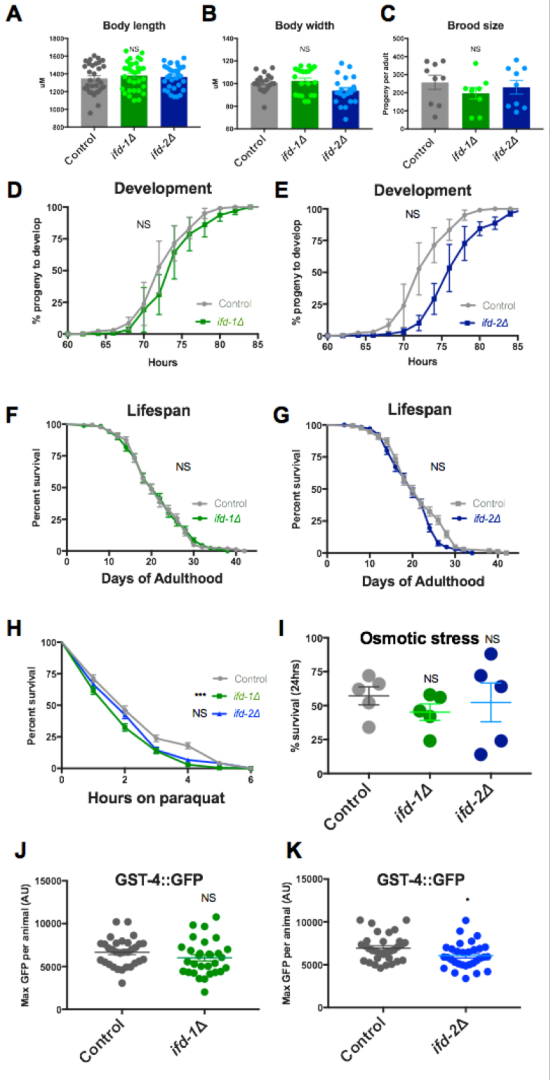

Arnold *et al.*,
Supplementary Figure 3

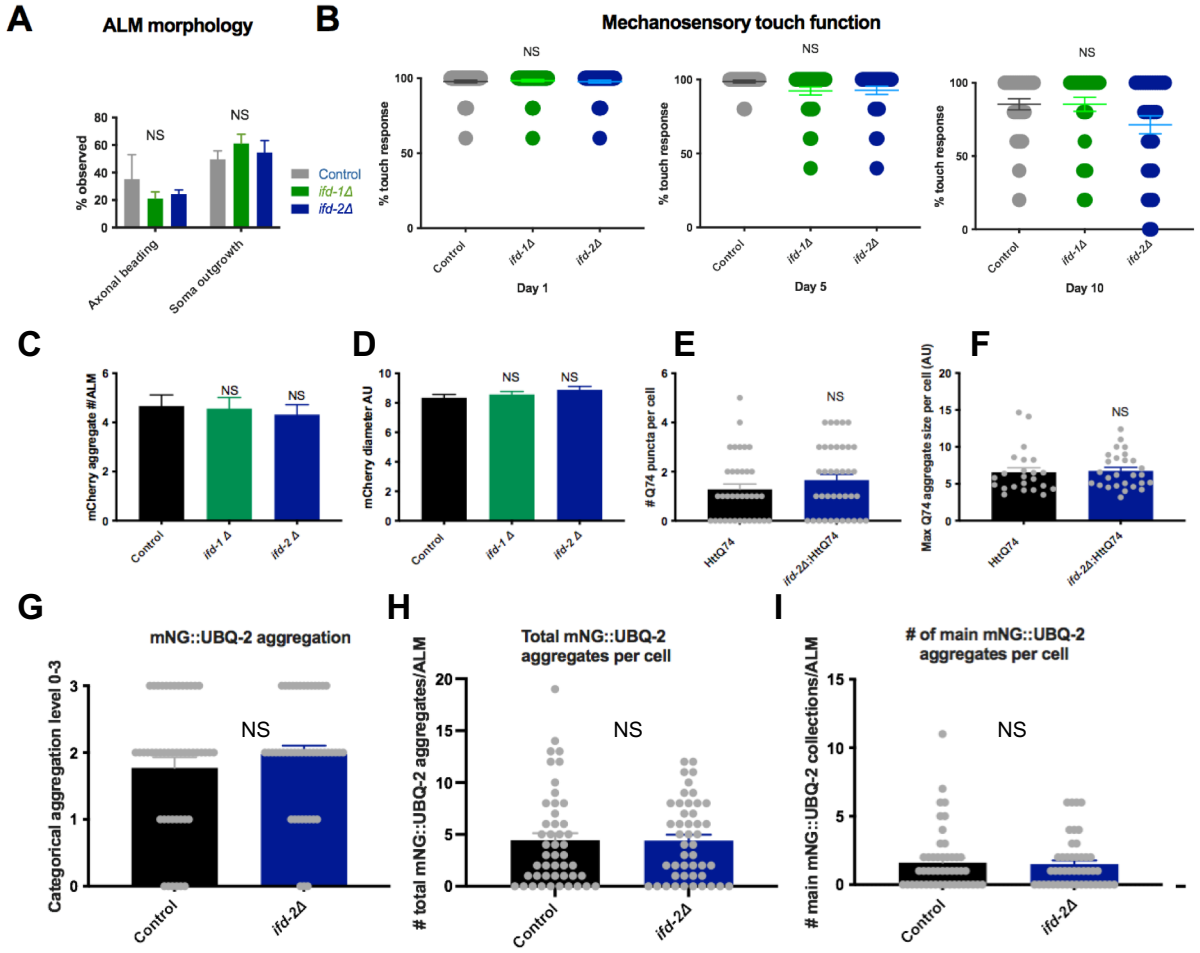

Arnold *et al.*, Supplementary Figure 4

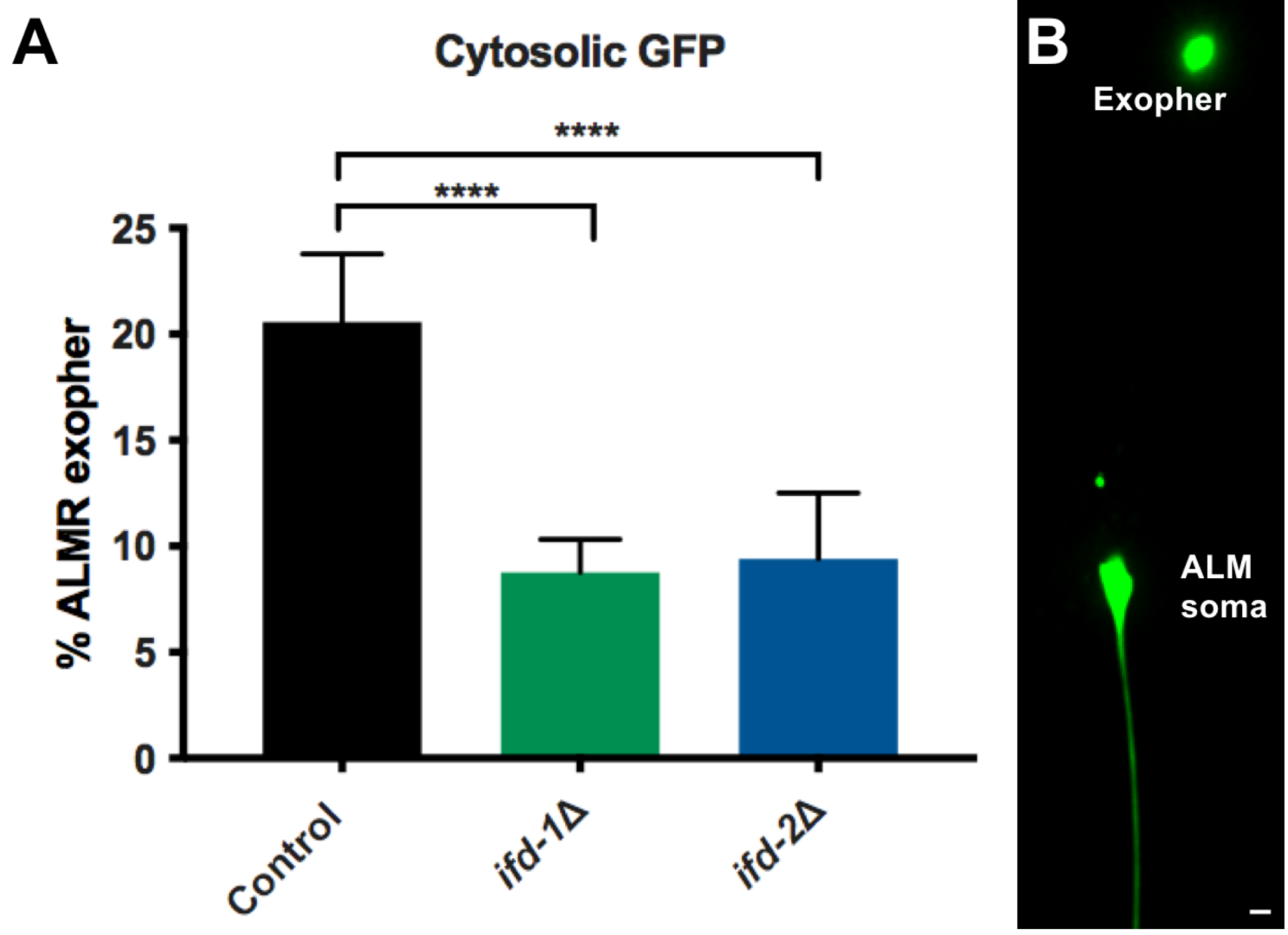

Arnold *et al.*,
Supplementary Figure 5

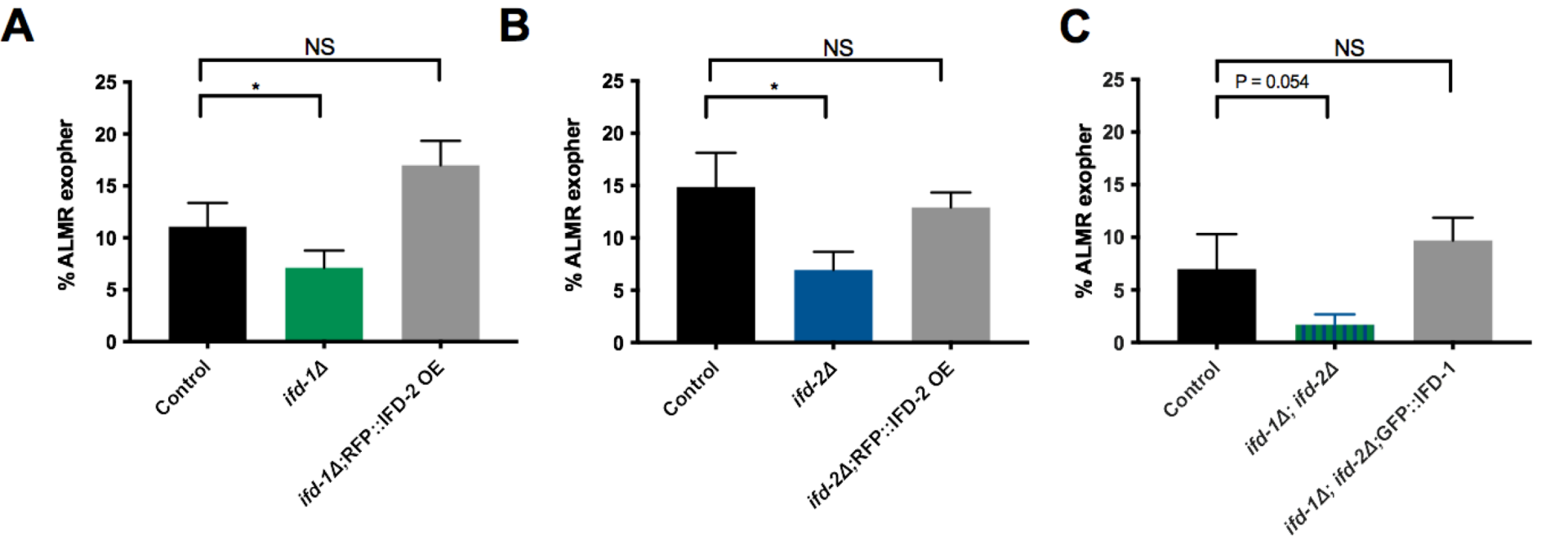

Arnold *et al.*,
Supplementary Figure 6

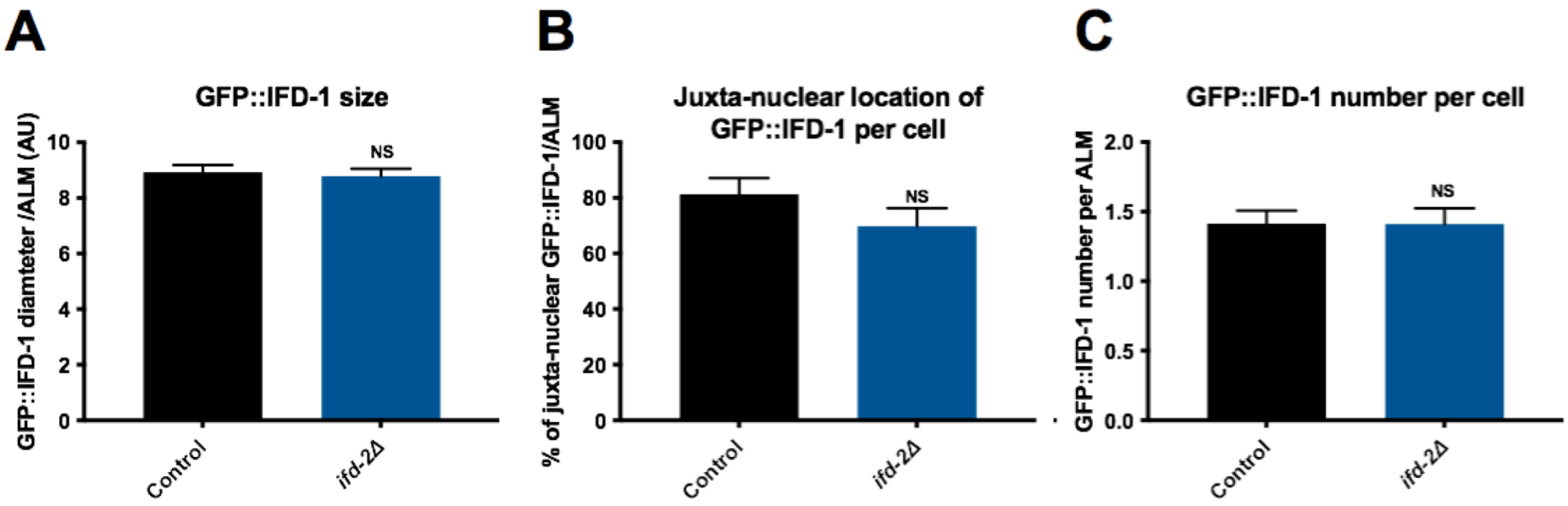

Arnold *et al.*,
Supplementary Figure 7

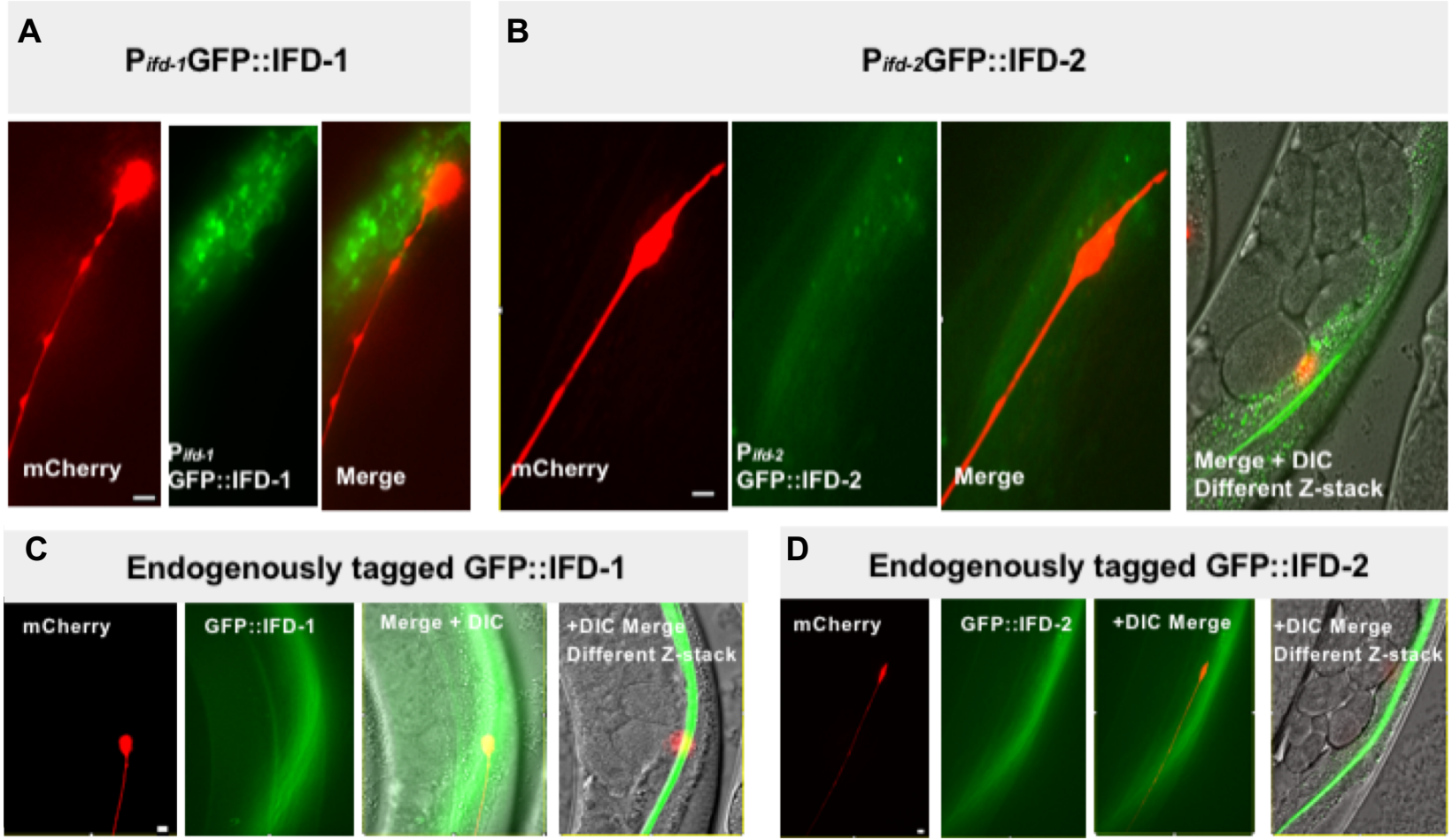

Arnold *et al.*,
Supplementary Figure 8

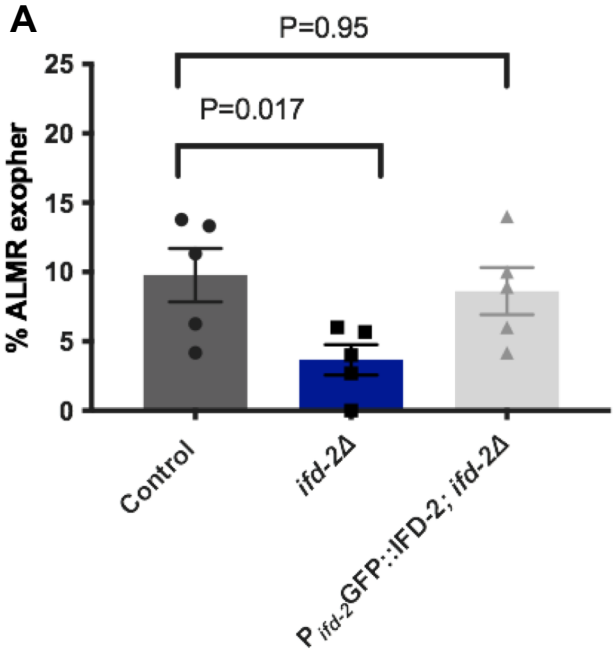

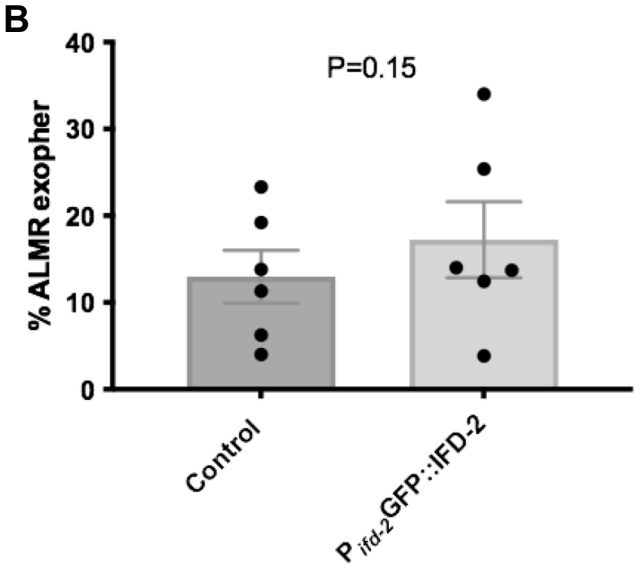

Arnold *et al.*,
Supplementary Figure 9

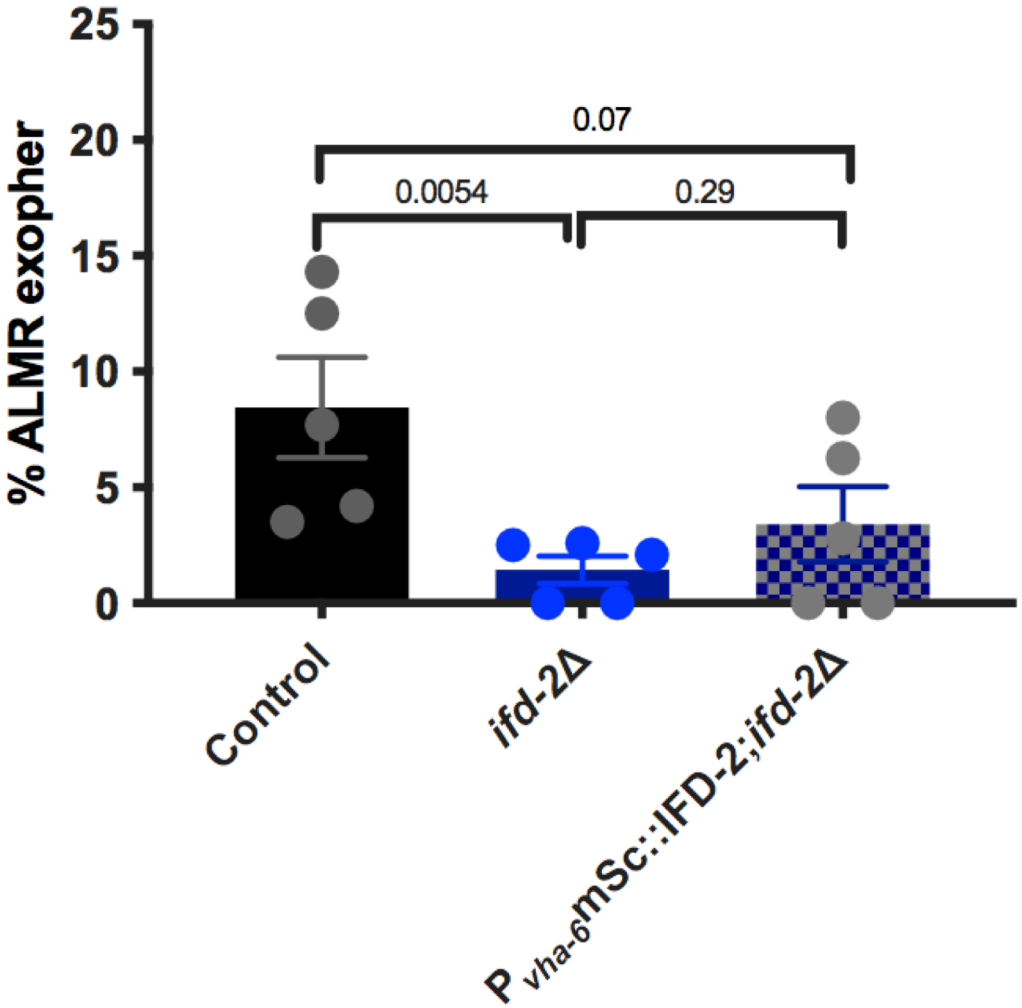

Arnold *et al.*,
Supplementary Figure 10

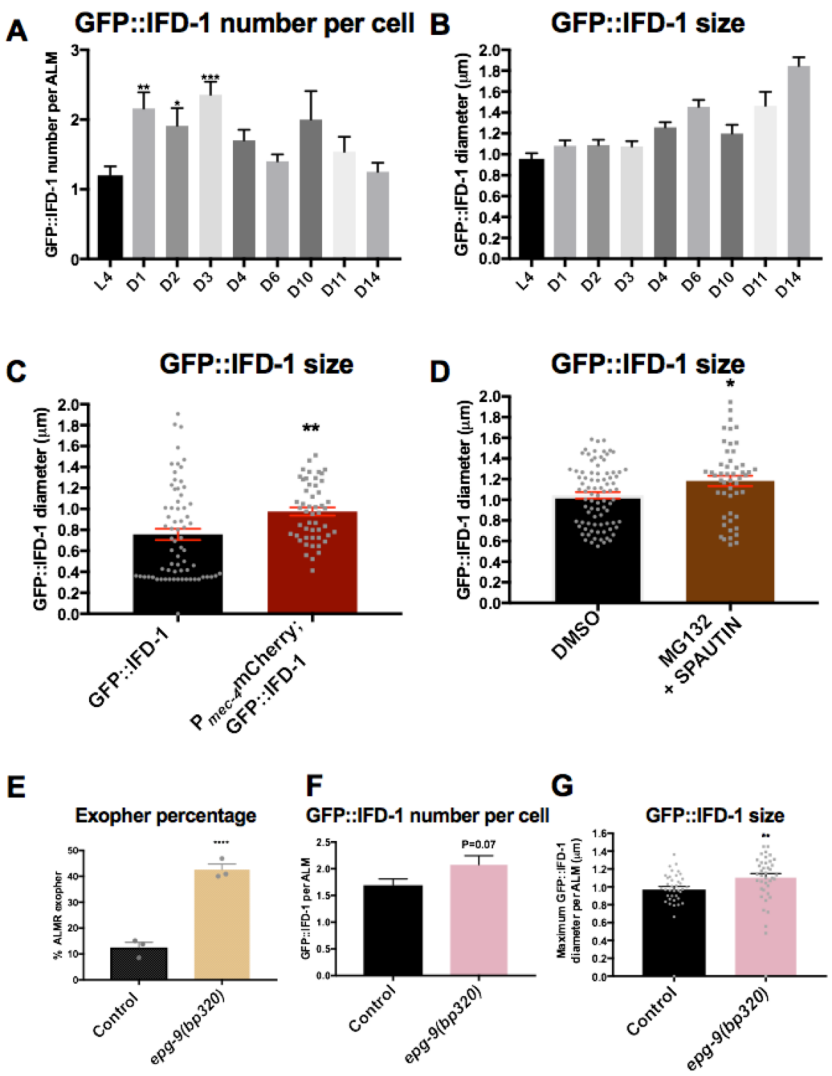

Arnold *et al.*,
Supplementary Figure 11

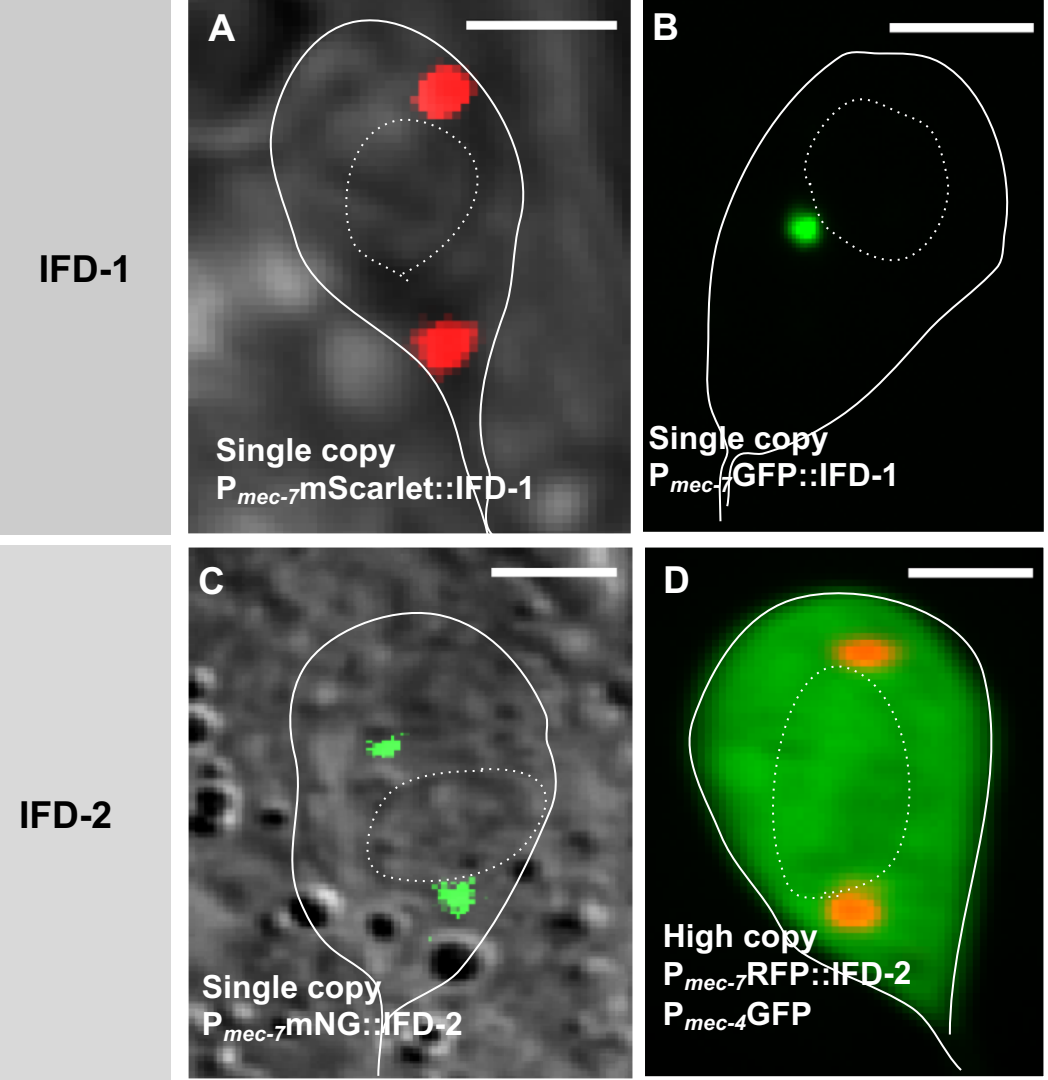

Arnold *et al.*,
Supplementary Figure 12

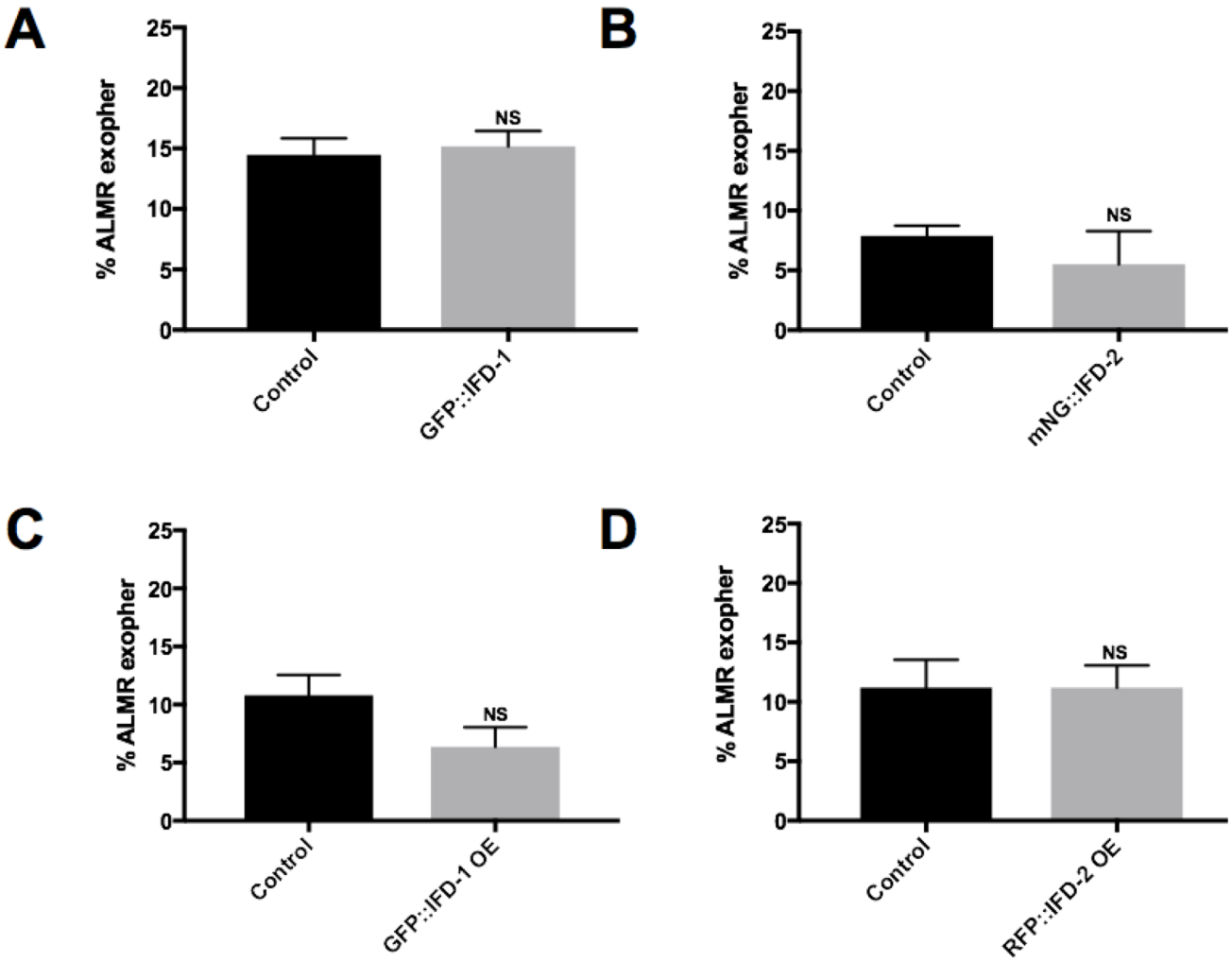

Arnold *et al.*,
Supplementary Figure 13

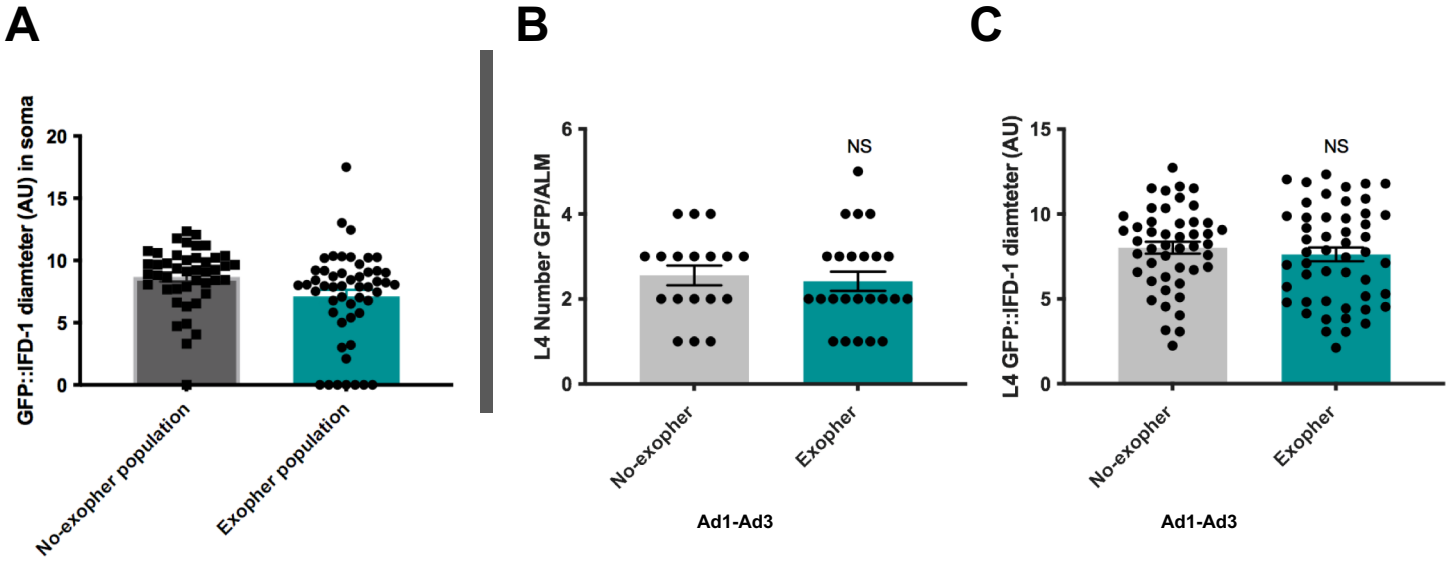

Arnold *et al.*,
Supplementary Figure 14

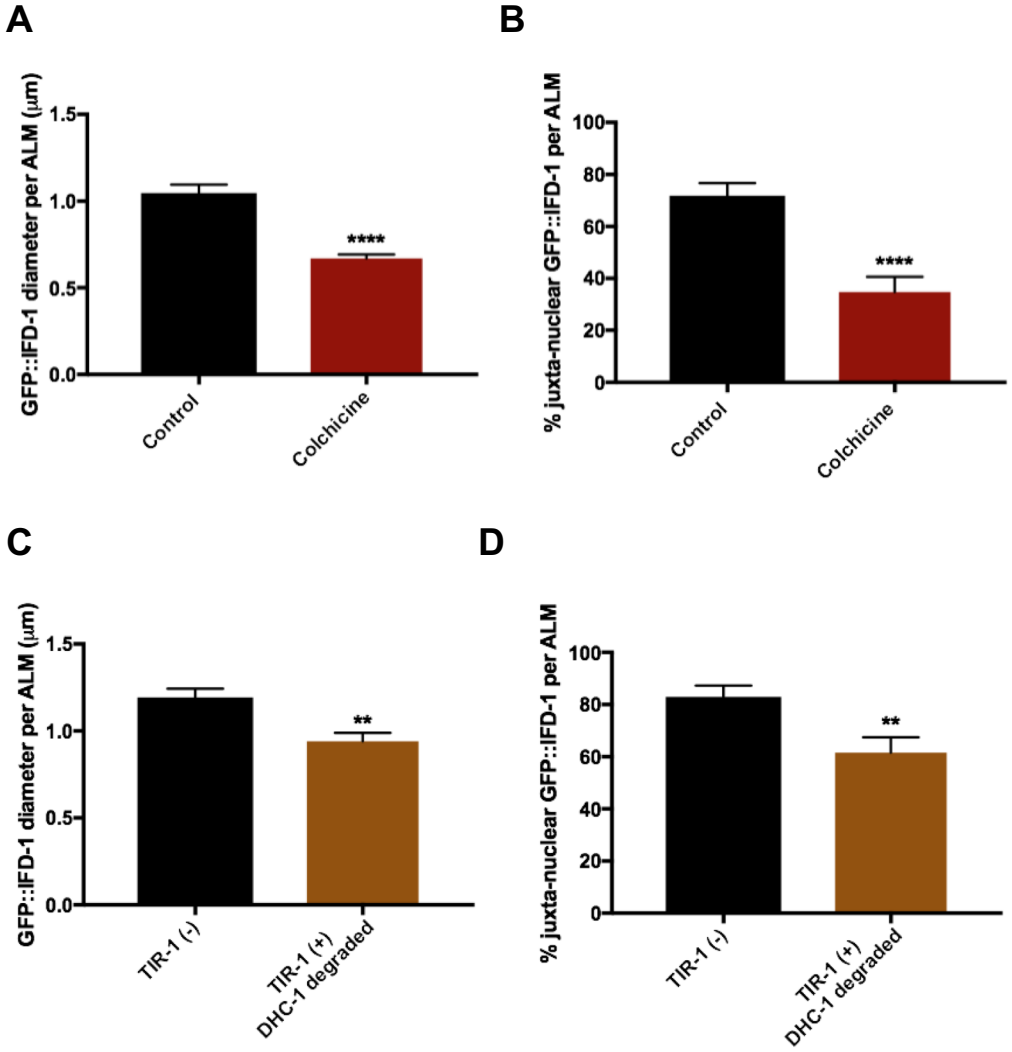

Arnold *et al.*,
Supplementary Figure 15

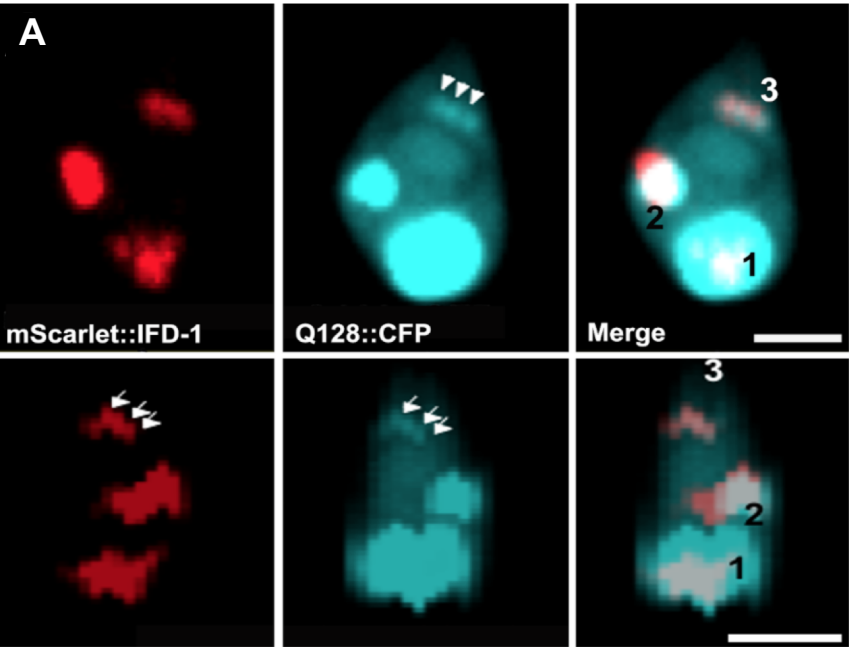

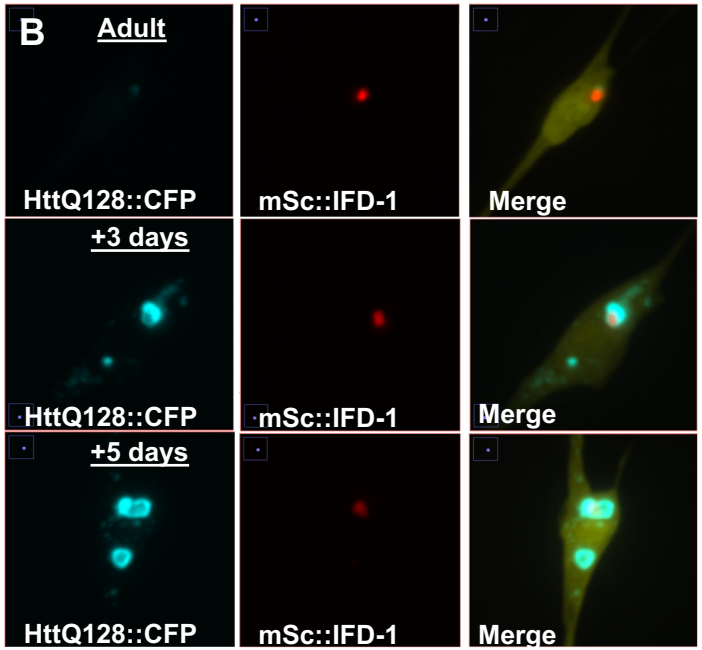

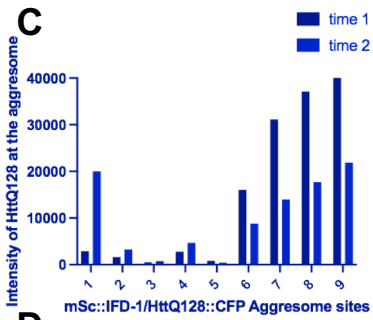

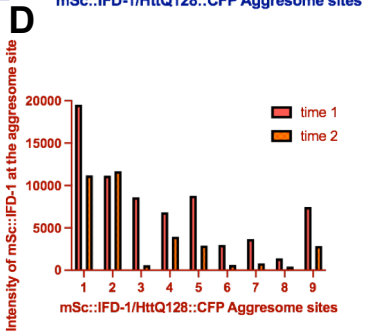

Arnold *et al.*,
Supplementary Figure 16

Arnold *et al.*,
Supplementary Figure 17

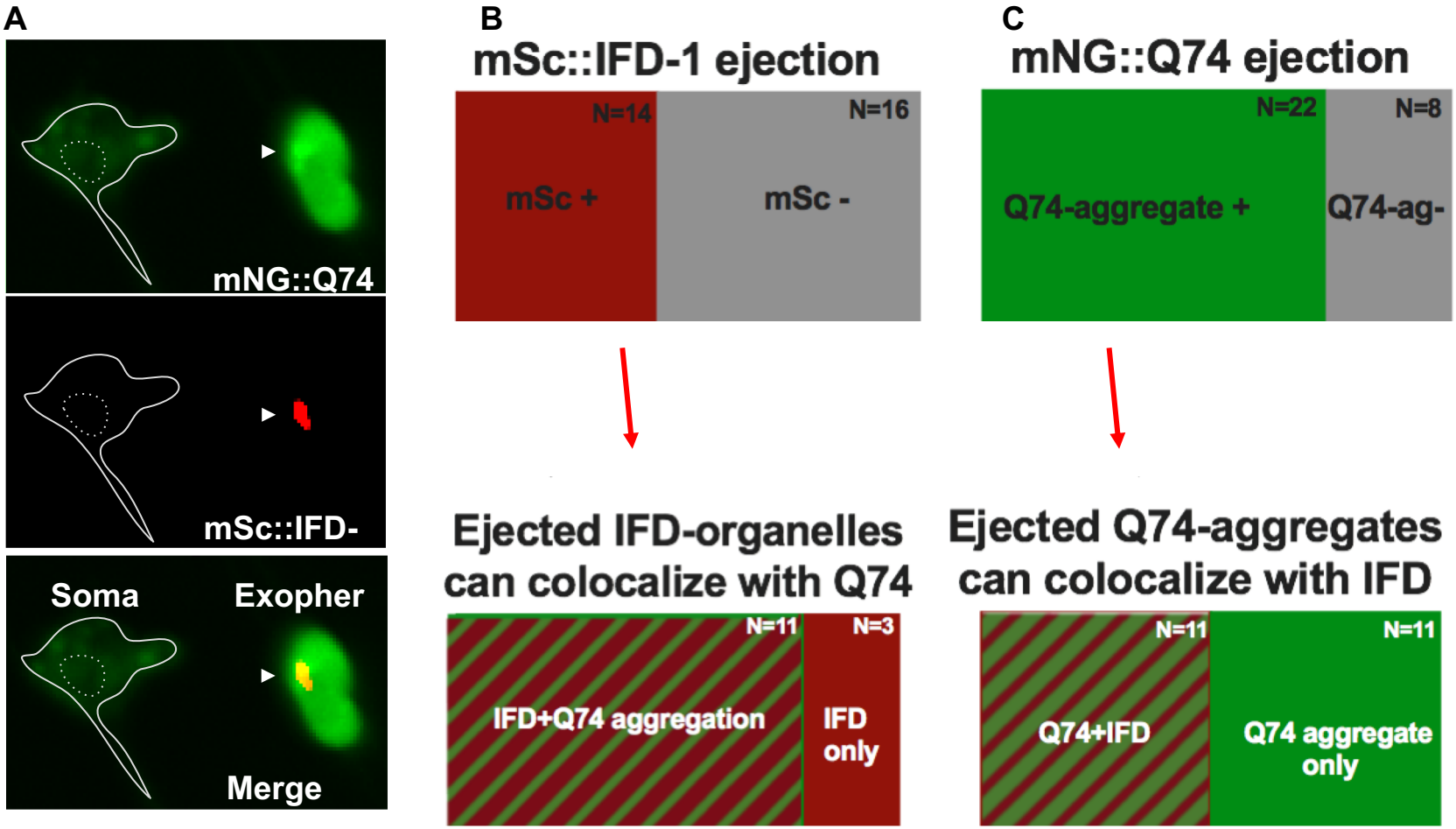

Arnold *et al.*,
Supplementary Figure 18

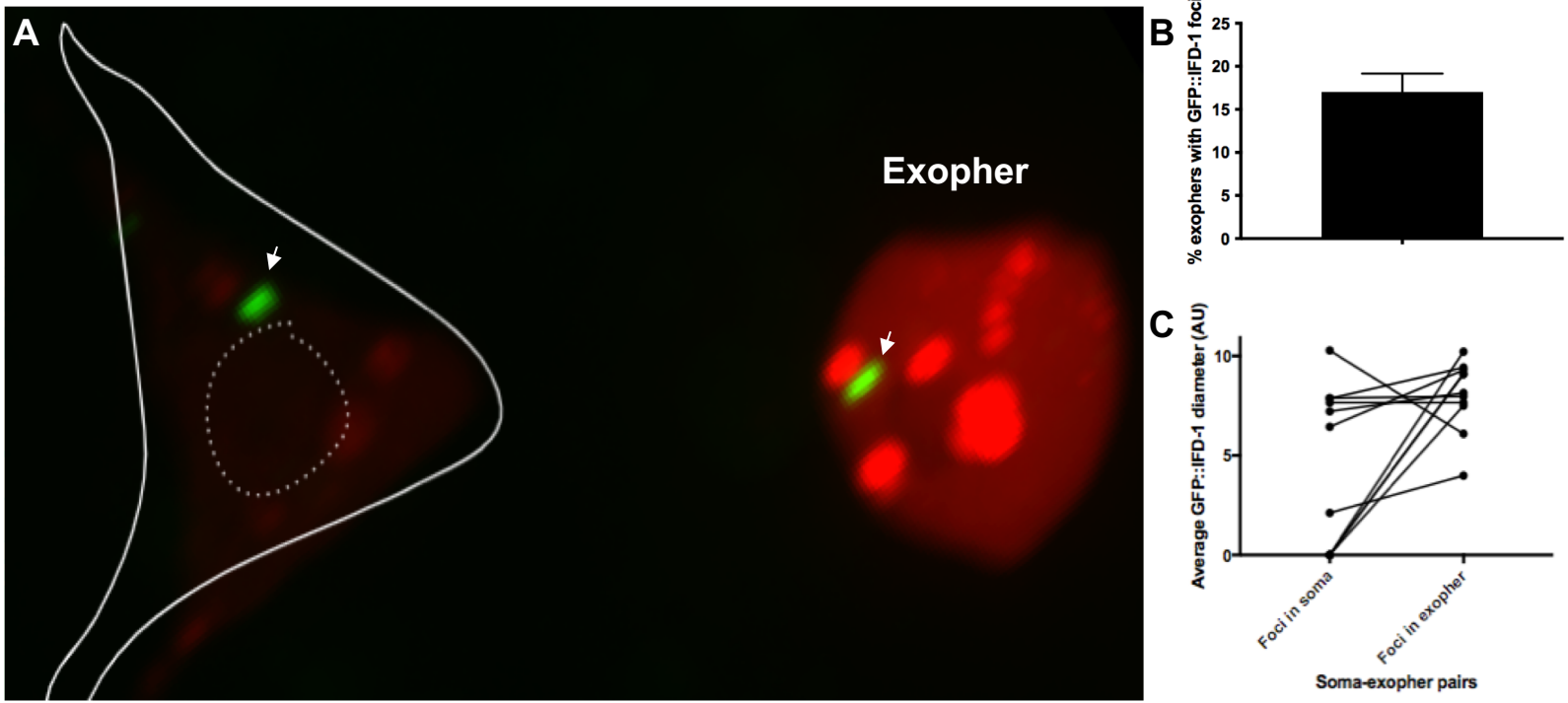

Arnold *et al.*,
Supplementary Figure 19

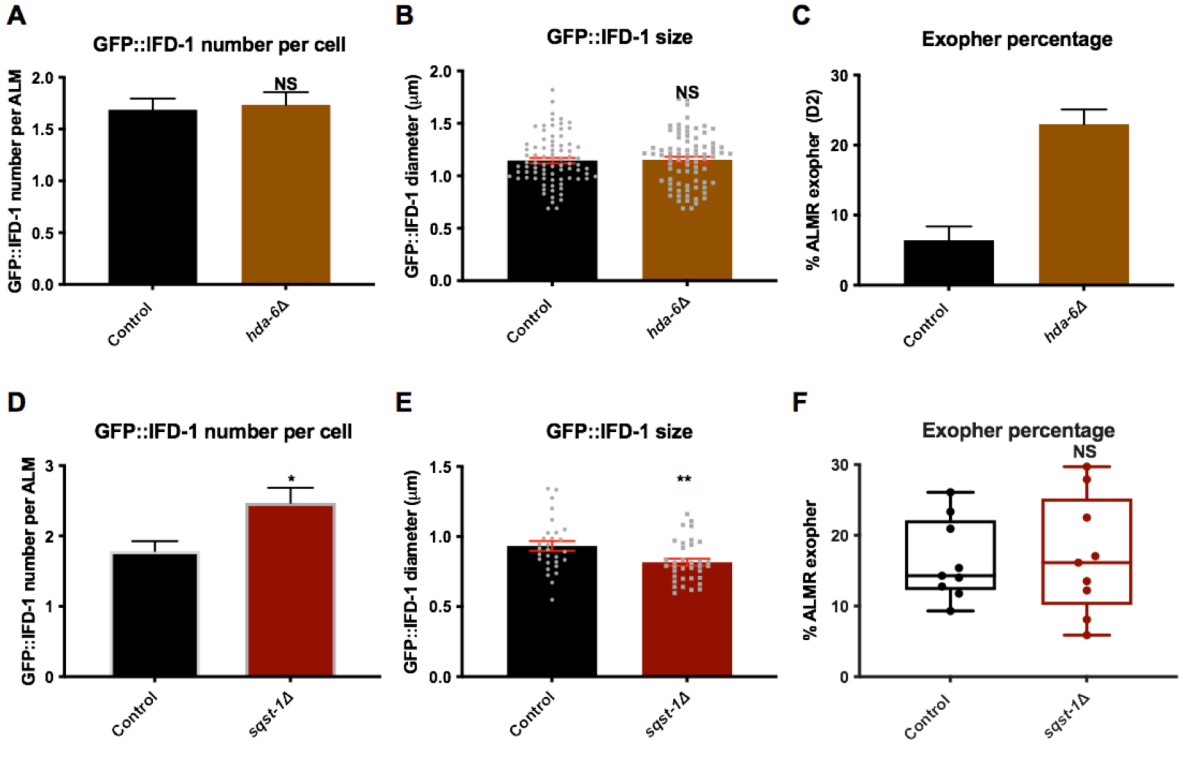

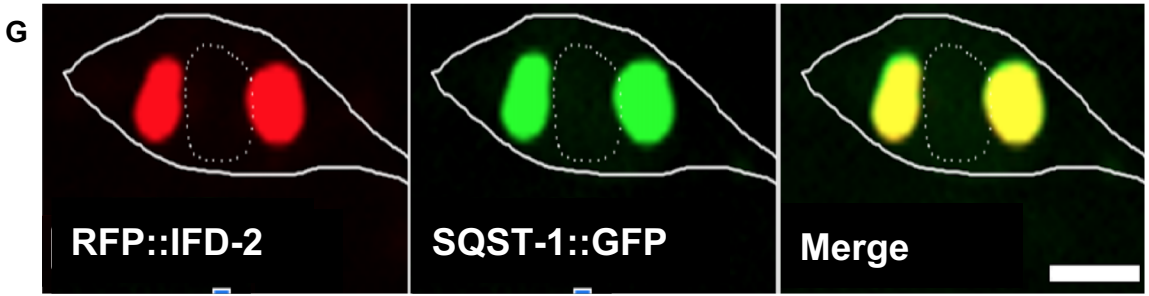

Arnold *et al.*,
Supplementary Figure 20

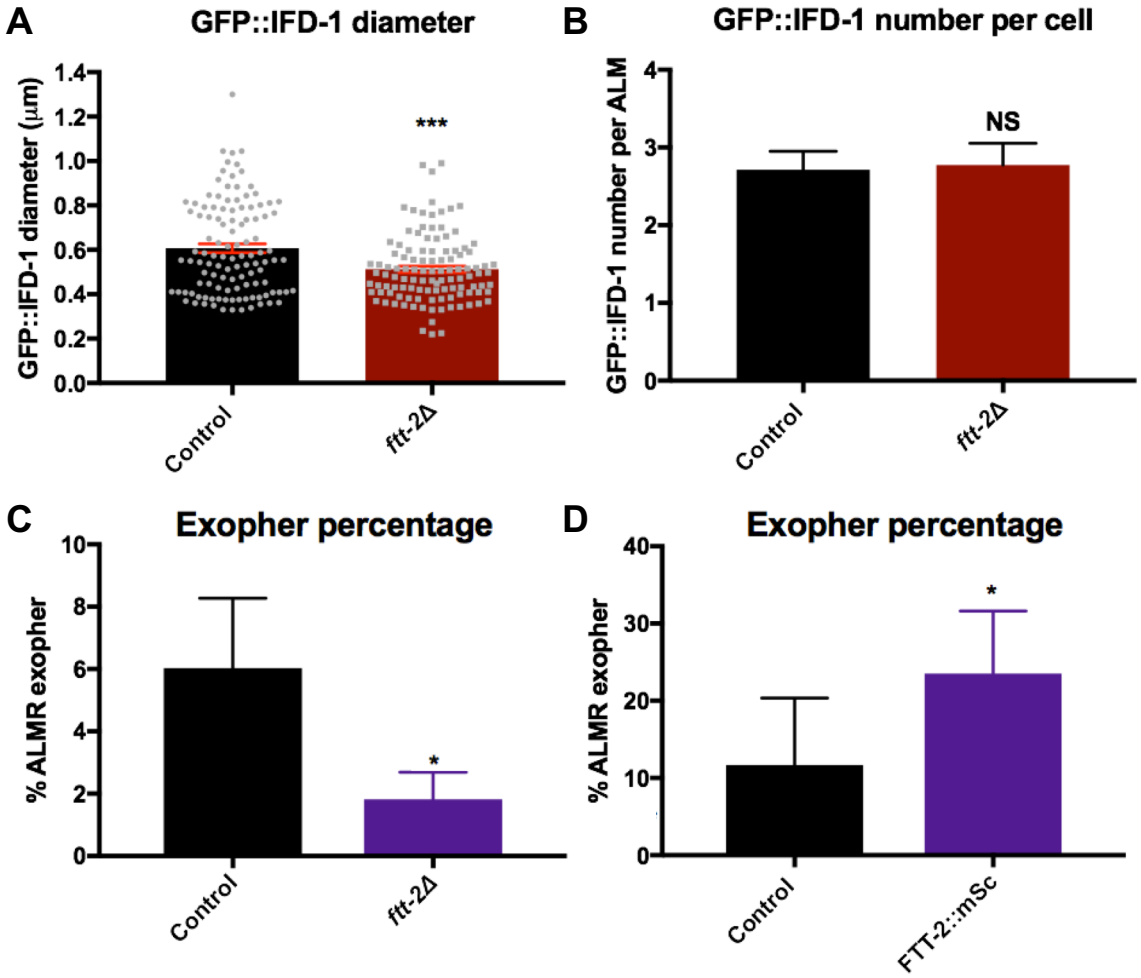

Arnold *et al.*,
Supplementary Figure 21

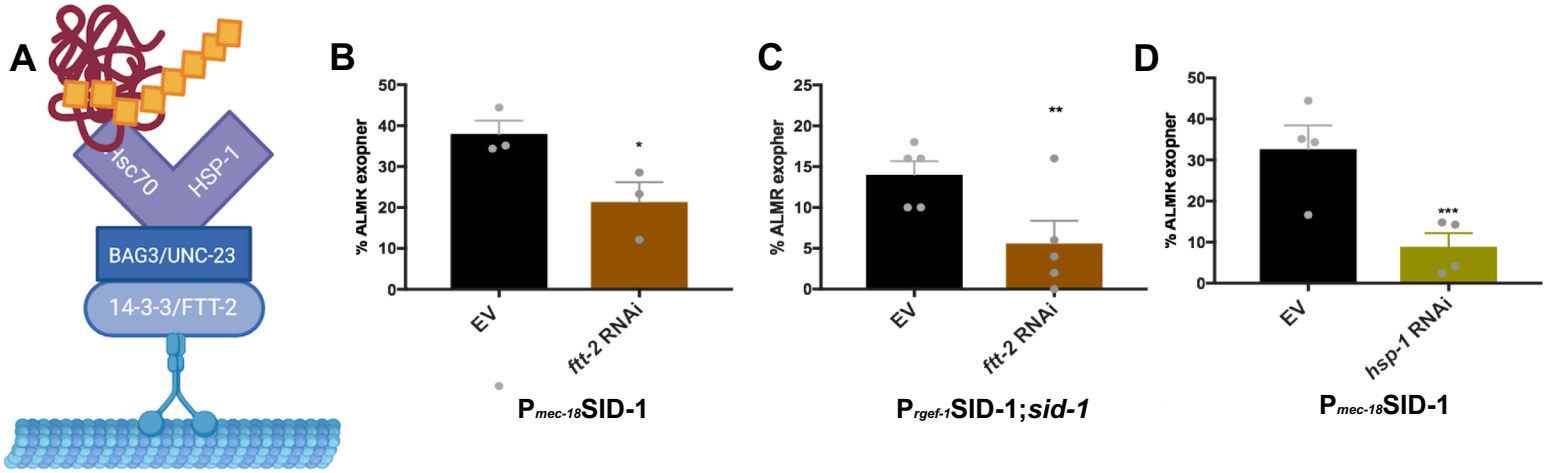

Arnold *et al.*,
Supplementary Figure 22

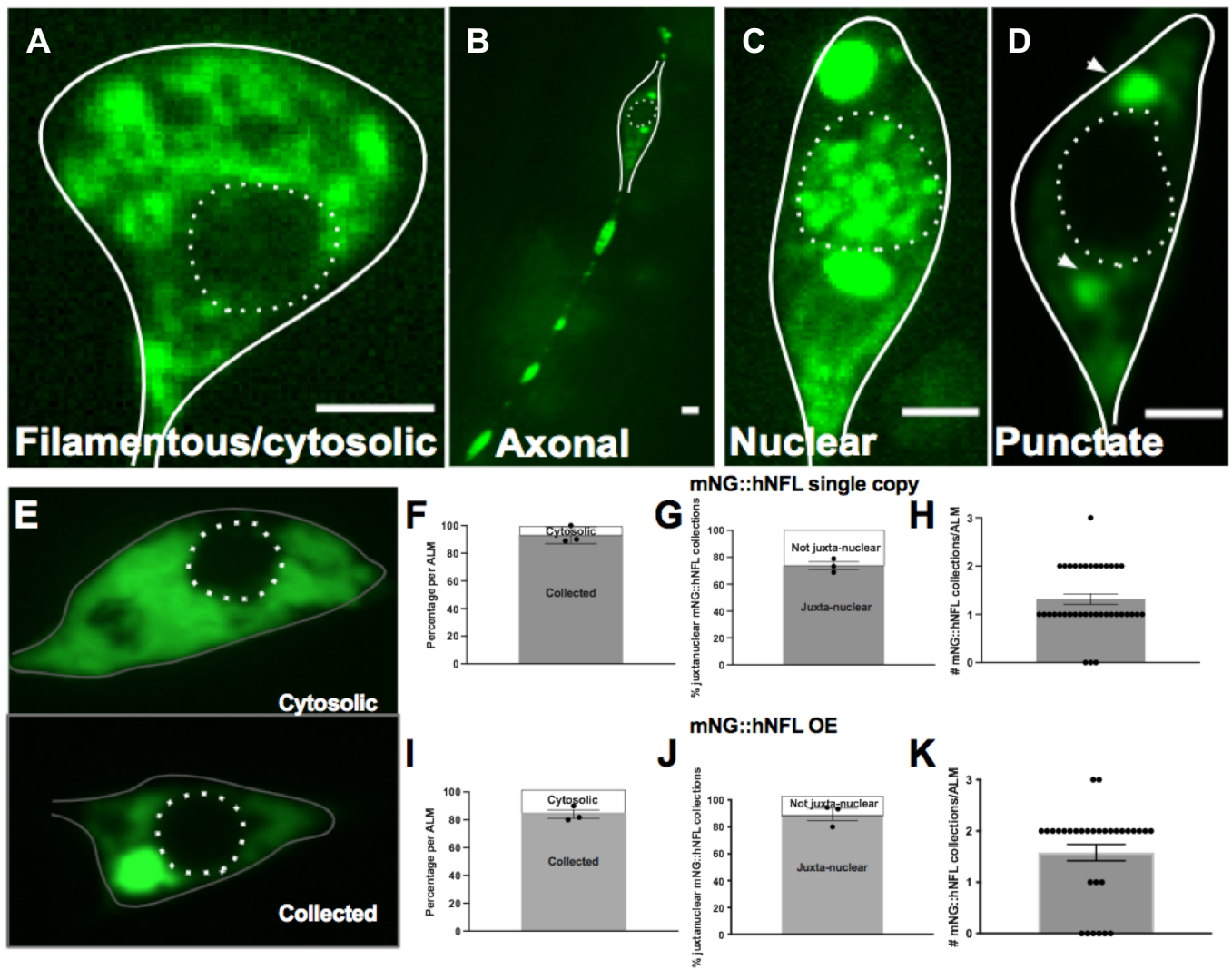

Arnold *et al.*,
Supplementary Figure 23

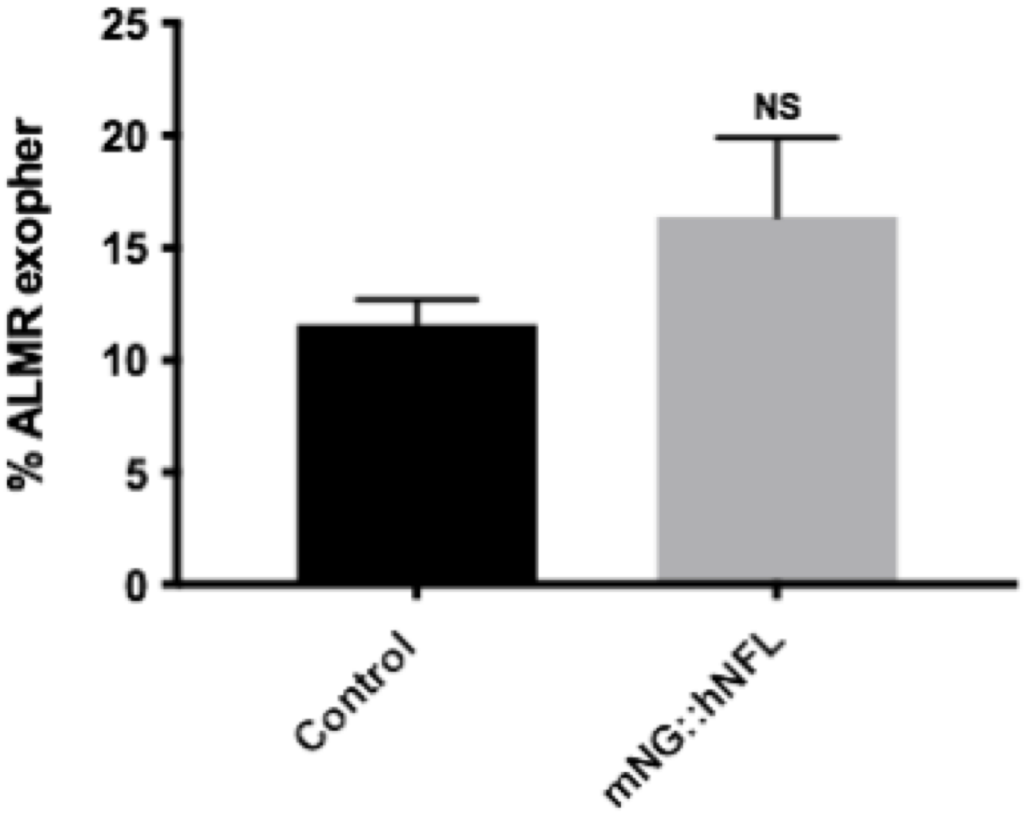

Arnold *et al.*,
Supplementary Figure 24

Video link 1: https://youtu.be/zMvtUJJbrzc
Video link 2: https://youtu.be/Gtex9gShdR8